Excited States and Band Structures of ^{129}Pr and ^{132}Sm

UNIVERSITY OF LIVERPOOL

by

Lorna Waring

Supervised by

Professor David Joss and Professor Robert Page

Thesis submitted in accordance with the requirements of the University of Liverpool
for the degree of Doctor in Philosophy

in the

Faculty of Science and Engineering
Department of Physics

April 2023

UNIVERSITY OF LIVERPOOL

Abstract

Faculty of Science and Engineering

Department of Physics

Excited States and Band Structures of ^{129}Pr and ^{132}Sm

by Lorna Waring

The newly commissioned JUROGAM3 γ-ray spectrometer was used in conjunction with MARA to investigate nuclei in the rare-earth mass region around $A \approx 130$ in order to investigate the excited states of several nuclei near the proton drip line. Nuclei in this region are known to be some of the most highly deformed, and it is of particular interest to understand how deformation changes with decreasing neutron number. Excited states have been established in the proton-rich odd-A nucleus ^{129}Pr and the even-even nucleus ^{132}Sm. The experiment was carried out at JYFL-ACCLAB using the fusion-evaporation reactions ^{58}Ni(^{78}Kr, $\alpha 3p$)^{129}Pr and ^{58}Ni(^{78}Kr, $2p2n$)^{132}Sm to produce the nuclei ^{129}Pr and ^{132}Sm respectively. Following the identification of several nuclei produced during the experiment and the utilisation of the mass separating capabilities of MARA, both level schemes for ^{129}Pr and ^{132}Sm have now been significantly extended. Two new sidebands in ^{129}Pr have been established up to a spin of $43/2^-$, as well as the extension of a known strongly coupled band up to a spin of $43/2^+$. The discovery of the S-band has also been established in ^{132}Sm up to a spin of 20^+, as well as a tentative extension to the known ground-state band. Experimentally derived quantities have been compared

to theoretical calculations, and configuration assignments have been made with the predictions of the cranked shell model.

I am among those who think that science has great beauty.

MARIE CURIE

What we do in life echoes in eternity.

MAXIMUS

Acknowledgements

I would like to express my sincere gratitude to my primary supervisor, Professor David Joss. Thank you for your invaluable guidance, support and encouragement throughout my PhD journey. Your unwavering belief in my abilities and encouragement have been instrumental in bringing this thesis to fruition. Also, a heartfelt thank you to my other supervisor, Professor Robert Page. Having your input and support during my research has been an absolute privilege.

Thanks also go to all those involved in the nuclear research cluster here at the University of Liverpool - I have been extremely fortunate to be surrounded by some of the most incredible minds in the field. Your expertise and feedback have enabled me to not only improve my academic work, but also inspired and motivated me to grow as a person. Special thanks also go to Dr Eddie Paul and Dr Andy Briscoe. A huge thank you also goes to all those involved at the research facility at the University of Jyväskylä for providing the necessary resources and facilities to complete this work. Additionally, I would like to acknowledge the financial support of the STFC that has enabled me to complete this research project.

I would also like to express my deepest appreciation for my friends who have made this journey the most memorable experience. Steve, thank you for always keeping me sane and giving me your unconditional support throughout everything, both personally and professionally. You have helped me to finally believe in myself and our friendship will always mean the world to me - I couldn't have done it without you. Special thanks also go to Conor, my third and unofficial supervisor. For not only providing me with guidance with my work, but also for being the best laugh and genuinely making this rollercoaster a fun ride. Holly, thank you for not only bringing your positive mindset and friendship, but also for your academic work that

Contents

List of Figures

List of Tables

Chapter 1

Introduction

One of the primary objectives in the field of nuclear physics is to determine the number of protons and neutrons that can be bound within the atomic nucleus, in order to establish the limits of observable nuclei and elucidate their underlying structures. These limits are defined by the 'drip lines' which represent the regions where the nucleus becomes unbound due to the nucleon emission, and the nucleon separation energy changes sign. The study of nuclear limits is important in that it allows us to understand the effective interactions in nuclei, and further test the current nuclear formulae that have been developed semiempirically. Such formulae that have been established using masses of known nuclear, appear to break down when applied to nuclei far from stability and do not take into account further nuclear effects that arise as the result of a many-body system. Due to the Coulomb repulsion between protons, it is not possible for nuclei to exist with a very large proton excess – in the lighter elements (Z < 50) the small Coulomb potential barrier enables the emission of a proton to occur quickly, thus the proton drip line lies close to N=Z, i.e. the valley of stability. For heavier elements, the relatively large Coulomb barrier slows the proton emission process sufficiently enough that it may enable the study of proton-emitting nuclei using a variety of experimental techniques.

The data analysed in this work were obtained from an experiment conducted in JYFL-ACCLAB at the University of Jyväskylä with JUROGAM3 and MARA (Mass Analysing Recoil Apparatus) and was the first experiment in a planned future programme using a range of tagging techniques with MARA to establish the excited states of proton-unbound nuclei in this mass region. The experiment was specifically

set up to investigate the excited states in ^{131}Eu [1]. Several nuclei are observed within this region using an optimised beam energy, and the identification of rotational band structures in specific nuclei will help inform deformation parameters that provide crucial constraints on sophisticated models of deformed proton emitters.

The main motivation behind this work is to further analyse the excited states of rare-earth deformed nuclei that have been produced during the aforementioned experiment, and gain an understanding of the general systematics of such nuclei as well as the methods of analysis used to investigate them. In the peak deformation region, there are numerous band structures observed, many of which are 'floating' bands in that the transitions connecting the superdeformed bands with the low-lying states are not known. An aim of this research is to investigate the relative ordering of states in the nucleus, and also to look at the correlations between bandheads. First, Chapter 2 will look at the background physics relating to the data produced. Chapter 3 will then look at the theory of γ-ray spectroscopy, including the theory of γ decay and the spectroscopy techniques relevant to the experimental setup used to obtain data. Chapter 4 will then explain the experimental setup and how the data were obtained. Chapters 5 and 6 will present a selected portion of the results obtained from the data relating to the specific praseodymium nuclei to be discussed in this work, as well as a discussion of how these results may be interpreted. Chapter 7 will then summarise the findings of the report and discuss how these results fit into the wider context of this research area, as well as discussing further prospects following on from this work.

Chapter 2

Physics Background

This chapter will review the physics concepts that are relevant to the experimental analysis presented in this work.

Nuclear physics involves the study of the structure, interactions and properties of atomic nuclei and nuclear matter. Such studies utilise measurements and calculations of static properties such as electric charge, mass, radius, binding energy, angular momentum, size, shapes and energy of excited states, as well as observing the dynamics of nuclear decays and reactions. The nucleus is a many-body system consisting of neutrons and protons that are held together by the strong nuclear force, that overcomes the Coulomb repulsion between the protons. When discussing nuclear properties, it is difficult to describe them in terms of constituent nucleons, thus it is preferential to use an approach that encompasses the overall composite structure of the nucleus.

Since there is not one single comprehensive nuclear theory, it is necessary to construct theoretical nuclear models that enable the verification of experimentally observed results. The research of nuclear structure involves the interplay of two types of nuclear motion - 'single-particle motion' and 'collective motion'. The first of these is based on the concept of non-interacting, single-nucleon states that imply a simplistic nuclear shell model with near-spherical nuclei. In this model, it is only the nucleons that are in the vicinity of the Fermi surface that are involved. The second of these nuclear motions represents a coherent motion, in which the interactions between valence and core nucleons are considered in order to describe bulk nuclear properties, and essentially the theory of nuclear deformation.

2.1 The Nuclear Shell Model and Nuclear Potentials

The nuclear shell model (Fig. 2.1) is one in which the structure of the nucleus is described in terms of energy levels, utilising the Pauli exclusion principle. Analogous to the atomic shell model (describing the arrangement of electrons in an atom), the origin of the nuclear shell model was the observation of increased stability in nuclei. This led to the discovery of 'magic numbers' of nucleons (2, 8, 20, 28, 52, 82, 126), such that they are arranged in complete shells within the nucleus. Nuclei with such an arrangement are therefore considered more stable against nuclear decay, since they have a higher binding energy per nucleon than expected based upon the predictions of the semi empirical mass formula (a theory based upon the Liquid Drop Model). The shell model is representative of a 'single-particle model' in which the motion of A independent nucleons are treated as a particle within a mean-field potential created by all other nucleons. This means that nucleons exist in discrete levels that are separated by energy gaps, allowing the many-body nuclear problem to be treated as a two-body problem that may be solved.

By giving the average potential acting on each particle as

$$V_i(r_i) = \left\langle \sum_j v(r_{ij}) \right\rangle, \tag{2.1}$$

where $v(r_{ij})$ is the short range interaction potential between two nucleons i and j.

Thus, the Hamiltonian, H may be expressed as

$$H = \sum_i T_i + \sum_{ij} v(r_{ij}), \tag{2.2}$$

which can in turn be rewritten as

$$H^{'} = \sum_i [T_i + V_i(r_i)] + \lambda \left[\sum_{ij} v(r_{ij}) - \sum_i V_i(r_i) \right], \tag{2.3}$$

where $H^{'}$ is the perturbed Hamiltonian and the second term is the perturbation term due to the residual interactions. For $\lambda = 1$, $H^{'} = H$ and it is the assumption for the shell model that the central interaction is greater than the residual interactions between nucleons, thus $\lambda \to 0$.

It follows on from this that it is necessary to choose a suitable potential that enables the solutions of the Schrödinger equation to be obtained from

$$(T + V)\Psi(r) = E\Psi(r), \tag{2.4}$$

thus yielding the energy eigenvalues of the single-particle orbits.
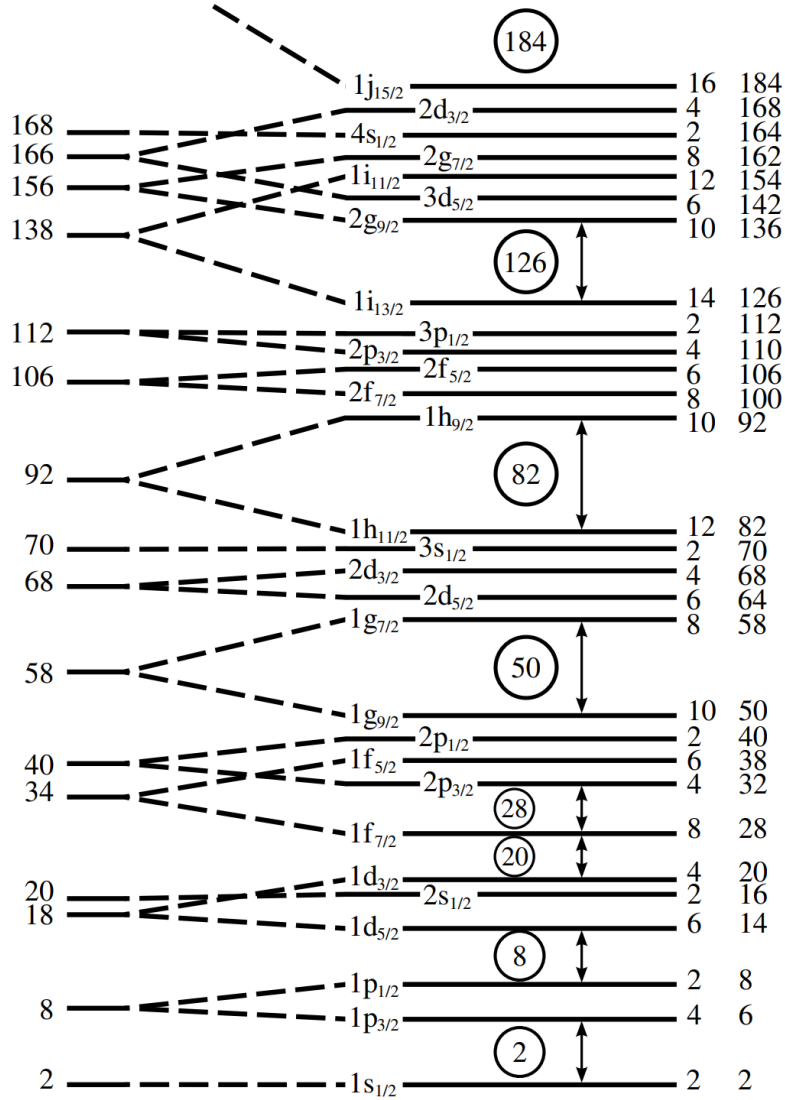
Figure 2.1: The complete nuclear shell model displaying the effects of the spin-orbit interaction, which splits the levels with $l > 0$ into two new levels (solid lines on the right hand of figure). To the right of each of these levels are shown the capacity and cumulative number of nucleons up to that level. Circled numbers indicate the magic numbers of nucleons.

2.1.1 The Harmonic Oscillator Potential

The harmonic oscillator potential may be given as

$$V_{HO}(r) = -V + \frac{1}{2}M\omega^2 r^2, \qquad (2.5)$$

where V is the depth of the potential well, M is the mass of the particle, r is the nuclear radius and ω is the frequency of the simple harmonic motion of the particle.

Whilst this potential has the advantage of being able to solve the Schrödinger equation analytically, for large r the potential tends to infinity, and so is not representative of a physical potential. The Schrödinger equation for this potential can be written as

$$H_{HO} = -\frac{\hbar^2}{2M}\nabla^2 - V + \frac{1}{2}M\omega^2 r^2, \tag{2.6}$$

with the solutions yielding the energy eigenvalues of the nth shell as

$$E_n = \left[n + \frac{3}{2}\right]\hbar\omega, \tag{2.7}$$

where n is the principal quantum number and represents the number of oscillation quanta. There is a degenerate group of levels with different value of angular momentum quantum numbers, ℓ for each value of n such that

$$d_n = (n+1)(n+2), \tag{2.8}$$

where d_n is the total number of degenerate states, and each of the shells contains states with the same parity such that

$$\pi = (-1)^\ell = (-1)^n, \tag{2.9}$$

This potential does not produce the correct magic numbers, and as such it is necessary to continue exploring various other potentials that are able to obtain a realistic nuclear model capable of describing experimentally observed results.

2.1.2 The Woods-Saxon Potential

The Woods-Saxon potential [2] may be given as

$$V_{WS}(r) = \frac{-V_0}{1 + \exp[(r - R_0/a]}, \tag{2.10}$$

where V_0 is the potential well depth (usually set to ≈ 50 MeV, r is the distance from the centre of the nucleus, a is the surface diffuseness of the nucleus, and $R_0 = r_0 A^{\frac{1}{3}}$ is the nuclear radius term (where $r_0 = 1.2$ fm and A is the mass number). Unlike the harmonic oscillator, the Wood-Saxon potential describes a finite potential such that $V(r) \to 0$ when $r > R_0$. The surface diffuseness term, a, takes into consideration the fact that the boundaries of the nucleus are not sharply defined, and is usually set to a value of ≈ 0.5 fm. A comparison of both the harmonic oscillator and Woods-Saxon Potentials is shown in Fig. 2.2. Whilst the Woods-Saxon potential is strong within the nucleus, it can be seen that following an increase in the potential with distance, the potential approaches zero, thus showing the nature of the strong nuclear forces at short distances. This potential is also a desirable choice in that it also reproduces a flat-bottomed potential well. This reflects the fact that near the centre of the nucleus, there is no net force since $\frac{\delta V}{\delta r} = 0$, and so all nucleons feel the nuclear forces uniformly.

The Hamiltonian can now be written using the potential given in Eq. 2.10 as

$$H_{WS} = \frac{-\hbar}{2M}\nabla^2 + \frac{V_0}{1 + \exp[r - R_0/a]}, \tag{2.11}$$

Whilst the parameters chosen for the Woods-Saxon potential relieves the degeneracy of the harmonic oscillator states, this potential still does not correctly reproduce the magic numbers and so a further correction to the nuclear Hamiltonian is required.
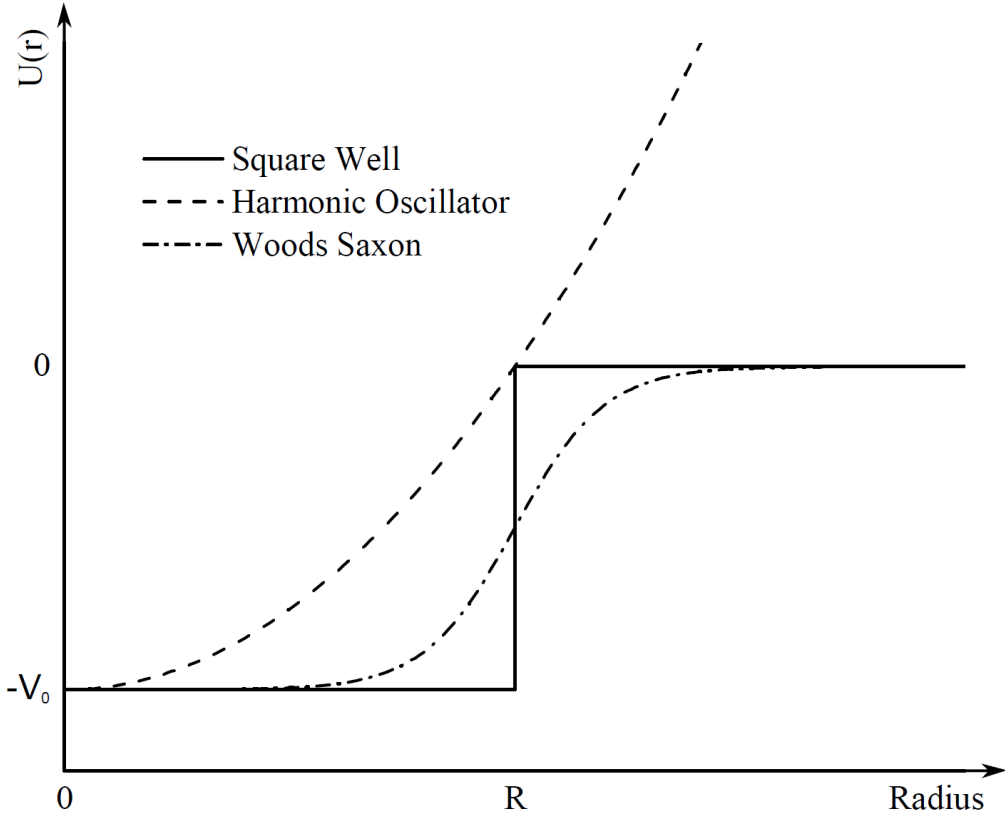
Figure 2.2: Comparison of nuclear potentials obtained from theoretical values. Showing the Woods-Saxon potential as a combination of the square well potential and harmonic oscillator potential.

2.1.3 Spin-Orbit Coupling

In order to empirically fit the magic numbers for nuclei, a spin-orbit interaction was introduced (analogous to the spin-orbit interaction in atomic physics). This interaction term may be added to the nuclear potential so that the force felt by a nucleon is now dependent on the direction of its spin, relative to its motion. The spin-orbit potential may be given by

$$V_{SO} = f(r)\boldsymbol{\ell} \cdot \boldsymbol{s}, \tag{2.12}$$

where $f(r)$ controls the strength of the coupling. The spin-orbit coupling now relieves the degeneracy of the Woods-Saxon levels with $\boldsymbol{j} = \boldsymbol{\ell} \pm \frac{1}{2}$, where $\boldsymbol{j}$ is the total angular momentum ($\boldsymbol{j} = \boldsymbol{\ell} + \boldsymbol{s}$). Contrary to the case for atomic physics, the

spin-orbit interaction must be an attractive force to account for the observation the $\boldsymbol{j} = \boldsymbol{\ell} + \frac{1}{2}$ states are lower in energy than the $\boldsymbol{j} = \boldsymbol{\ell} - \frac{1}{2}$ states. The components of the spin-orbit coupling are shown in Fig 2.3 and depicts that whilst $\boldsymbol{j}$ precesses about the symmetry axis, $\boldsymbol{\ell}$ and $\boldsymbol{s}$ precess around $\boldsymbol{j}$.
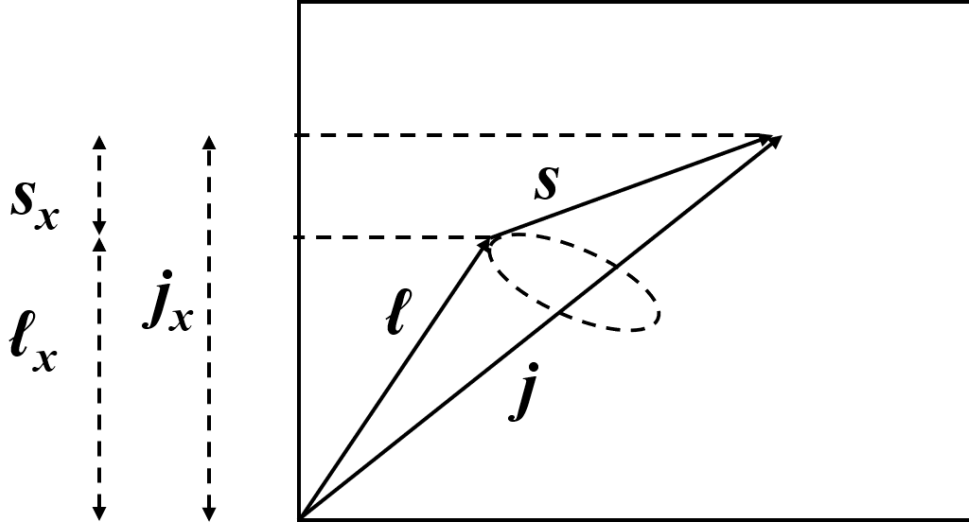
Figure 2.3: The spin-orbit coupling showing the components of the total angular momentum, $\boldsymbol{j}$. The components of these vectors on the rotational axis are also shown.

The total angular momentum $\boldsymbol{j}$, the projection of $\boldsymbol{j}$ on the rotation axis, $\boldsymbol{j_x}$, and $\boldsymbol{\ell}$ all remain constants of the motion, and so are good quantum numbers. The components of $\boldsymbol{\ell}$ and $\boldsymbol{s}$ on the rotation axis ($\boldsymbol{\ell_x}$ and $\boldsymbol{s_x}$ respectively) are not constant however.

By now adding the spin-orbit term to the Woods-Saxon potential given in Eq.2.11, the nuclear Hamiltonian may now be given by

$$H_{WS} = \frac{-\hbar}{2M}\nabla^2 + \frac{V_0}{1 + \exp\left[r - R_0/a\right]} - f(r)\boldsymbol{\ell} \cdot \boldsymbol{s}, \tag{2.13}$$

Since the spin-orbit term is proportional to $\boldsymbol{\ell}$ (i.e. the splitting is proportional to $\boldsymbol{\ell}$), for states in which the spin-orbit coupling interaction is sufficiently large, such states may be lowered in energy enough so that they reside in the next lowest major

oscillator shell. These states are known as 'intruder' or 'unnatural parity' states. Evidence of these intruder states becomes apparent in highly deformed nuclei.

2.2   Nuclear Deformation

For nuclei with closed-shell configurations, i.e. magic nuclei, the nucleus is spherical, thus the orbits of individual nucleons are equally orientated. It is expected that the shell structure is modified significantly far from stability - for shells that are partly filled, the orbits of the nucleons are strongly anisotropic and the nucleus deviates away from sphericity. These shape changes arise from changes in the ratio of nucleons within the nucleus and the resulting shapes are created by both the residual pairing interactions between nucleons, and the effect that individual nucleons have on driving deformation. As will be discussed in further detail, the nucleus will favour an ellipsoidal shape should nucleons behave in a collective manner, as well as a number of anisotropic orbitals also being coherent.

To give a more complete description of nuclear deformation, the nucleus can be described using spherical harmonics as a 'drop' of matter with an equipotential surface, $R(\theta, \phi)$ given by

$$R(\theta, \phi) = R_0 \left[1 + \sum_{\lambda=0}^{\infty} \sum_{\mu=-\lambda}^{\lambda} \alpha_{\lambda\mu} Y_\lambda^\mu(\theta, \phi) \right], \tag{2.14}$$

where R_0 is the radius of the sphere, $Y_\lambda^\mu(\theta, \phi)$ are the spherical harmonics, and the coefficients $\alpha_{\lambda\mu}$ (with $\lambda\mu$ being the Hill-Wheeler coordinates [3]) represent the distortion of the shape from sphericity (with λ describing the type of deformation shown in Fig. 2.4).

$$\lambda = 0 \qquad \lambda = 1 \qquad \lambda = 2 \qquad \lambda = 3$$
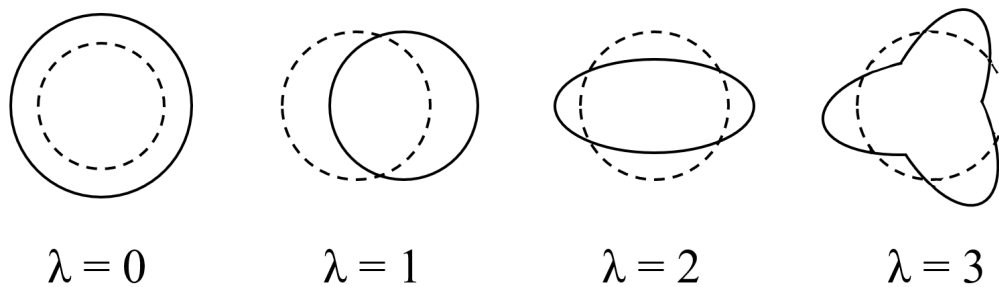
Figure 2.4: The various nuclear deformations showing the differing constant value of λ. Dashed lines depict the equilibrium shape, solid lines depict the vibrating surface of the nucleus.

It can be seen that when $\lambda = 1$, this term simply describes the displacement of the centre of mass and so this does not give rise to nuclear excitation. In the case of this work, the $\lambda = 2$ term is of greatest importance since it describes quadrupole deformation, representing a prolate, axially symmetric nucleus. For the quadrupole deformation, Eq. 2.14 reduces to

$$R(\theta, \phi) = R_0 \left[1 + \sum_{\mu=-2}^{2} \alpha_{2\mu} Y_2^{\mu}(\theta, \phi) \right], \qquad (2.15)$$

where for axially symmetric shapes, the $\alpha_{\lambda\mu}$ coefficients are therefore defined in the system of principal axes and constrained such that $\alpha_{22} = \alpha_{2-2}$ and $\alpha_{21} = \alpha_{2-1} = 0$.

Together with the three Euler angles (that define the transformation from laboratory to intrinsic frames), the two independent coefficients α_{20} and α_{22} now completely define the system, i.e. the shape of the nucleus.

In the intrinsic frame (the system of principal axes), it is possible to introduce polar coordinates (β_2, γ) as an alternative parameterisation, defining the relations as

$$\alpha_{20} = \beta_2 \cos\gamma; \qquad \alpha_{22} = \frac{-1}{\sqrt{2}} \beta_2 \sin\gamma, \qquad (2.16)$$

where the parameter, β_2, is a measure of the total deformation (the root-mean-sqare

(RMS) deviation of the surface of the nucleus from a sphere of radius, R_0), given by

$$\beta_2^2 = \sum_{\mu} |\alpha_{2\mu}|^2, \tag{2.17}$$

and the parameter, γ, is known as the *triaxiality* parameter that describes the lengths along the principal axes, i.e. how the deformation is distributed over the nuclear surface.

In terms of the alternative parameters, the nuclear surface may now be described by

$$R(\theta, \phi) = R_0 \left[1 + \sqrt{\frac{5}{16\pi}} \, \beta_2 \left\{ \cos \gamma (3 \cos^2 \theta - 1) + \sqrt{3} \, \sin \gamma \, \sin^2 \theta \, \cos 2\phi \right\} \right], \tag{2.18}$$

Both the β_2 and γ parameters are defined using the Lund convention [4] shown in Fig. 2.5. The shapes at $0°$ and $-60°$ represent collective-motion with prolate and oblate shapes respectively. The shapes at $+60°$ and $-120°$ represent single-particle motion with oblate and prolate shapes respectively. When $\beta_2 > 0$, this elongates the symmetry axis, giving the form of a *prolate* ellipsoid. When $\beta_2 < 0$, this contracts the symmetry axis, giving the form of an *oblate* ellipsoid. When $\beta_2 = 0$, a perfect sphere is described. To provide a sufficient description of the triaxiality of deformed quadrupole shapes, the range of γ values from $-60° \leq \gamma \leq 0°$ is the region spanning the collective regime, where rotation for triaxial shapes is around the intermediate axis. However, three times this range is needed in order to correspond to the three principal axes about which the system may be rotated or *'cranked'*.
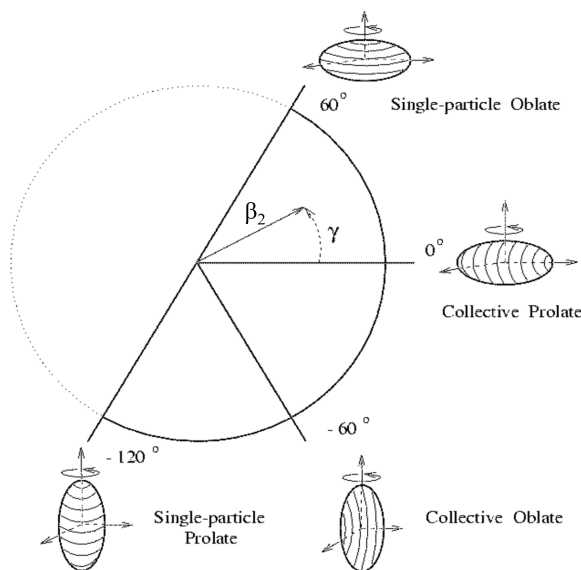
Figure 2.5: The Lund convention for describing quadrupole shapes [5].

2.3   The Deformed Shell Model

Having discussed the shell model, it can be understood that for closed-shell nuclei, it can be seen that a spherical nucleus is the result of the pairing force dominating above the deforming power of individual nucleons. Above closed shell systems, independent particle models fail to adhere to empirical observations of nuclei that have many nucleons added above such configurations. When additional nucleons are added, the equilibrium shape of the nucleus is gradually driven away from sphericity and instead becomes softer against deformation and develops an ellipsoid shape.

Collective rotational modes occur in non-spherical (deformed) nuclei, involving a large number of nucleons in the nuclei moving coherently – characterised by the small changes in angular momentum contributions. Should the nucleus be axially symmetric, rotational effects may only be observed about an axis that is perpendicular to the symmetry axis. In order to further extend the shell model, it is also necessary to deform the potentials described previously, thus enabling a more accurate description of deformed nuclei.

2.3.1 The Anisotropic Harmonic Oscillator Potential

In the intrinsic frame, deformation is usually introduced along the z-axis (i.e. $x = y \neq z$). For a deformed nucleus, the Anisotropic Harmonic Oscillator (AHO) may be given as

$$V_{AHO} = \frac{1}{2}M\left[\omega_\perp^2\left(x^2 + y^2 + \omega_z^2 z^2\right)\right], \qquad (2.19)$$

where $\omega_\perp$ and ω_z represent the frequencies of the simple harmonic motion perpendicular and parallel to the nuclear symmetry axis respectively. In terms of the nuclear deformation parameter, δ, these frequencies may be given by

$$\omega_z \approx \left[1 - \frac{2}{3}\delta\right]; \qquad \omega_\perp \approx \left[1 + \frac{1}{3}\delta\right], \qquad (2.20)$$

with $\omega_0^3 = \omega_\perp^2 \omega_z$ for volume conservation. The deformation parameter δ is defined as $\delta = \Delta R/R_0$, with ΔR being the difference between the radii parallel and perpendicular to the symmetry axis, and R_0 is the mean radius. It is also possible to express δ in terms of β_2 as

$$\beta_2 = \frac{4}{3}\sqrt{\frac{\pi}{5}}\delta. \qquad (2.21)$$

The value of the harmonic oscillator quantum, ω_0 is deduced from

$$\hbar\omega_0 = 41A^{-\frac{1}{3}}\left[1 \pm \frac{(N-Z)}{3A}\right](\text{MeV}), \qquad (2.22)$$

where plus is used for neutrons and minus is used for protons, N is the mass number and Z is the proton number.

The anisotropic harmonic oscillator potential may now be written as

$$V_{AHO} = \frac{1}{2}\hbar\omega_0(\varepsilon_2)\rho^2\left[1 - \frac{2}{3}\varepsilon_2 P_2(\cos\theta_t)\right], \qquad (2.23)$$

where ε_2 is another quadrupole deformation that is approximately $0.95\beta_2$, ρ^2 refers to the sum of 'stretched' coordinates ($\rho^2 = \xi^2 + \eta^2 + \zeta^2$), $P_2(\cos\theta_t)$ are Legendre polynomials (where the term $cos(\theta_t)$ is equal to ζ/ρ and refers to the angle between the stretched coordinates). Stretched coordinates in nuclear physics refer to a coordinate system where the radial distance of nucleons from the centre of the nucleus is defined, allowing for the separation of collective and intrinsic nuclear motion.

The solutions of the anisotropic harmonic oscillator problem are given by

$$E_{n_z n_\perp} = \left[n_z + \frac{1}{2}\right]\hbar\omega_z + \left[n_\perp + 1\right]\hbar\omega_\perp, \tag{2.24}$$

or in terms of the nuclear deformation δ,

$$E_{n_z n_\perp} \approx \left[n + \frac{3}{2}\right]\hbar\omega_0 - \frac{1}{3}\delta\left[2n_z - n_\perp\right]\hbar\omega_0, \tag{2.25}$$

with $n = n_z + n_\perp$. Eq. 2.29 is simply inclusive of the first term describing the energies of a spherical harmonic oscillator, and the second term being a correction term that is proportional to the quadrupole deformation.

2.3.2 The Modified Harmonic Oscillator or Nilsson Potential

The Nilsson potential (or modified harmonic oscillator) includes additional terms to the anisotropic harmonic oscillator potential, and may be given as

$$V_{MHO} = V_{AHO} - \kappa\hbar\omega_0\left[2\boldsymbol{\ell}\cdot\boldsymbol{s} + \mu(\boldsymbol{\ell}^2 - \langle\boldsymbol{\ell^2}\rangle_n)\right], \tag{2.26}$$

where $\boldsymbol{\ell}\cdot\boldsymbol{s}$ is the nuclear spin-orbit term in the stretched (non-Cartesian) coordinate system, whilst the last term, $\mu(\boldsymbol{\ell}^2 - \langle\boldsymbol{\ell^2}\rangle_n)$ is added to flatten the potential well in order to describe the nuclear shape with more accuracy. The coefficients, κ and μ are the spin-orbit coupling parameters (defining the strength of the coupling as

well the squareness of the potential respectively), that are obtained by fitting to the experimental energy levels and are different for each major shell.

The major shell, n (oscillator quantum number), is given by $n = n_x + n_y + n_z$ where n_x, n_y and n_z describe the x, y and z (symmetry axis) components respectively. In addition to this, other quantum numbers are used: $\ell_z = \Lambda$ (projection of the orbital angular momentum, $\boldsymbol{\ell}$ on the z-axis), $s_z = \Sigma = \pm\frac{1}{2}$ (projection of the spin, $\boldsymbol{s}$ on the z-axis), and $j_z = \Omega = \Lambda + \Sigma$ (projection of the total angular momentum $\boldsymbol{j}$ on the z-axis)(Fig. 2.6). Using this notation, it is now possible to label the energy levels in the Nilsson Schemes (an example Nilsson Diagram for protons is shown in Fig. 2.7) as

$$[nn_z\Lambda]\Omega^\pi, \tag{2.27}$$

where n is the total number of oscillation quanta, n_z is the number of oscillator shell quanta (nodes) along the direction of the symmetry axis, and the parity of the state, π is $(-1)^n$. It should be noted that parity π is often omitted from Nilsson labelling. The quantities of the total angular momentum $\boldsymbol{j}$ and $\boldsymbol{\ell}$ are no longer good quantum numbers, however their projections onto the symmetry axis (Ω and Λ respectively) are conserved.
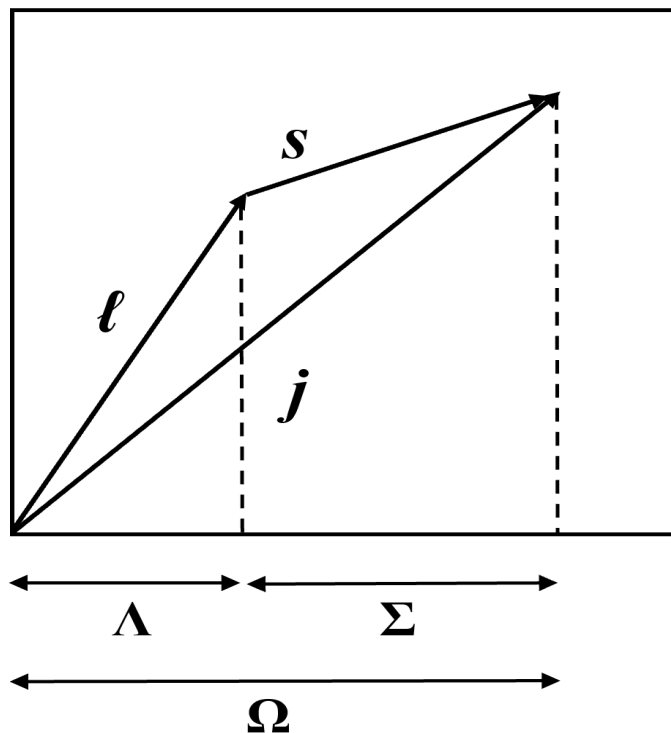
Figure 2.6: Projections of $\boldsymbol{\ell}$, $\boldsymbol{s}$ and $\boldsymbol{j}$ on the symmetry axis. Also shown are the components of these projections contributing to the Nilsson Diagram level labels. Quantum numbers shown are Σ (projection of spin, s on the z-axis), Λ (projection of orbital angular momentum, ℓ on the z-axis, and Ω (projection of the total angular momentum, j on the z-axis.

Figure 2.7: A Nilsson Diagram for protons in the region $50 \leq Z \leq 82$. The slope of the levels is related to the single-particle matrix element of the quadrupole operator. Down-sloping orbitals have positive prolate single-particle quadrupole moments, and up-sloping orbitals have negative oblate single-particle quadrupole moments. Orbital slopes are when moving from left to right. [6]

2.3.3 The Deformed Woods-Saxon Potential

As previously described in Eq. 2.26, the Nilsson Potential, V_{MHO} contains a term inclusive of $\boldsymbol{\ell^2}$ in order to flatten the potential to represent an actual nuclear shape. It was found experimentally that for heavy nuclei in the rare-earth region [7] that there was a strong shift in single-particle energies. To eliminate this overestimation presented in the Nilsson model, it is desirable to use a deformed Woods-Saxon potential which may be given as

$$V_{DWS}(r,) = \frac{-V_0}{1 + \exp\ \left[dist_\Sigma(r, \beta)/a\right]},$$

(2.28)

where $dist_\Sigma(r, \beta)$ is the distance between, r and the nuclear surface, Σ, and β represents the shape parameters that specify Σ.

The nuclear Hamiltonian for the deformed Woods-Saxon potential may now be expressed by

$$H_{DWS} = \frac{-\hbar}{2M}\nabla^2 + \left[\frac{V_0}{1 + \exp\left[dist_\Sigma(r, \beta)/a\right]}\right],$$

(2.29)

Regardless of the chosen potential used to describe the deformation, plots of the single-particle energies as a function of some quadrupole deformation parameter, are generally named Nilsson Diagrams.

2.4 Nuclear Rotation

2.4.1 Non-Collective Single-Particle Excitation

In the region of a closed shell, it is observed that pairing processes dominate and spherical nuclei result. A large total angular momentum, J, may be described as the sum of all the single-particle contributions of the valence nucleon orbitals lying close to the Fermi surface. This is generated if all the valence nucleons are aligned with the rotation axis (Fig. 2.8). The generation of this type of angular momentum

can be observed in both spherical and deformed nuclei. As with axially symmetric nuclei, collective rotation is quantum mechanically forbidden since the orientations of the intrinsic frame are indistinguishable, thus the Hamiltonian will be invariant during the rotation. Therefore, collective rotation requires a non-spherical nuclear potential.
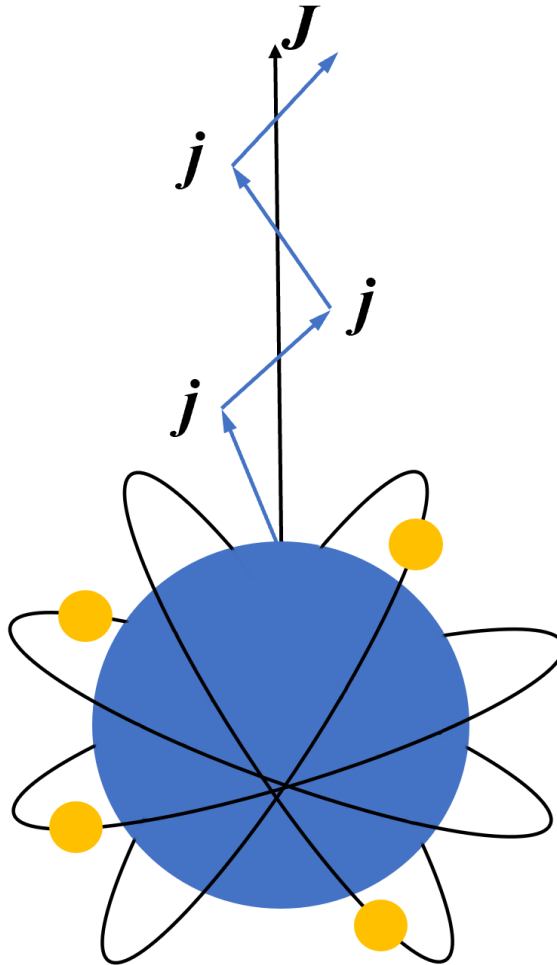
Figure 2.8: Illustration of non-collective single-particle excitation, where the total angular momentum, J, is generated from the sum of the alignment of valence nucleons, with angular momentum components, j.

2.4.2 Collective Nuclear Rotation

Classically, the kinetic energy of a rotating object is given by

$$E_{rot} = \frac{1}{2}\mathcal{J}\omega^2, \qquad (2.30)$$

where $\mathcal{J}$ is the moment of inertia (given by $\mathcal{J} = mr^2$), and ω is the rotational frequency. In terms in of the angular momentum $\ell = \mathcal{J}\omega$, the expression for energy is $\frac{\ell^2}{2\mathcal{J}}$. By then taking the quantum mechanical value of ℓ^2 and allowing I to represent the angular momentum quantum number, this then gives rise to a smooth relation between the energy and angular momentum given by

$$E = \frac{\hbar^2}{2\mathcal{J}}I(I+1), \qquad (2.31)$$

The addition of rotational energy to the nucleus is what corresponds to an increase in the angular momentum quantum number I, resulting in the formation of a rotational band as a sequence of excited states. Following on from Eq. 2.31 describing the transitions between levels, it can be seen for the energy levels of a rotor that the ratios are:

$$\frac{E(4^+)}{E(2^+)} = 3.33, \qquad (2.32)$$

and

$$\frac{E(6^+)}{E(2^+)} = 7. \qquad (2.33)$$

The rotational frequency about the x-axis may be defined as

$$\hbar\omega = \frac{dE}{dI_x} \approx \frac{1}{2}[E_{I+1} - E_{I-1}], \qquad (2.34)$$

where I_x is the projection of I onto the rotation axis:

$$I_x = \sqrt{I(I+1) - K^2}. \qquad (2.35)$$

In Eq. 2.35, I refers to the average spin of a transition given by $I = (I_i + I_f)/2$. Another formalism that is used in work carried out by Purry et al. [8], used the average aligned angular momentum given by $I_x = (I_{x_i} + I_{x_f})/2$. Whilst both of these quantities provide useful insight into nuclear structure, the formalism given in Eq. 2.34 will be used in this work, since the average spin captures the collective rotational behaviour of the system. For axially symmetric shapes, rotation about the symmetry axis, z, as depicted in Fig. 2.9, is forbidden by quantum mechanics. It is the projections $I_z = J_z = K\hbar$ that are conserved quantities for the rotational motion of the nucleus about an axis, x, perpendicular to the symmetry axis. The intrinsic wavefunction can be characterised by the spin projection, K, on the symmetry axis z. Three variables: I^2, $I_{Z_{lab}} = m\hbar$, and K, are three components that completely define the rotational state of motion of the nucleus. The eigenfunctions of I^2, m and K are given by

$$\phi_{rot} = |ImK\rangle = \sqrt{\frac{2I+1}{8\pi^2}}\mathcal{D}^I_{mK}(\Theta, \Phi, \Psi), \qquad (2.36)$$

where the functions $\mathcal{D}^I_{mK}$ are the rotation matrices, containing the wavefunctions that describe the orientation of the rotating nuclear system with the angular momentum quantum numbers I, m and K. Varying the value of K has an impact on the $\mathcal{D}^I_{mK}$ functions, hence also the form of the nuclear wavefunction. For $K=0$, the $\mathcal{D}^I_{mK}$ functions are reduced to spherical harmonics Y_{Im} and the nuclear wavefunction is given by

$$\Psi_{r,ImK=0} = \frac{1}{\sqrt{2}}\phi_{r,K=0}Y_{Im}, \qquad (2.37)$$

where r is the quantum number that represents the reflection invariance of the system, and its allowed values are given by

$$r = (-1)^I. \qquad (2.38)$$

This leads on to the following selection rules being defined as

$$I = 0, 2, 4, ... \quad \text{for} \quad K = 0 \quad \text{and} \quad r = +1$$

$$I = 1, 3, 5, ... \quad \text{for} \quad K = 0 \quad \text{and} \quad r = -1.$$

It is these two sequences of spin values that form the rotational bands observed, where the angular momentum separation between adjacent states in each band is $2\hbar$.

In order to satisfy reflection symmetry, for the cases when $K \neq 0$, the wavefunction takes the antisymmetrised form

$$\Psi^I_{mK} = \sqrt{\frac{2I+1}{16\pi^2}} [\phi_K \mathcal{D}^I_{mK} + (-1)^{I+K} \phi_{\overline{K}} \mathcal{D}^I_{m-K}], \tag{2.39}$$

where $\phi_{\overline{K}}$ is the wavefunction corresponding to the projection of the angular momentum $-K$, and is obtained from ϕ_K by a rotation of π around the rotation axis, x. As a consequence of the rotational invariance of the system, the intrinsic spin states ϕ_K (with eigenvalue K) and $\phi_{\overline{K}}$ (with eigenvalue $-K$) are degenerate and only form a single sequence of rotational states with spins given by

$$I = K, K+1, K+2, ...$$

The phase factor term in Eq. 2.39, $r = (-1)^{I+K}$ corresponding to the signature, changes sign for alternate spin values within a band. Therefore, a rotational band can be considered to be composed of two separate spin sequences with opposite signature

$$I = K, K+2, K+4, ...$$

$$I = K+1, K+3, K+5, ...$$
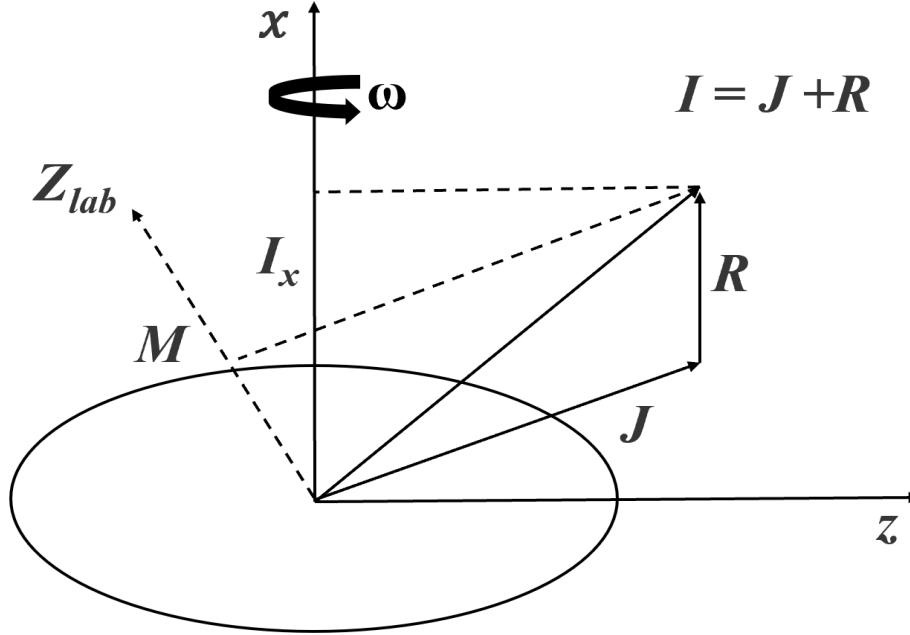
Figure 2.9: Projections of quantities describing the collective rotational motion of the nuclear system.

Moments of Inertia

Previously, Eq. 2.30 defined the kinetic energy of a rotating object, which in turn defines the static moment of inertia, $\mathcal{J}$ (sometimes denoted $\mathcal{J}^0$). It should be noted that when describing the nucleus as a rotating body, the moment of inertia in fact varies as a function of rotational frequency, and is not a static function. The actual nuclear moment of inertia ($\mathcal{J}_{Nucl}$) is seen to lie between the rigid-body moment of inertia ($\mathcal{J}_{rig}$) and the hydrodynamic moment of inertia ($\mathcal{J}_{hydro}$). The value $\mathcal{J}_{Nucl}$ lies below 50% of $\mathcal{J}_{rig}$ but five times greater than $\mathcal{J}_{hydro}$. Based upon this information, it can be deduced that there are residual interaction between nucleons, and as such, $\mathcal{J}_{Nucl}$ provides evidence of pairing. It is under rotation that the nucleus can be considered to be a body consisting of a rigid core with fluid valence nucleons. To provide more information on the collective rotational effects on the nucleus, two other moments of inertia can be introduced: $\mathcal{J}^{(1)}$ (kinematic moment of inertia) and $\mathcal{J}^{(2)}$ (dynamic moment of inertia), derived from the first and second derivatives of the following definition of the energy of rotational motion

$$E_{rot} = \frac{\hbar^2}{2\mathcal{J}}(\boldsymbol{I} - \boldsymbol{J})^2 = \frac{\hbar^2}{2\mathcal{J}}(\boldsymbol{I.I} + \boldsymbol{J.J} - 2\boldsymbol{I.J}), \qquad (2.40)$$

where the term $\boldsymbol{I.J}$ couples the degrees of freedom of the valence nucleons to the rotational motion. Thus, by assuming maximum alignment on the x axis, i.e. $I_x \approx I$ (defined in Eq. 2.35), the kinematic moment of inertia, $\mathcal{J}^{(1)}$ [9], may be defined as

$$\mathcal{J}^{(1)} = \hbar^2 I_x \left[\frac{dE}{dI_x}\right]^{-1} = \hbar\frac{I_x}{\omega}, \qquad (2.41)$$

and the dynamic moment of inertia, $\mathcal{J}^{(2)}$ [9], may be defined as

$$\mathcal{J}^{(2)} = \hbar^2 \left[\frac{d^2 E}{dI_x^2}\right]^{-1} = \hbar\frac{dI_x}{d\omega}. \qquad (2.42)$$

Both these moments of inertia can then be related by

$$\mathcal{J}^{(2)} = \mathcal{J}^{(1)} + \omega\frac{d\mathcal{J}^{(1)}}{d\omega}, \qquad (2.43)$$

and are equal only for rigid-body rotation with a frequency independent $\mathcal{J}^{(1)}$ moment of inertia, i.e. $\mathcal{J}^{(1)} \approx \mathcal{J}^{(2)} \approx \mathcal{J}_{rig}$. Whilst this is not true for nuclear rotation, at higher rotational frequencies it can be seen that $\mathcal{J}^{(1)} \approx \mathcal{J}^{(2)}$, which is taken to be due to the collapse of pairing correlations.

The moments of inertia described in Eq. 2.41 and Eq. 2.42 may also be defined by

$$\mathcal{J}^{(1)} = \hbar^2\frac{2I - 1}{E_\gamma}, \qquad (2.44)$$

and

$$\mathcal{J}^{(2)} = \frac{4\hbar^2}{\Delta E_\gamma}, \qquad (2.45)$$

for experimental measurements, where ΔE_γ is the energy separation between two peaks in the rotational band of stretched E2 γ-rays. From Eq. 2.49, it can be seen that the moment of inertia, $\mathcal{J}^{(2)}$ is not dependent on the level spin in the band, however is very sensitive to single-particle alignments. Thus, the value of $\mathcal{J}^{(2)}$ is of great interest when looking at structural changes within the nucleus.

Angular Momentum and Particle-Rotor Coupling

Following on from Eq. 2.40 where the coupling term $\boldsymbol{I.J}$ was introduced (analogous to the classical Coriolis force), the coupling of valence nucleons to a deformed core is dependent on the addition of the components of the angular momentum. This angular momentum coupling is described by the particle-rotor model. The angular momentum of the nuclear system is composed of two contributions – the collective rotational angular momentum, $\boldsymbol{R}$ (from the rotation of the deformed core), and the single-particle component, $\boldsymbol{J}$ (from the intrinsic motion of the valence nucleons). Combined, these two contributions give the total resultant angular momentum of the nucleus (illustrated in Fig. 2.10) as

$$ \boldsymbol{I} = \boldsymbol{R} + \boldsymbol{J}, \tag{2.46} $$

where $\boldsymbol{I}$ is a constant of the motion and $\boldsymbol{J}$ is the sum of all the intrinsic angular momenta of the individual valence nucleons (j_i).

Depending upon the relative effects of the nuclear core deformation and the strength of the Coriolis interaction, there are two extreme limits of nucleon-core coupling that can occur: Deformation Aligned (DAL) or Rotation Aligned (RAL). These limits are the strong-coupling and weak-coupling limits respectively and are illustrated in Fig. 2.11.
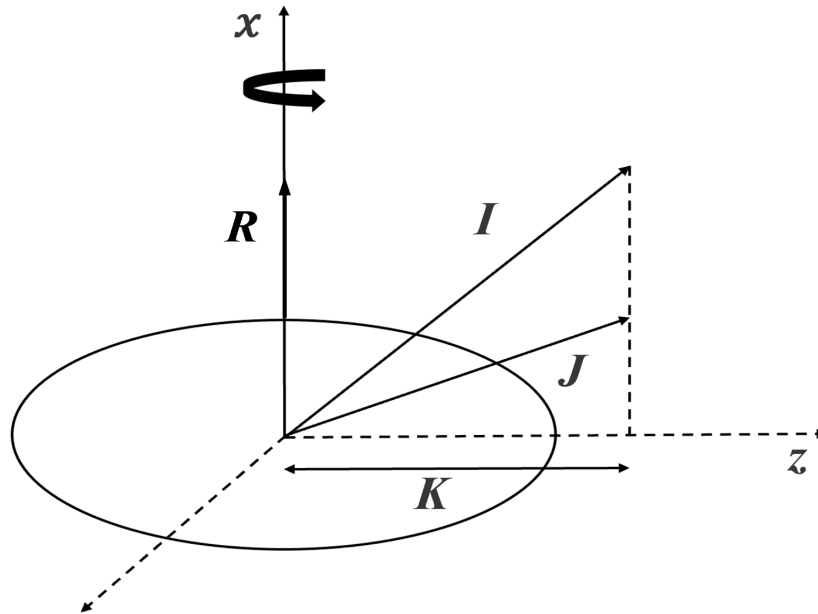
Figure 2.10: Angular momentum coupling in the particle-rotor model. As shown, K is the projection of the total spin on to the symmetry axis z.

(a) DAL

(b) RAL
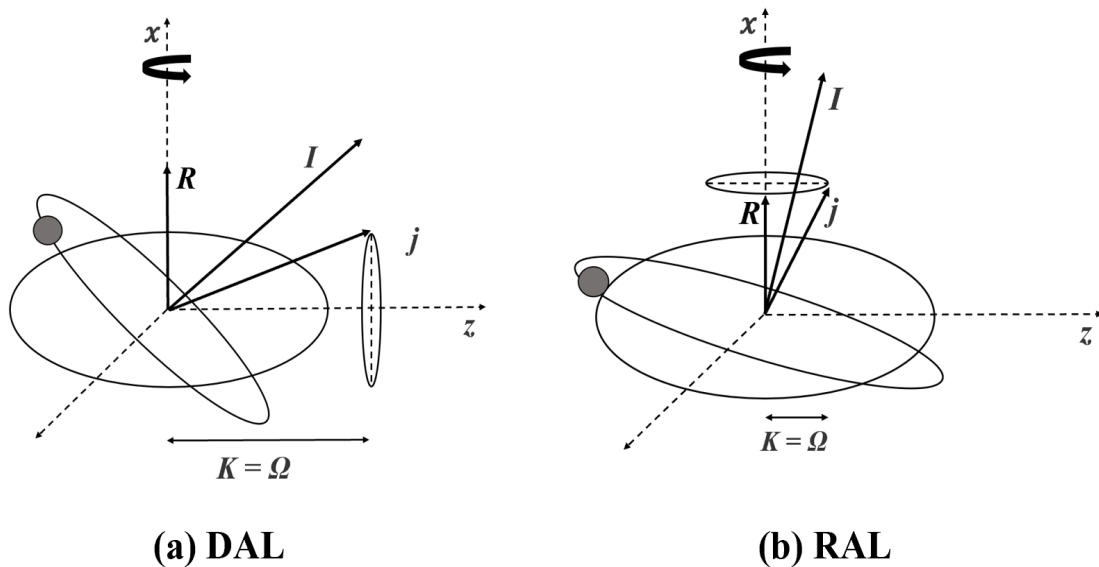
Figure 2.11: Schematic diagrams depicting (a) the Deformation Aligned (DAL) scheme and (b) the Rotation Aligned (RAL) scheme.

In the case of the deformation aligned limit (DAL), this is recognised for well-deformed nuclei with lower rotational frequencies, the odd nucleon is strongly coupled to the collective rotation of the core. When the angular momentum vector, $\boldsymbol{j}$

is coupled to the deformation, the Coriolis effect is only a very small perturbation and is not large enough to align the single-particle orbits with the rotation axis. In this case, K (the total spin projection on the symmetry axis) is approximately a good quantum number, i.e. a conserved quantity, and related to the single-particle momentum projection, Ω by $K = \sum_i \Omega_i$. There is very little signature splitting with the energy levels now given by

$$E_{rot}^K(I) = \frac{\hbar^2}{2\mathcal{J}}[I(I+1) - K^2],\qquad(2.47)$$

with spins of the rotational band being: $I = K, K+1, K+2,...$

In the case of the rotation aligned limit (RAL), this is recognised for more weakly deformed nuclei and faster rotation. The coupling of the unpaired nucleon to the deformed core is negligible due to the much larger strength of the Coriolis Force. The Coriolis interaction aligns the angular momentum of the nucleon, $\boldsymbol{j}$ with the rotation axis, $\boldsymbol{R}$. The odd nucleon's orbit therefore lies in the symmetry plane (that corresponds to the $y - z$ plane), and its wavefunction is what now determines the properties of the band structure. In this case, the larger Coriolis interaction leads to strong K-mixing and signature splitting, thus Ω is no longer a conserved quantity. Energies of the states are given by

$$E_{rot.al}(I) = \frac{\hbar^2}{2\mathcal{J}}(I - j_x)(I - j_x + 1),\qquad(2.48)$$

where $j_x = j$ being a constant of the motion and the vectors precess around the rotation axis, $\boldsymbol{R}$. Spin members of the band are given by $I = j, j+2, J+4, ...$

Band Crossings and Backbending

Backbending is an effect that occurs due to the increasing moment of inertia with increasing rotational frequency, in the rotational bands of deformed nuclei. This behaviour can be attributed to the 'crossing' of two bands – the ground-state band (g-band) and Stockholm band (S-band) [10]. The states that are observed and have the lowest energy configuration for a given spin, are known as the 'yrast' states

(depicted in Fig. 2.12). These states from the yrast band are built upon the ground-state configuration with spins 0^+, 2^+, 4^+...
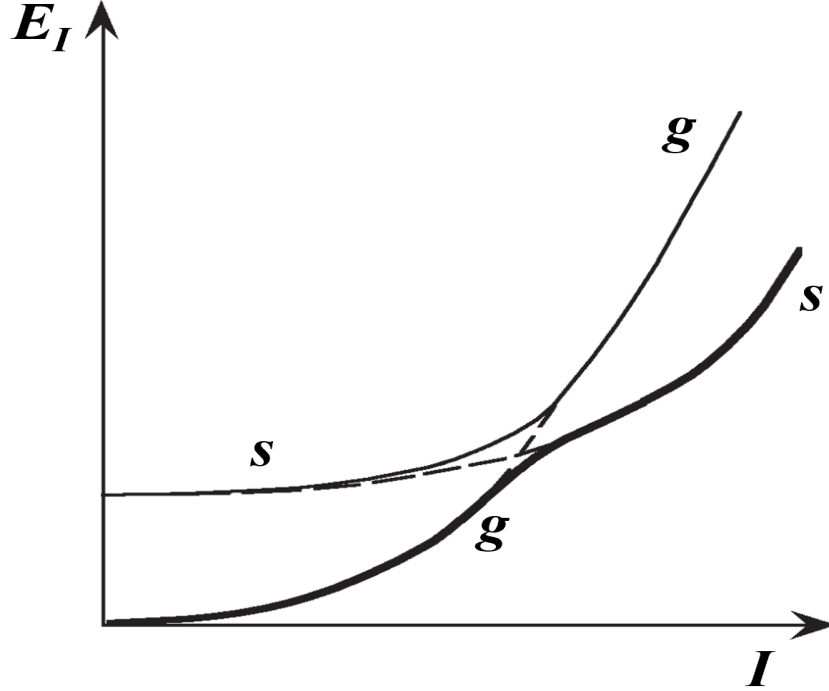
Figure 2.12: Ground-state (g) and Stockholm (s) bandcrossing shown on a plot of energy as a function of total spin. Dashed lines represent the energy levels within each band, and their crossing indicates a change in nuclear configuration. The thick line shows the 'yrast' states.

For the ground-state band, the level energies are given by

$$E_g = \frac{\hbar^2}{2\mathcal{J}_g} I(I + 1). \tag{2.49}$$

For the superdeformed band, from Eq. 2.44 it can be given that

$$E_s = \frac{\hbar^2}{2\mathcal{J}_s} (I - J)^2 + E_J, \tag{2.50}$$

where $E_J \approx 2\Delta \approx 24.A^{-\frac{1}{2}}$ (MeV), and is the energy required to break a pair of nucleons.

The Coriolis force that acts in opposite directions for each nucleon in a pair, can overcome the pairing correlations, thus at a critical frequency (ω_c) the pair will break. Their angular momenta, j_1 and j_2 then align with the rotation axis (Fig. 2.13), increasing the aligned momentum of the s-band [10] by approximately $j_1 + j_2 - 1$. The two bands cross when $E_g \approx E_s$, causing the nucleus to 'change gear' - essentially slowing the nucleus down whilst maintaining angular momentum.
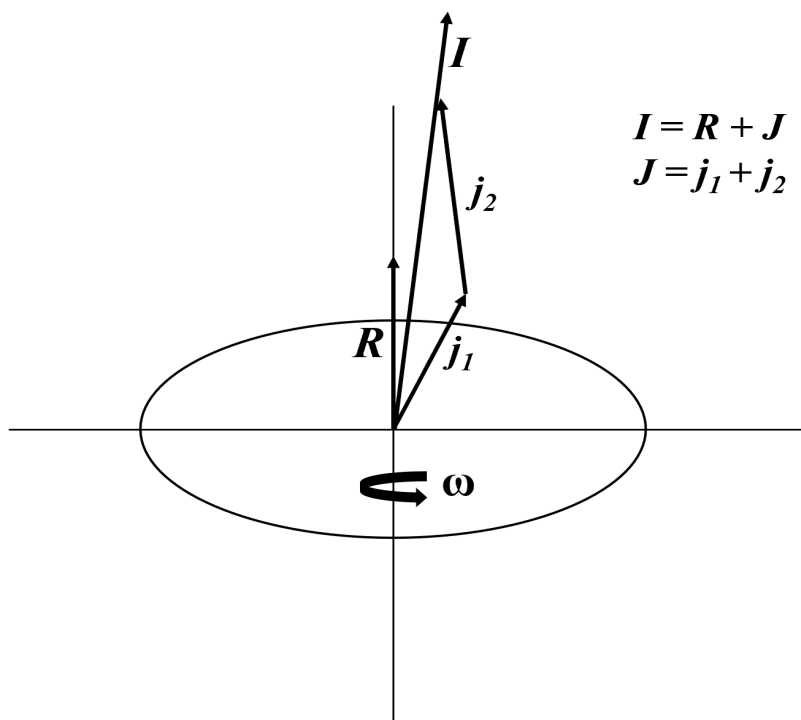
Figure 2.13: The rotational alignment of the angular momenta of a broken nucleon pair, j_1 and j_2, with the rotational axis.

2.5 The Cranked Shell Model

As previously discussed, the collective rotation of a nucleus is related to the shape deformation that may arise as the result of the breaking of symmetry. The 'Cranked Shell Model' (CSM) is a fully microscopic description of the rotating nucleus, derived semi-classically by Inglis [11]. It is able to account for the collective rotation of the externally imposed nuclear field, around an axis (x) perpendicular to the symmetry axis (z). It is rotated with a constant angular velocity, ω around this fixed axis.

The CSM [12] is able to describe the collective angular momentum as a sum of the single-particle momenta. This enables the coupling processes previously discussed to be treated on an equal basis, since the Coriolis and centrifugal effects may be included in the description. By using a coordinate system rotating with a constant angular velocity about the fixed axis, with the correct choice of angular frequency, the nucleons can be thought of as independent particles moving in an average potential well. Since this average field is not symmetric with respect to the rotation axis, the rotation introduces an explicit time dependence to the Schrödinger equation,

$$i\hbar\frac{\partial\phi_L}{\partial t} = H_L\phi_L, \tag{2.51}$$

where ϕ_L and H_L refer to the wavefunction and Hamiltonian in the non-rotating laboratory coordinate frame respectively.

The transformation into the rotating frame can then be achieved using the rotation operator,

$$\mathcal{R}_x = e^{-iI_x\omega t}, \tag{2.52}$$

and

$$\phi_L = \mathcal{R}_x\phi_{int} \quad ; \quad H_L = \mathcal{R}_x H_{int}\mathcal{R}_x^{-1}. \tag{2.53}$$

So the Schrödinger equation in the intrinsic frame becomes,

$$i\hbar\frac{\partial\phi_{int}}{\partial t} = (H_{int} - \hbar\omega I_x)\phi_{int}, \tag{2.54}$$

where ϕ_{int} and H_{int} refer to the wavefunction and the Hamiltonian in the intrinsic frame. Thus, the cranked Hamiltonian (or Routhian) may be defined as

$$H^\omega = H_{int} - \hbar\omega I_x, \tag{2.55}$$

where H_{int} may be seen as the single-particle Hamiltonian. The term $\hbar\omega I_x$ term models the classical Coriolis and centrifugal forces, and its sign is dependent on whether or not the nucleon is moving in the direction of the collective rotation. The presence of this term also leads to the removal of time reversal symmetry.

In terms of the single-particle states, Eq. 2.55 may be written as

$$H^\omega = \sum_i h^\omega(i) = \sum_i (h_{int}(i) - \hbar\omega j_x(i)), \tag{2.56}$$

where h^ω is the sinlge-particle Routhian and $j_x(i)$ are the components of the nucleonic angular momenta projected on to the rotation axis.

The Schrödinger equation in the rotating system can now be solved in the standard ways as an eigenvalue problem. The single-particle Routhian, h^ω, may be evaluated by solving

$$h^\omega|\nu^\omega\rangle = e_\nu^\omega|\nu^\omega\rangle, \tag{2.57}$$

where $|\nu^\omega\rangle$ are the single-particle eigenfunctions in the rotating frame, and

$$e_\nu = \langle\nu^\omega|h_{int}|\nu^\omega\rangle = e_\nu^\omega + \hbar\omega\langle\nu^\omega|j_x|\nu^\omega\rangle. \tag{2.58}$$

The total energy in the rotating frame may now be given by

$$E_{rot} = \sum_{\nu^\omega} e_\nu - \omega \sum_{\nu^\omega} \langle\nu^\omega|j_x|\nu^\omega\rangle, \tag{2.59}$$

and the total angular momentum projection on the rotation axis, I_x is defined as

$$I_x = \sum \langle j_x\rangle_i = \sum \langle\nu^\omega|j_x|\nu^\omega\rangle. \tag{2.60}$$

Differentiation of Eq. 2.58 leads to the single-particle alignment, i_x, given by

$$\frac{de_\nu^\omega}{d\omega} = -\hbar\langle\nu^\omega|j_x|\nu^\omega\rangle = i_x. \tag{2.61}$$

Certain orbitals are most affected by the changes in rotational frequency – those being the ones with large components of angular momentum aligned on the rotation axis and therefore a small Ω component.

2.5.1 Symmetries of the Cranking Hamiltonian

Due to the Coriolis force becoming strong enough to align nucleons with the rotation axis with increasing rotational frequency, the time-reversal symmetry is broken, and the degeneracy is lifted (due to the presence of the ωj_x term in the Hamiltonian). This results in signature splitting, i.e. splitting of each level in to two levels of opposite signature.

The *signature exponent quantum number*, 'α' defines the reflection symmetry of the single-particle Routhian that inhibits invariance with respect to the rotation of $180°$ (π) about the rotation axis, and is often defined as

$$r = e^{-i\pi\alpha}, \tag{2.62}$$

where the signature component is additive. The eigenvalues restrict the spin sequences to:

$$
\left.\begin{array}{lll}
I = 0, 2, 4, ... & \alpha = 0 & r = +1 \\
I = 1, 3, 5, ... & \alpha = 1 & r = -1
\end{array}\right\} \text{ for even } A
$$

$$
\left.\begin{array}{lll}
I = \frac{1}{2}, \frac{5}{2}, \frac{9}{2}, ... & \alpha = +1/2 & r = -i \\
I = \frac{3}{2}, \frac{7}{2}, \frac{11}{2}, ... & \alpha = -1/2 & r = +i
\end{array}\right\} \text{ for odd } A
$$

which may be written more succinctly as

$$I = \alpha \mod 2. \tag{2.63}$$

The only other remaining symmetry in terms of the cranking Hamiltonian is parity, which defines the symmetry with respect to an inversion of the spatial coordinates. The total parity and signature of a configuration is given by

$$\pi_{tot} = \prod_i \pi_i \qquad \text{and} \qquad \alpha_{tot} = \sum_i \alpha_i. \tag{2.64}$$

It is these symmetries that are used to label the single-particle energy levels that will be discussed in further detail in this section.

2.5.2   Pairing

The pairing interaction is a short-range interaction in order to account for nuclear properties that may be observed. It has been experimentally observed in nuclei that the pairing force favours the coupling of nucleons, such that both their spin and orbital angular momenta sum to zero. This explains how the ground states of all even-even nuclei have ground state spins of $I^\pi = 0^+$. Pairing can be explained in terms of time-reversal symmetry, where two nucleons must travel in opposite directions when occupying the same orbital, to satisfy the Pauli exclusion principle (hence why their spins cancels such that $I^\pi = 0^+$) . Further evidence of pairing has also previously been mentioned in section 2.5.2 concerning the moment of inertia, where the nuclear moments of inertia, $\mathcal{J}_{nucl}$ are $\sim 50\%$ lower than the rigid-body moment of inertia, $\mathcal{J}_{rig}$.

Another factor that is experimental evidence of pairing, is the presence of an energy gap, 2Δ, of $\sim 1.5 MeV$ in non-collective excitation energies in even-even nuclei. These gaps are not present in odd-odd nuclei, and as such it can be seen that even-even nuclei near to closed shells exhibit low-lying vibrational states that cannot be explained in terms of single-particle or rotational effects. Thus, the larger

energy needed to break a pair of nucleons in even-even nuclei is evidence of even-even nuclei being more tightly bound due to pairing correlations.

The pairs of particles in time-reversed orbits interact twice per orbit (Fig. 2.14) and so can 'scatter' from one orbit to another time-reversed orbit above the Fermi surface, as a result of the pairing interaction. This scattering of states means that the orbits have different excitation energies, thus smearing out the Fermi surface (Fig. 2.15).
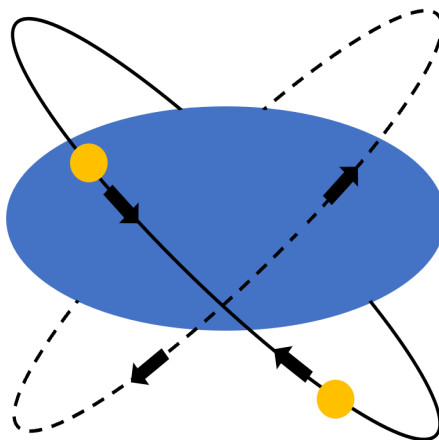
Figure 2.14: An illustration of nucleons scattering from one orbit to another in time-reversed orbits as a result of the pairing interaction.

2.5.3 Cranked Shell Model Calculations and Quasiparticle Routhians

Since the definition between particle-hole states is removed due to the inclusion of pairing correlations, the excitations are more appropriately discussed in terms of particle-hole occupation probabilities. Thus, the concept of quasiparticles (linear combinations of these probabilities) may be introduced to allow the states to be described as being occupied by either a particle or a hole. The probability of the state being occupied is given by V_ν^2 and the probability of the state being unoccupied is given by U_ν^2. Therefore, it is the creation and annihilation of quasiparticles that
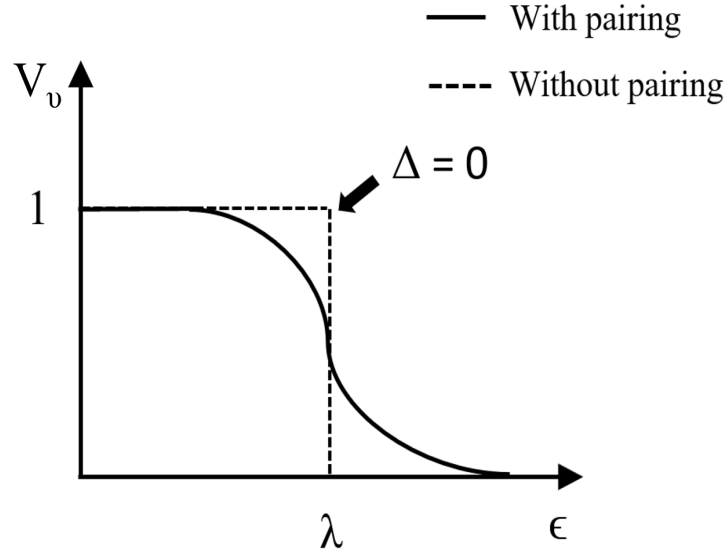
Figure 2.15: An illustration of the effect of pairing on the Fermi surface, with V_ν representing the occupation amplitude. When there is no paring, the Fermi surface is level. With pairing, the Fermi surface is smeared as the nucleons scatter into new time-reversed orbits. This smearing is the origin of the pair gap, Δ.

creates the particle-hole excitations. The transformation of the particle basis into the quasiparticle basis is given by the Bogoliubov-Valatin transformation [13]

$$\alpha_\nu^\dagger = U_\nu a_\nu^\dagger + V_\nu a_{\bar\nu}; \qquad a_\nu^\dagger = U_\nu \alpha_\nu^\dagger - V_\nu \alpha_{\bar\nu}. \tag{2.65}$$

$$\alpha_{\bar\nu}^\dagger = U_\nu a_{\bar\nu}^\dagger - V_\nu a_\nu; \qquad a_{\bar\nu}^\dagger = U_\nu \alpha_{\bar\nu}^\dagger + V_\nu \alpha_\nu, \tag{2.66}$$

where the coefficients U_ν and V_ν represent the occupation amplitudes, such that

$$|U_\nu|^2 + |V_\nu|^2 = 1. \tag{2.67}$$

The quasiparticle energy of a state, $|\nu\rangle$, is defined by

$$E_\nu = \sqrt{(\epsilon_\nu - \lambda)^2 + \Delta^2}, \tag{2.68}$$

where ϵ_ν is the single-particle energy, λ is the Fermi level energy and Δ is the pair gap energy that may be expressed by

$$\Delta = G \sum_{\nu > 0} U_\nu V_\nu, \tag{2.69}$$

with G being a pairing term representing the two-body interaction strength.

The single-particle Hamiltonian in the rotating frame (quasiparticle excitations), obtained from this treatment of the Cranking Hamiltonian given in Eq. 2.56, may be given by

$$h_\nu^\omega = h_{sp} - \Delta(P^\dagger + P) - \lambda \hat{N} - \omega j_x, \tag{2.70}$$

where h_{sp} is the single-particle potential, $\hat{N}$ is the particle number operator, and $P^\dagger$ and P are the pair creation and annihilation operators are defined as

$$P^\dagger = \sum_\nu a_\nu^\dagger a_{\bar{\nu}}^\dagger; \qquad P = \sum_\nu a_{\bar{\nu}} a_\nu. \tag{2.71}$$

It is the eigenvalues from this single-particle Hamiltonian defined in Eq. 2.70, that are the energies of the single-particle levels in the rotating frame or 'Routhians'.

Since the results of CSM calculations provide Routhians as opposed to single-particle energies, it is required that theory is compared to experimental results. The experimental Routhian [14], is given as

$$E_{expt}^\omega(I) = \frac{1}{2} \big[E(I + 1) + E(I - 1) \big] - \omega(I) I_x(I). \tag{2.72}$$

To clearly single out the non-collective effects and remove core contributions, thus obtaining a single-particle quasiparticle Routhian, it is necessary to subtract a parameterised reference band as follows

$$e'(I) = E^\omega_{expt}(I) - E^\omega_{ref}(I), \tag{2.73}$$

where the reference energy, $E^\omega_{ref}(I)$ [14] is given by

$$E^\omega_{ref}(I) = -\frac{1}{2}\omega^2 \mathcal{J}_0 - \frac{1}{4}\omega^4 \mathcal{J}_1 + \frac{1}{8}\frac{\hbar^2}{\mathcal{J}_0}. \tag{2.74}$$

As shown, Eq. 2.74 is inclusive of terms that introduce the Harris parameters [15], $\mathcal{J}_0$ and $\mathcal{J}_1$ that are used to obtain the experimental alignments, i_x, given by

$$i_x = I_x(I) - I_{x,ref}(I), \tag{2.75}$$

where $I_{x,ref}(I)$ is given by

$$I_{x,ref}(I) = \omega\left[\mathcal{J}_0 + \mathcal{J}_1\omega^2\right]. \tag{2.76}$$

Both quantities in Eq. 2.74 and Eq. 2.76 are obtained using a reference configuration with a variable moment of inertia given by

$$\mathcal{J}^{(1)}_{ref} = \mathcal{J}_0 + \mathcal{J}_1\omega^2. \tag{2.77}$$

The choice of specific Harris parameters used can be taken from literature, as is the case in Chapters 5 and 5 of this work. The deformed Woods-Saxon potential (Eq. 2.28) previously discussed in section 2.4.3, is a popular choice of single-particle potential that is used to carry out Cranked Shell Model (CSM) calculations. The specific deformation parameters required are calculated using Total Routhian Surface (TRS) calculations. Using the relevant software, it is then possible to generate a Woods-Saxon quasiparticle diagram, that shows the quasiparticle Routhian energies, e', against the rotational frequency, $\hbar\omega$. These calculations will be shown in

Chapters 5 and 6 of this work, and the labelling convention for such diagrams is shown in Table 2.1.

Table 2.1: Table showing the convention for labelling quasiparticle Routhians for both protons and neutrons.

(π, α)	Protons	Neutrons
$(+, +\frac{1}{2})$	A, C, . . .	a, c, . . .
$(+, -\frac{1}{2})$	B, D, . . .	b, d . . .
$(-, +\frac{1}{2})$	F, H, . . .	f, h, . . .
$(-, -\frac{1}{2})$	E, G . . .	e, g, . . .

The quasiparticle levels at $\hbar\omega = 0$ can be labelled using the Nilsson quantum numbers, as described in section 2.4.2. With increasing rotational frequency, due to the Coriolis and centrifugal forces, the Nilsson levels split into two levels that are identified using the parity and signature (π, α) quantum numbers: solid line $(+, +1/2)$, dotted line $(+, -1/2)$, dot-dash line $(-, +1/2)$ and dashed line $(-, -1/2)$. The evolution of nuclear structure from spherical nuclei using the shell model, to when deformation and rotations are applied using CSM calculations, is shown in Fig. 2.16.
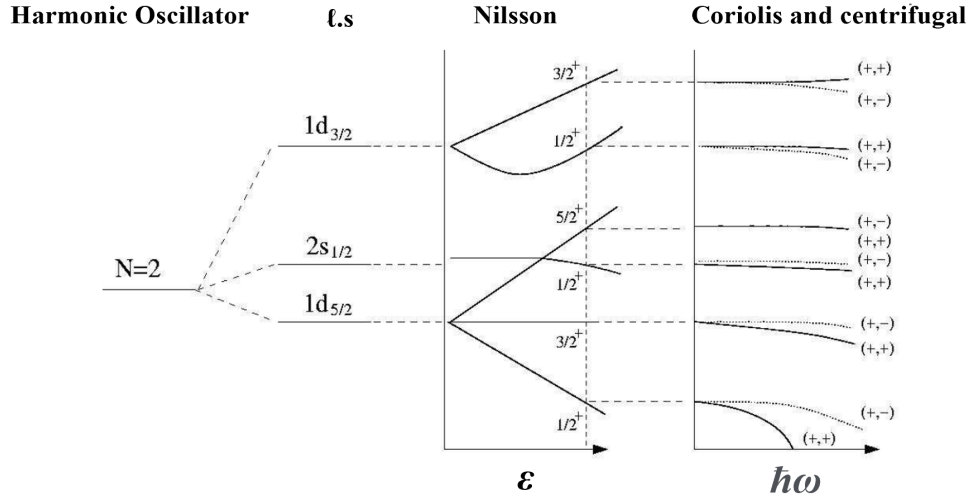
Figure 2.16: A schematic diagram showing the shell model states for various nuclear potentials. The single-particle states for spherical nuclei are calculated using the shell model, for deformed nuclei the states are calculated using the Nilsson model, and when rotation is applied, the CSM is used.

Orbitals that interact are labelled as a bandcrossing (previously discussed in section 2.5.2). Since the signature quantum number must be conserved at a crossing, these interacting orbitals must have opposite signature. If one of the interacting levels is occupied by a particle, this particle essentially 'blocks' this level and so the crossing cannot take place.

Quasiparticle levels that have the same signature and parity will not cross, but each level will exchange character at the point of interaction between the levels.

The alignment or 'aligned angular momentum' describes the non-collective component of the nuclear spin that is projected on to the rotation axis. It is of great interest to study the alignments in rotating nuclei, as it is a quantitative measure of how well the spins of the excited nucleons line up with the collective spin. A useful feature of these diagrams is that the slopes of two interacting levels can be used to calculate the theoretical gain in alignment at a crossing, given by

$$\Delta i_x = -\frac{1}{\hbar} \sum_\nu \frac{de_\nu}{d\omega}. \tag{2.78}$$

Such bandcrossings occur when the Coriolis force becomes strong enough to break a pair of nucleons in time-reversed orbits and align their orbital angular momenta with the rotation axis. The result is the signature splitting of levels with the same parity, at a definitive value of rotational frequency.

The significance of a bandcrossing is that it is showing a change in the internal structure of the nucleus, and deformed (rotational) bands will become yrast. Information about the bandcrossings can also be seen from quasiparticle Routhian diagrams - the distance between interacting levels is smaller for a backbend (weaker interaction) than would be observed should it be an upbend (stronger interaction).

2.6   Superdeformation

The phenomenon of superdeformation arises when the decay processes proceed from metastable states, in a secondary potential minimum in the fission barrier.

Nuclear shapes arise from the interplay between collective rotation and the quantal structure of valence nucleons. It is the interplay of these that causes the shape of a nucleus to be either oblate or prolate. For nuclei rotating at sufficiently high angular momentum, a prolate shape with a major-to-minor axis ratio of 2:1 is favoured (experimentally observed in ^{152}Dy [16] for example).

Within the mass region of $A \approx 130$, experimental data have also revealed nuclei with a major-to-minor axis ratio of 3:2 (seen in ^{132}Ce [17] for example), following the observation of the discrete γ-ray spectra observed.

The experimental signature of such superdeformed shapes, is the γ-ray sequence of very regular spacing, the energies of which are given by

$$\Delta E = \frac{\hbar^2}{2\mathcal{J}}((I+1)(I+2) - (I-1)I) = \frac{\hbar^2}{2\mathcal{J}}(4I+2). \qquad (2.79)$$

It is this particular mass region that is being investigated using the experimental set-up outlined in Chapter 4, with the aim of studying such γ-ray spectra in order to reveal more information about the internal structure of the nuclei produced, and phenomena observed during their decay.

2.7 Rare-Earth Deformed Nuclei in the $A \approx 130$ Region

The mass region, $A \approx 130$ is known to extend from around the nucleus ^{132}Sn (doubly magic) into the deformed region below $N = 82$ and above $Z = 50$. This region reflects the experimental studies that have been carried out, showing a range of rotational structures that can be explained by the various shape-driving effects that occur due to the role of valence and intruder orbitals. Figure 2.17 shows a portion of this mass region, specifically with the nuclei of interest in this work. Nuclei in this region have been observed to show changes in shape from triaxial to prolate at higher spins. The interplay between the collective and single-particle angular momenta of these valence nucleons, is what impacts how a triaxial nucleus will rotate. Both protons and neutrons are occupying the same major shells, and the deformed structures are built on configurations involving the $h_{11/2}$ shell (Fig. 2.7). Valence protons occupy the low-Ω orbitals from the bottom of the $h_{11/2}$ subshell, driving the nucleus to prolate deformations. Under the influence of the Coriolis force, the protons at the Fermi surface are aligned rapidly with the axis of rotation, whilst valence neutrons occupy the high-Ω orbital from the top of the $h_{11/2}$ subshell, driving the nucleus to adopt an oblate shape.

As the neutron number decreases, this means the neutron Fermi level approaches that of the protons (i.e. both the proton and neutron Fermi surfaces are expected to be at similar levels in the $h_{11/2}$ subshell), thus increasing the possibility of proton-neutron interactions [19]. As the nuclei become more neutron deficient, an increase in deformation can be seen towards the proton drip line.

The nuclear cores in this region are known to have properties that are in agreement with them being soft with respect to the triaxiality parameter, γ [20]. The ideal triaxial shape is known to have the parameter of values: $\gamma = \pm 30°$ or $-90°$ [21], whereby in the Lund convention, the shapes with the γ parameters of these values correspond to the axis about which the nucleus rotates (Fig. 2.5): for $\gamma = 30°$, rotation is around the short axis, for $\gamma = -30°$, rotation is about the intermediate axis, and for $\gamma = 90°$, rotation is about the long axis. It is the shape changes driven by the rotational alignment of quasiparticles, that means these γ-soft cores are par-
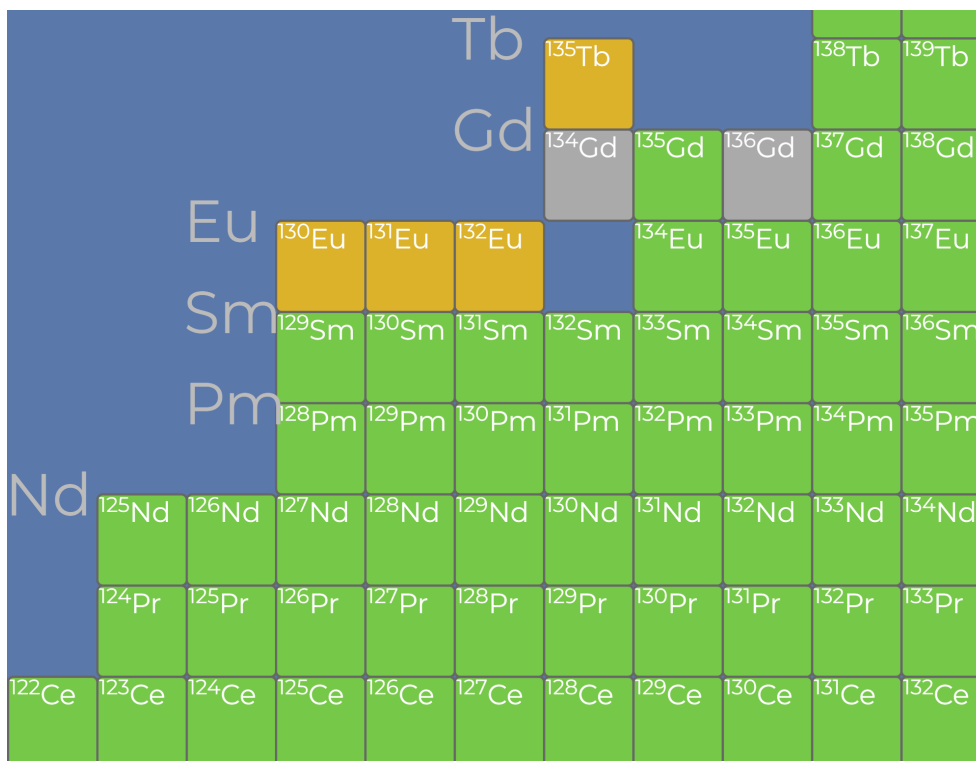
Figure 2.17: A selected portion of the Segre chart, highlighting some of the nuclei of interest in the mass region $A \approx 130$ [18].

ticularly susceptible to the polarising effects of the valence orbitals, at specific values of γ.

Another factor that it thought to be of importance in driving the deformation towards highly elongated prolate nuclear shapes, is the presence of intruder states (unnatural parity states) that arise from the spin-orbit coupling. The orbitals with higher angular momentum are then lowered in energy, so that they then reside amongst levels with opposite parity. These neutron intruder states originate from the $f_{7/2}$, $h_{9/2}$ and $i_{13/2}$ subshells and shell closures. An example of this is the $i_{13/2}$ intruder state originating from the $N = 6$ oscillator shell (with a positive parity) that is lowered to the $N = 5$ oscillator shell (with a negative parity) containing the $h_{11/2}$ subshell. It is accepted that within this region, the occupation of the $i_{13/2}[660]_{1/2}$ orbital is what polarises the core, thus playing a fundamental role in stabilising the nuclear shape [22]. Deformed bands involving the $i_{13/2}$ neutron intruder orbital have been observed in several isotopes of nuclei with $N \geq 72$ including Ce, Sm and Nd [23][24][25]. It has also been noted experimentally in Pr isotopes that proton holes in the $g_{9/2}$ orbital also play an important role in driving deformation in this region

[26][27]. It is all of these components, as well as the single-particle energy gaps at $Z = 58$ and $N = 72, 74$ [22] that all play roles in establishing the second minimum that gives rise to superdeformation.

Chapter 3

Gamma-Ray Spectroscopy

This section will give a brief overview of the theory of γ decay, as well an overview of the aspects of γ spectroscopy that are relevant to the experimental details included in this report. A full description of the electronics and data acquisition system is beyond the scope of this work, however a general overview of these aspects will be discussed here, alongside the experimental setup and methodology used to acquire data.

The use of γ spectroscopy is one of the primary methods used to obtain information about nuclear structure. It is achieved by displaying a full spectrum of γ rays that are emitted from highly excited nuclei, showing the energies and intensities of each of the transitions. Most γ transitions will occur in a time period of $< 10^{-12}$ s, however if this time period is $> 10^{-9}$ s then de-excitations are known as *isomeric*.

3.1 Gamma-Ray Interactions

There are three interactions of γ rays with matter that are known to have significance in γ-ray spectroscopy: Photoelectric absorption, Compton scattering and pair production. These processes involve either the total or partial energy transfer of the photons to the electrons of the absorber.

Photoelectric Absorption

Photoelectric absorption involves the interaction of an incoming γ ray with a bound atomic electron, with the production of a photoelectron possessing the energy of the incident γ ray absorbed, given by

$$E_e = hv - E_B, \qquad (3.1)$$

where hv is the energy of the incident γ-ray photon and E_B is the binding energy of the electron. Often in this process, a characteristic X-ray is often emitted. Should the photoelectric absorption occur near the surface of the detector, the X ray may escape, thus producing another peak that is located below the full-energy peak. The photoelectric effect is mostly prominent at low γ-ray energies (up to several hundred keV).

Compton Scattering

Compton scattering is a process involving the interaction of an incoming γ ray (E_γ) with a loosely bound atomic electron. This results in the creation of a recoil electron (m_e) and a scattered γ-ray photon (E_s), where the energy transferred in this interaction is dependent on the scattering angle, θ. This relationship is given by

$$E_s = \frac{E_\gamma}{1 + \frac{E_\gamma}{m_e c^2}(1 - \cos\theta)}. \qquad (3.2)$$

In a large number of circumstances, all scattering angles occur in the detector, thus a continuum of energies may be transferred up to a maximum energy known as the *Compton Edge*. Beyond this is where the full-energy peak or 'photopeak' may be observed. Compton scattering is the dominant process for γ-ray energies from around 200-1000 keV.

Pair Production

Pair production refers to when an electron-positron pair is created at the disappearance point of the incident γ-ray photon. Since this process requires an energy of $2m_0c^2$, to make this process energetically possible it requires a minimum γ-ray energy of around 1.022 MeV. Any excess energy above this goes to the kinetic energy of the electron and positron. Following the disappearance of the γ ray into the Coulomb field of the nucleus and production of the electron-positron pair, the positron will subsequently annihilate into two photons (each of energy 511 keV) that may subsequently detected.

Other secondary radiations that can be created near the source must also be taken into account, since they may be observed and recorded in the spectrum. These include *annihilation radiation* (possible peak observation at around 0.511 MeV) and *Bremsstrahlung* (generated during the absorption process). A *backscatter peak* is another effect that may be observed in the spectrum in the vicinity around 0.2-0.5 MeV, and this is caused by the Compton scattering of γ rays from the source through large angles by first interacting with material surrounding the detector.

3.2   Fusion-Evaporation Reactions

In order to further understand the collective properties of nuclei, it is necessary to observe the characteristic γ-decay of the specific nucleus being investigated. For the study of the nuclei of interest within this work, it is desirable to use a reaction method that enables the synthesis of heavy nuclei in high-spin excited states, populating channels with as much angular momentum as possible. Heavy-ion fusion evaporation reactions (Fig. 3.1) allow for the population of states with such angular momentum and significant cross-sections. A compound nucleus is formed by bombarding a stationary target nucleus with a projectile nucleus, whereby the induced angular momentum of the compound system is dependent on the impact position of the projectile on the target. This relationship may be given by

$$\overrightarrow{l} = \overrightarrow{b} \wedge \overrightarrow{p}, \tag{3.3}$$

where l is the angular momentum of the compound nucleus, b is the impact parameter and p is the momentum of the projectile. Following the formation of the compound nucleus (around 10^{-22} s after impact), the residual nucleus of interest is obtained by the 'boiling off' of the relevant amount of nucleons which cool the system towards the particle evaporation threshold (occurs at around 10^{-19} s). At this stage, large amounts of energy are carried away, however little angular momentum is lost at this point. Subsequently, at around 10^{-15} s, angular momentum and energy are lost via the emission of statistical γ rays as the nucleus 'cools' towards the yrast line. After around 10^{-12} s following the initial formation of the compound nucleus, electric quadrupole (E2) γ-ray cascades now enable the nucleus to dissipate angular momentum. After around 10^{-9} s and 10^{11} rotations, the nucleus then decays to its final ground-state energy.
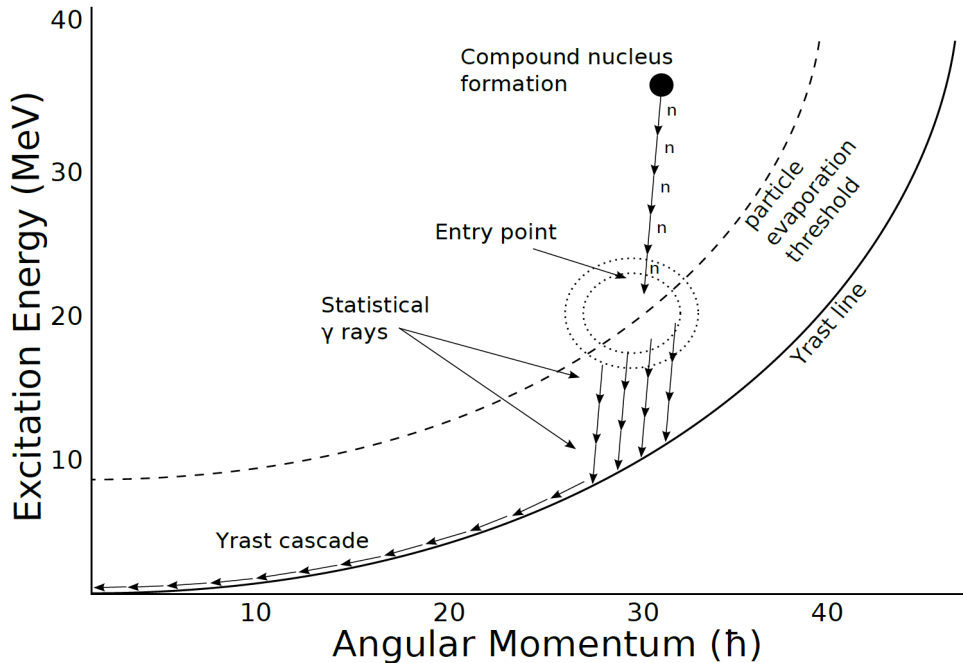
Figure 3.1: A schematic showing a five particle (nucleon) exit channel of a fusion-evaporation reaction. Once the particle-evaporation threshold is reached, angular momentum and energy are lost via statistical γ rays.

3.3 Gamma Decay

Following the production of the highly excited nuclei that are produced via fusion-evaporation reactions, these nuclei then decay rapidly via electromagnetic transitions (either γ decay or internal conversion). It is these electromagnetic transitions that specifically enable the decaying nucleus to lose energy, and allow information about the nuclear structure to be obtained from the radiation that is detected.

Following most α and β decays, the nucleus is left in an excited state, decaying rapidly to the ground state through the emission of one or more γ rays. The energy emitted by these γ rays is what allows the nucleus to obey the laws of conservation when transitioning between the initial and final states. It is the conservation of momentum and parity of these electromagnetic transitions, that enable the deduction of the properties of the levels from the multipolarity.

In order to conserve linear momentum, the nucleus will also have a recoil momentum that corresponds to the recoil kinetic energy, T_R, such that

$$E_i = E_f + E_\gamma + T_R, \tag{3.4}$$

where E_i and E_f are the excitation energies of the initial and final state angular momenta respectively, and E_γ is the γ-ray energy. Another requirement is that the angular momentum during the transition is also conserved,

$$\vec{I_i} = \vec{L} + \vec{I_f}, \tag{3.5}$$

where $\vec{I_i}$ and $\vec{I_f}$ are the initial and final state angular momentum respectively, and $\vec{L}$ is the multipolarity. Values of L are restricted since each of these three vectors must form a closed vector triangle, yielding the following relationship,

$$|I_i - I_f| \leq L \leq I_i + I_f. \tag{3.6}$$

It is then the conservation of parity between the initial and final states that determines if the transition is either electric (E) or magnetic (M). Table 3.1 displays the angular momentum and parity selection rules, whereby there is one exception

for the case when $I_i = I_f$ due to there being no monopole ($L = 0$) γ transitions. Generally, based on single-particle estimates, it is the lowest multipole that will dominate during de-excitation and magnetic transitions are hindered compared to their corresponding electric transitions.

Table 3.1: Angular momentum and parity selection rules for both electric and magnetic radiation.

$|I_i - I_f|$	1	2	3	4	5
No change of parity	M1	E2	M3	E4	M5
Change of parity	E1	M2	E3	M4	E5

Based on the assumption that a single particle is responsible for the transition, theoretical estimates for the half-lives of a γ-decaying state were proposed by Weisskopf [28]. Whilst these are considered estimates, they are taken into account when assigning the multipolarities of γ-ray transitions, as well as assessing the single particle nature of a transition. Based upon these estimates (Table 3.2), it is expected that all transitions cascade with multipolarities of E1, E2 and M1.

Table 3.2: Estimates of the half-lives based on Weisskopf estimates for electric (E) and magnetic (M) transitions for the first four orders of multipolarity. Here A is the mass number and E_γ is the γ-ray energy in MeV.

L	E (s^{-1})	M (s^{-1})
1	$1.0 \times 10^{14} A^{\frac{2}{3}} E^3$	$5.6 \times 10^{13} E^3$
2	$7.3 \times 10^7 A^{\frac{4}{3}} E^5$	$3.5 \times 10^7 A^{\frac{2}{3}} E^5$
3	$3.4 \times 10^1 A^2 E^7$	$1.6 \times 10^1 A^{\frac{4}{3}} E^7$
4	$1.1 \times 10^{-5} A^{\frac{8}{3}} E^9$	$4.5 \times 10^{-6} A^2 E^9$

3.4 Semiconductor Detectors

In crystalline materials, the periodic lattice making up their structure is what establishes the allowed energy bands for electrons, that are separated by *band gaps* (forbidden regions). The electrical conductivity can be defined by a simplified representation of these bands – both valence and conduction bands, separated by a band gap. The valence band is one which corresponds to electrons that are bound to specific sites within the crystal lattice, and do not contribute to the conductivity within the material. The conduction band represents those electrons that are free to move within the crystal. It is the size of the band gap that determines if a material is an insulator or a semiconductor. In both materials, the valence gap is completely filled with electrons, however the band gap energy is smaller in semiconductors than that in insulators. Thus, thermal excitations can promote electrons across the band gap into the conduction band. Physically, this corresponds to the breaking of a covalent bond in the crystal, creating an electron in the conduction band, as well as leaving a 'hole' in the valence band. This combination is what is known as an *electron-hole pair* and it is the motion of these charge carriers that contributes to the overall conductivity of the material.

In radiation detection, semiconductor detectors are those that measure the number of charge carriers (within the detector material itself situated between two electrodes) that are set free by ionising radiation. The principle is based upon this ionising radiation generating electron-hole pairs along the path taken by the charged particle in the detector. It is their motion in an applied electric field that generates an electric signal from the detector – the charge is proportional to the energy of the incoming photons, and it is this that is converted into a voltage pulse by a preamplifier.

In any crystal that is a completely pure semiconductor, i.e. undoped, there is an intrinsic charge flow where the concentration of electrons in the conduction band (n) is equal to the concentration of holes in the valence band (p). The addition of impurities to the semiconductor material, also known as *doping*, is a way of increasing the concentration of carriers, thus increasing the conductivity. Two types of semiconductors are the result of doping in this manner: An *n-type* semiconductor is one which has been doped with electron donor atoms, so the majority of the charge

carriers are electrons, whereas an *p-type* semiconductor is one which has been doped with electron acceptor atoms, so the majority of the charge carriers are holes.

A major source of the degradation of energy measurements in the detector, arises from the noise resulting from the random intrinsic charge flow. In order to avoid this, a $p-n$ junction can be formed by placing n-type and *p*-type semiconductors in direct contact. When such contact is made, the electrons and holes from the *n*-type and *p*-type semiconductor materials respectively, are both free to diffuse from regions of high concentration to low concentration. This creates what is known as a *depletion region*, the result of which is the inhibition of further charge flow across the junction. It is within this region in which the detection of γ rays occurs. To further increase the efficiency of γ-ray detection, a reverse-bias voltage can also be applied in order to increase the thickness of this depletion region, given by

$$d = \left[\frac{2\epsilon V}{eN} \right]^{\frac{1}{2}},\qquad(3.7)$$

where V is the voltage of the reverse-bias, ϵ is the ionisation energy, e is the electron charge, and N is the net impurity concentration in the material [29]. As large a depletion region as possible is desired in semiconductor detectors, due to γ rays being deeply penetrating.

Silicon Detectors

Silicon strip detectors are often used to measure the trajectories and positions of charged particles. Such detectors work by the doping of narrow strips of silicon in order to turn them in to diodes. They are then reverse biased so that when a charged particle passes through them, a small ionisation current can be measured and detected. The use of double-sided silicon strip detectors (DSSD) (as used in the experimental setup explained in Chapter 4), measures two coordinates (x and y) in a detector layer. The highly doped n-type or p-type silicon strips are positioned orthogonal to one another in order to enable such two-coordinate measurements.

High-Purity Germanium Detectors

As previously discussed, within γ-ray spectroscopy it is desirable to have as thick a depletion region as possible, due to the high penetration depths of γ rays. Depletion depths of greater than 2-3 mm are difficult to achieve when using silicon or germanium of normal semiconductor purity. Following on from Eq. 3.7, a greater depletion depth may be achieved by reducing the net impurity concentration, N.

High-purity germanium (HPGe) detectors with such low impurities are now available with depletion depths of up to several centimetres. Due to γ rays being highly penetrating, it is of great importance to produce detectors of larger volumes for γ-ray spectroscopy. Most commercially produced HPGe detectors use lithium diffusion to make an n^+ ohmic contact, and boron implantation to make a p^+ ohmic contact. Two types of HPGe crystal material may be produced, either of high-purity p or n type - cross-sections of each of these perpendicular to the crystal's cylindrical axis are depicted in Fig. 3.2. Under the applied reverse bias, an electric field is extended across the intrinsic region - it is when photons interact with material in this region that charge carries (e^- and h^+) are swept to the p and n electrodes.
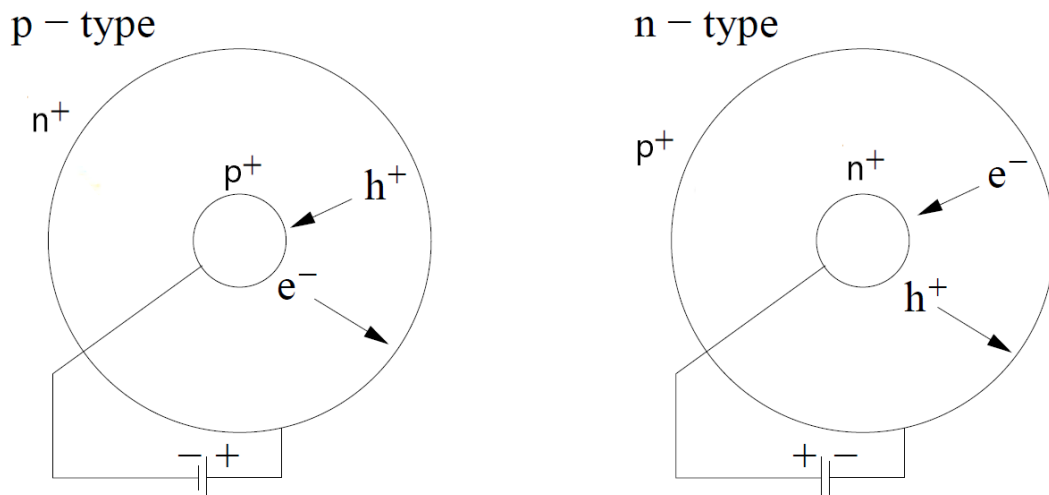
Figure 3.2: A schematic diagram of the cross-sections of p-type and n-type coaxial detectors, perpendicular to the cylindrical axis of the crystal, also showing the applied reverse bias. The flow of electrons and holes upon incident γ rays are shown by e^- and h^+ respectively. Adapted from [29].

In order to avoid leakage current complication, it is also desirable to choose a closed-ended coaxial configuration (as opposed to planar-geometry) (Fig. 3.3). Another advantage of this geometry is the ability to fabricate larger-volume detectors with lower capacitance, due to the smaller inner diameters being used.

n-type   **p-type**

n$^+$ contact   p$^+$ contact

p$^+$ contact   n$^+$ contact
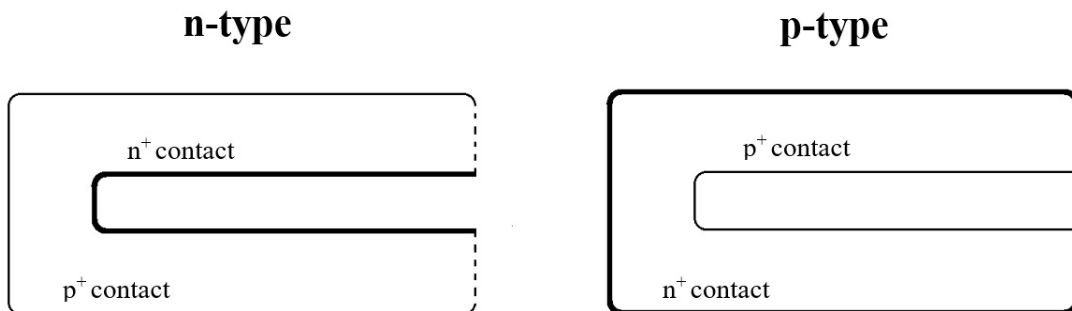
Figure 3.3: A schematic showing the cross-section through the axis of a bulletised coaxial germanium detector. Adapted from [29].

It is also a requirement that HPGe detectors are cooled to liquid nitrogen temperatures (77 K). Higher temperatures would result in the thermal excitation of electrons, enabling them to cross the band gap in the crystal to the conduction band, thus contributing to electrical noise. The cooling to such low temperatures therefore ensures the output of useful spectroscopic data.

3.5   Compton Suppression

As previously mentioned in section 3.1, most of the γ rays discussed in this research will interact by Compton scattering. When incident γ rays are scattered according to the relation described in equation 3.2, it is possible that unlike with the photo-electric effect, the scattered γ rays may only deposit a small part of their energy prior to escaping the volume of the detector. The result of this is an undesirable continuum background. In order to suppress this Compton background, it is necessary to surround the HPGe crystals in traditional detector arrays with an inorganic scintillator that is used in anti-coincidence mode. The material of choice in this particular experimental setup is Bismuth Germanate (BGO). It is the most commonly

used material for this purpose due to its high atomic number (Z=83), meaning it has a high efficiency for stopping γ rays. Consequently, any escaped γ rays are detected in the BGO shield and rejected from the data stream. The use of a BGO shield for Compton suppression also improves the peak-to-total ratio (the ratio of full-energy peak counts to the counts in both the peak and the background) from 0.2 (for unsuppressed detectors) to 0.6 (with suppressed detectors), as is the case for the JUROGAM3 array in the JM06 experiment [30].

3.6 Recoil Separators

The main purpose of a recoil separator is to separate the unreacted primary beam, from the fusion products that result from fusion-evaporation reactions. Such fusion products are collected at the focal plane setup for further analysis. Generally all separators are comprised of comparable electromagnetic elements, such as electric and magnetic dipoles (to achieve separation), as well as magnetic quadrupoles (to focus the resulting ions at the focal plane). Recoil separators fall into two categories: vacuum separators and gas-filled separators. They are complementary devices and the choice of separator is unique to each experiment and very much dependent on the desired preferences for data collection and the foreseen research. Gas-filled separators (e.g. RITU - Recoil Ion Transport Unit) are generally more simple in setup and have a high efficiency. They are better for asymmetric reactions and provide an average charge state. Since they also have poorer beam suppression for symmetric reactions and no mass resolution, this is where a more general-purpose vacuum separator such as MARA may be preferable. Vacuum separators have a lower efficiency and are more complex in setup, however, they have good beam suppression and the capability of physically separating the fusion products based on their mass-to-charge (A/q) ratio. Taking these factors in to consideration, the mode of separator chosen for this particular experiment is discussed further in section 4.2 of this work.

3.7 Gamma-Ray Spectrometer Arrays

As discussed in section 3.2, the nuclei following fusion-evaporation reactions are in highly-excited spin states with a high angular momentum. Following this, the cascade of γ rays emitted allows us to obtain information about the nuclear structure. The use of large spectrometer arrays has allowed for improvements in the desirable features within high-spin spectroscopy experiments, namely the photopeak efficiency, the energy resolution and the peak-to-total ratio.

The total photopeak efficiency is measured using a known γ-ray source, and is dependent on the geometry of the detector itself, as well as the distance between the detector and the source. It may be defined as the ability of the detector array to detect any incident γ rays. Optimally, such arrays of HPGe detectors are arranged to cover as much of the 4π solid angle as possible, thus increasing efficiency. The energy resolution is a reflection of the ability of the detector to distinguish between γ rays of close energies, i.e. the better the resolution, the better the separation of two distinct peaks. The intrinsic energy resolution of an HPGe detector is typically around 2 keV at 1.33 MeV. Since detected γ rays are emitted from recoiling nuclei, the Doppler effect is also another factor that contributes to the degradation of the resolution. Doppler broadening (section 4.4.3) occurs due to the opening angle of the detector, the angular spread of the recoils, and the velocity (energy) spread of recoiling nuclei. Thus, the overall detector resolution is a combination of the aforementioned considerations. The peak-to-total ratio defines the relationship between the area of the photopeak and the total area in the spectrum. This ratio is around 0.6 for 1.33 MeV in escape-suppressed HPGe detectors.

In order to obtain an indication of the performance of a detector array, and therefore the quality of the spectra obtained, it is important to look at the resolving power, R, defined as

$$R = \frac{SE_\gamma}{\Delta E_\gamma} \frac{P}{T},\tag{3.8}$$

where SE_γ is the average energy separation in a γ-ray cascade, ΔE_γ is the resolution of the γ rays in the spectrum, and $\frac{P}{T}$ is the peak-to-total ratio. Since SE_γ is dependent on the structure of the nucleus, it may be deduced from this relation

that the resolving power can only be improved by improving the resolution or peak-to-total ratio. The peak-to-total ratio must be large enough to distinguish the peaks from the fluctuating background. This background may be calculated by assuming that there is an average energy separation (SE_γ) of the transitions in a cascade, and also that it is not correlated with peak events.

For Compton-suppressed detectors it is difficult to improve upon the peak-to-total ratio, however by using high-fold coincidences, some improvements can be made, as shown by the relation

$$\left[\frac{N_p}{N_b}\right]_F = \alpha_0(0.76R)^F R_0, \tag{3.9}$$

where N_p is the number of counts in the peak region and N_b is the nuber of counts in the background region, thus $\left[\frac{N_p}{N_b}\right]_F$ is the peak-to-total ratio when applying a fold criterion to the data. The term α_0 is an observational limit of the array dependent on the resolving power, R and the total photopeak efficiency [31]. The value 0.76 relates to the consideration of an F-dimensional volume element decided by the FWHM of the peak. The background-reduction factor, R_0, is a further improvement to selectivity, resulting from the use of complementary devices such as recoil separators.

Chapter 4

Experimental Apparatus and Data Analysis

This chapter will give an overview of the experimental apparatus that was used to obtain the data in this work, as well as an outline of the various analysis techniques used in order to process the data. An understanding of the experimental apparatus and the software used to extract the results, forms the basis of further analysis that will be discussed in Chapters 5 and 6.

4.1   The JUROGAM3 Spectrometer Array

As previously discussed in Chapter 3, nuclei in high-spin excited states are produced via fusion-evaporation reactions, which then de-excite via a cascade of γ rays. The JUROGAM3 array [32] of Compton-suppressed HPGe detectors (24 Clover detectors [33] and 15 Phase I-type detectors [34]) shown in Fig. 4.1), is constructed to measure the prompt γ rays produced at the target position of the MARA recoil separator. This is the same configuration as its predecessor JUROGAM II, with the added advantage of the ability to move it efficiently between both the MARA [35] and RITU [36] separators. The full array of detectors consists of 39 detector modules with 111 individual germanium crystals. Five of these detector modules are the Phase I-type detectors that are mounted in a ring at 157.6°, whilst another ten of these modules are mounted in a ring at 133.5° with respect to the beam axis. Two

further rings are mounted at 104.5° and 75.5° with respect to the beam axis, with each ring housing 12 detector modules consisting of clover detectors. The HPGe crystals contained within the array are n-type material and measure around 75 mm in length, have a diameter of around 70 mm and are tapered over the front 30 mm [30]. The full JUROGAM3 spectrometer array yields a total photopeak efficiency of 5.2% for 1332 keV γ rays [32].
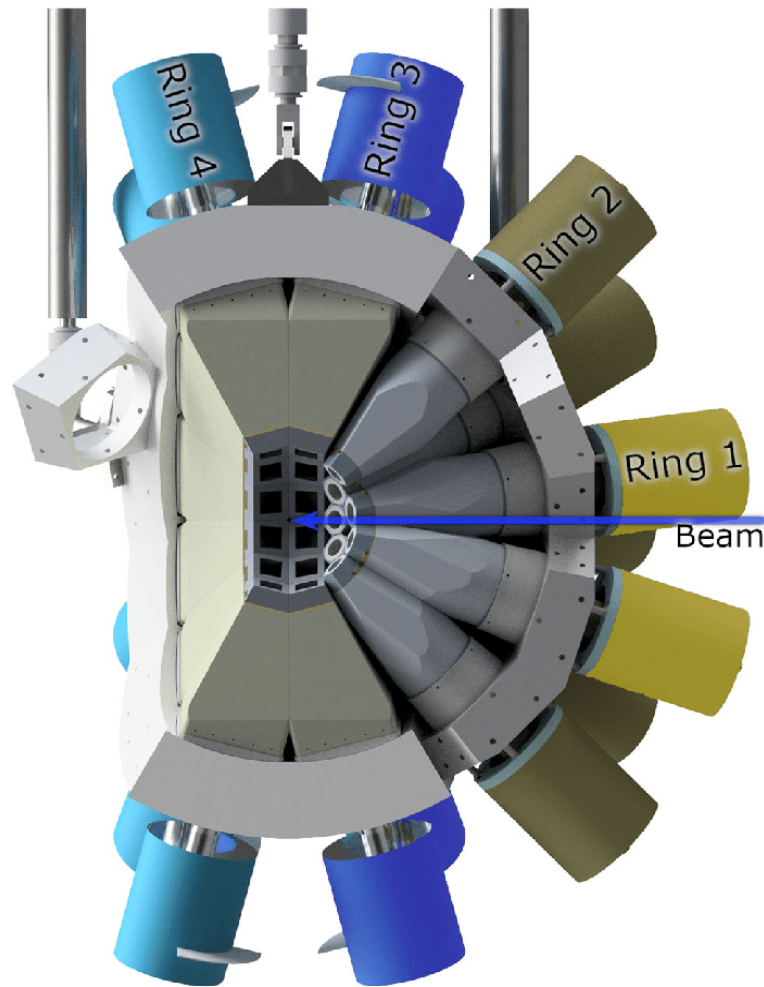
Figure 4.1: Side profile of the JUROGAM3 germanium detector array. The heavy-ion beam from the K130 cyclotron is depicted, passing from right to left through the various detector rings that are labelled [32].

4.2 MARA Recoil Separator

As it becomes increasingly difficult to study lighter and medium-mass ($A < 150$) nuclei with a gas-filled separator such as RITU, MARA was the recoil separator of choice for this experiment. For this particular work, in order to enable the selection of specific nuclei utilising mass-to-charge separation, it is required to use a near-symmetric fusion reaction (i.e. the masses of the projectile and target nuclei are comparable). A further feature of MARA in relation to this area is the improved beam suppression for such reactions. The high mass-resolving power of MARA and its capability of separating the fusion products based on their A/q ratios, are also desirable features in this instance due to the small cross-sections that result in nuclei far from stability. A full schematic and photographic depiction of MARA is shown in Fig. 4.2 and Fig. 4.3, respectively, both showing the quadrupole triplet, electrostatic deflector and magnetic dipole. The quadrupole triplet allows for the flexible transformation of the particle trajectories from the target area to the entrance of the detector. As shown in Fig. 4.4, there is point-to-parallel focus from the target to the electrostatic deflector, and point-to-point focus from the target to the focal plane. Following on from the quadrupole triplet, there is an adjustable aperture on each of the x and y directions.
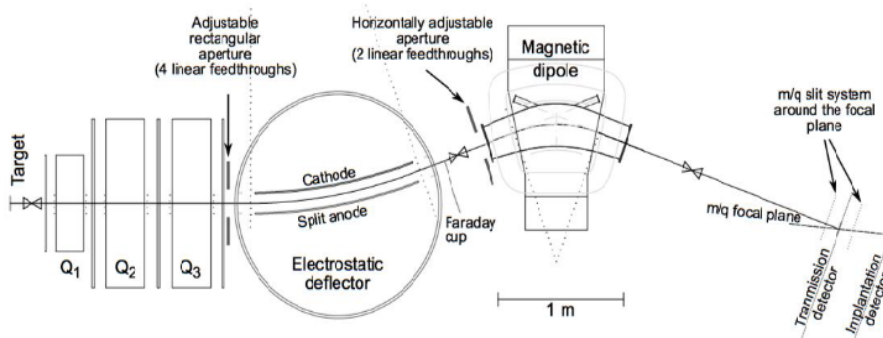
Figure 4.2: Schematic diagram depicting MARA, showing the positions of the quadrupole triplet, electrostatic deflector and the magnetic dipole from left to right [37].
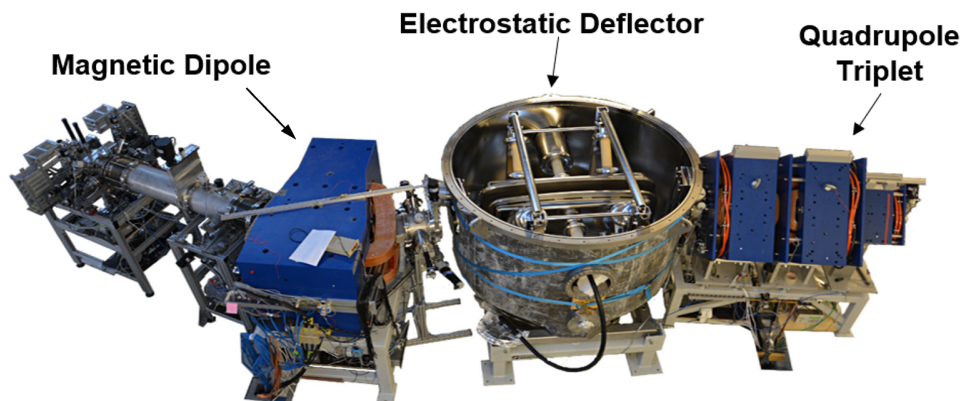
Figure 4.3: The full setup of MARA, showing the positions of the quadrupole triplet, electrostatic deflector and the magnetic dipole from right to left [38].

Upon passing to the electrostatic deflector (with beam separation of ±230kV and bending radius of ~ 4 m), the use of an electric field applied to the transverse of the path of the particles, separates the primary beam and the products (according to the energy per charge). The magnetic dipole (with a field strength of ~ 1 T and a ~ 1 m bending radius) consists of inclined and rounded effective field boundaries, as well as surface coils that are adjustable in order to change the focal plane position.

4.3 Focal Plane Setup

Whilst MARA is able to separate fusion products based on their A/q ratios, it is unable to separate overlapping isobars or fusion-evaporation reaction channels. Since this causes A/q ambiguity, further mass selectivity is desired and this can be achieved using the focal-plane set up (Fig. 4.5), inclusive of a multiwire proportional counter (MWPC), BB20 DSSD, box detector and punch through detector.
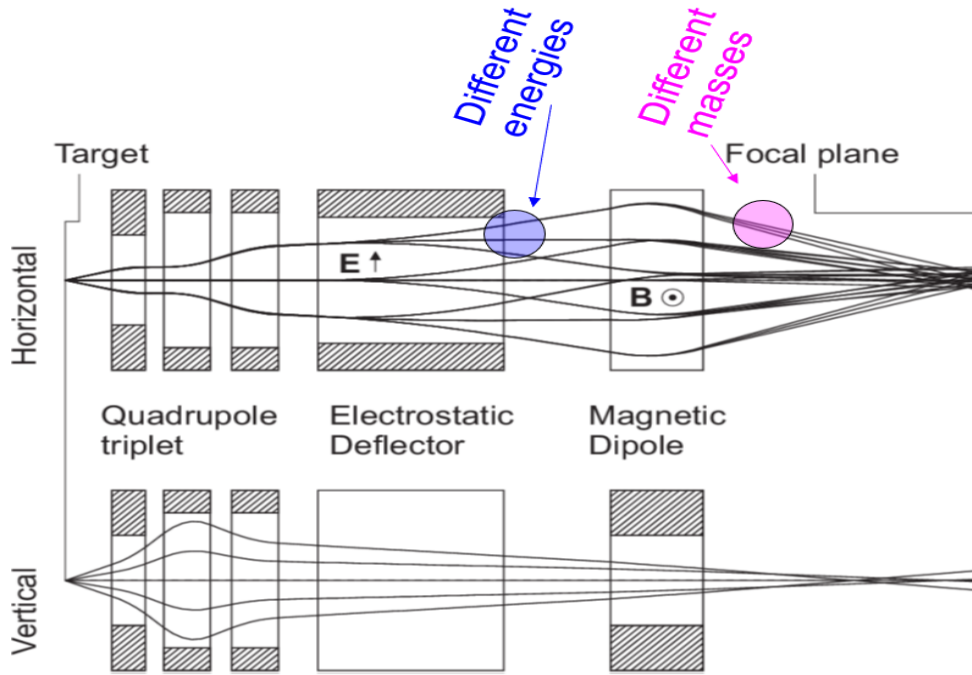
Figure 4.4: Side view schematic of MARA [35].
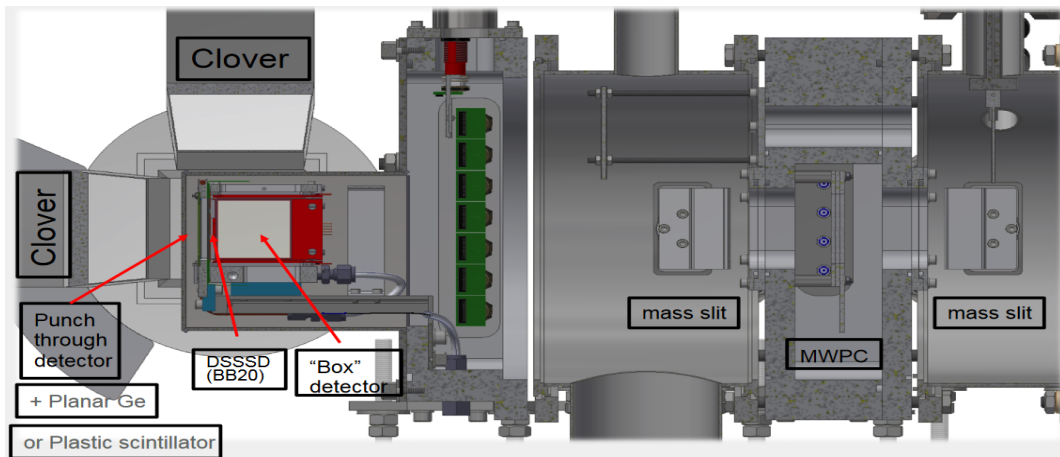
Figure 4.5: Diagram showing the focal plane setup after MARA.

4.3.1 Multi-Wire Proportional Counter (MWPC)

The role of the MWPC is to detect and give positional information on the trajectory of the charged particles. It includes an array of wires (anode) running through an isobutane gas-filled chamber with conductive walls (cathode). There are two layers of tungsten wires that are situated in the x and y planes (horizontal and vertical). The primary role of the MWPC is to distinguish between the recoiling nuclei prior to implantation in the DSSD, and it is these wires that are used to

provide position-sensitive information on the moving recoils. As shown in Fig. 4.4, the mass dispersion only occurs along the horizontal axis, thus the measured A/q ratio is only dependent on the MWPC-x coordinate. Fig. 4.6 displays a 2-D spectrum of the MWPC-x coordinate against γ-ray energy for all the recoils measured at the focal plane, highlighting the clusters of recoils corresponding to the different masses. Viewing the x and y projections of this spectrum yields 1-D spectra corresponding to the γ-ray energies and MWPC-x coordinates respectively. Figure 4.7 shows the raw spectrum of counts against MWPC-x coordinates for all recoils detected in JUROGAM3. In order to demonstrate the mass separating capabilities of MARA, Fig. 4.8 shows spectra of counts against MWPC-x coordinate for the recoils detected in JUROGAM3 when gating on known γ-ray energies corresponding to nuclei of various masses, showing the shift of the various charge states collected. When a high-energy ion beam interacts with the target material in an experiment, the ions that are produced may have lost or gained electrons during the interaction, leading to various different charge states. When these ions are detected, it may not be possible to determine which charge state they are in based on the detector's response alone. This uncertainty in the charge state of the ions gives rise to 'charge state ambiguity', meaning that in this case the A/q ratio is the same for nuclei with a mass difference of four. This mass difference can be attributed to the presence of multiple charge states of the recoils in the separator.

Mass Selectivity

To further increase the mass selectivity, it is desirable to create mass gates, and this is achieved by creating a 2-D matrix of the MWPC-x coordinate against Δx. The quantity Δx arises from the drift between the MWPC-x coordinate and the DSSD-x coordinate. The result of such mass gating further increases the selectivity achieved by MARA and has been used to show the measured spectra throughout the analysis in Chapter 5 of this work.
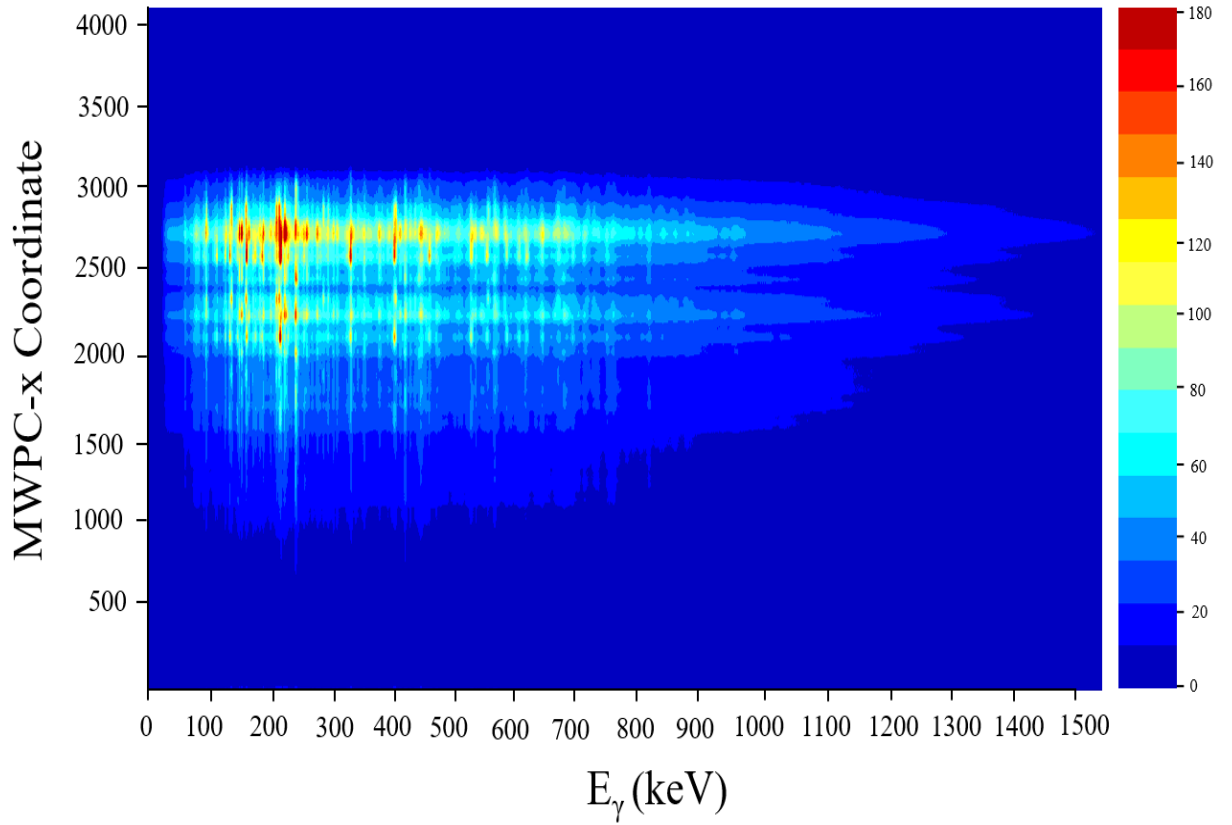
Figure 4.6: MWPC-x coordinate against γ-ray energy for all recoils detected at the focal plane.
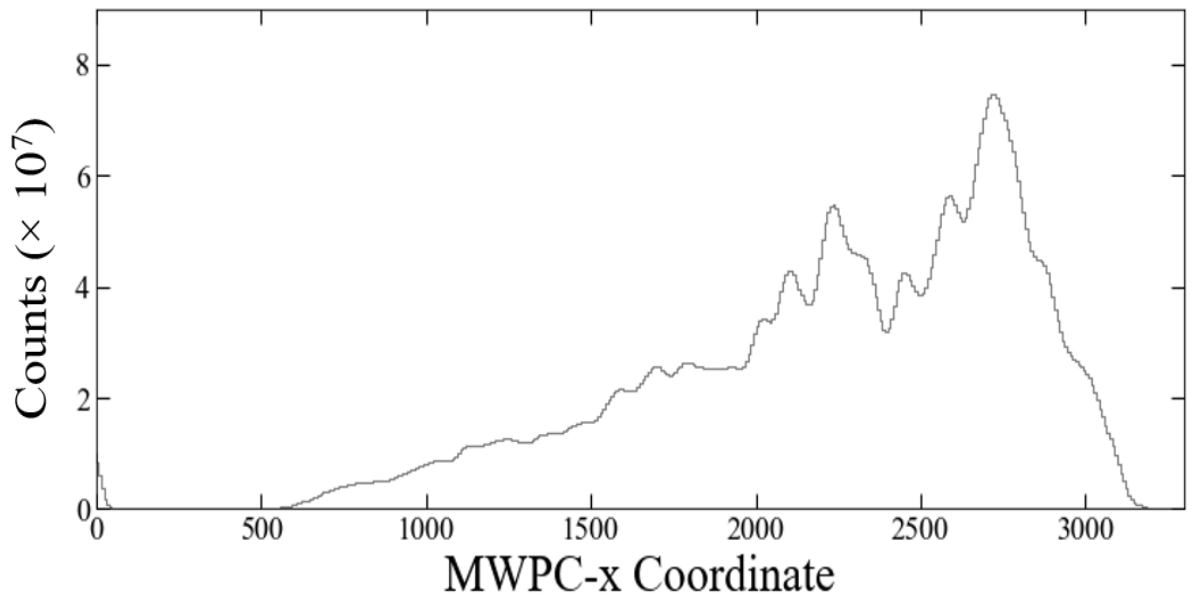
Figure 4.7: Raw spectrum to show counts against MWPC-x coordinate for all recoils detected in JUROGAM3.
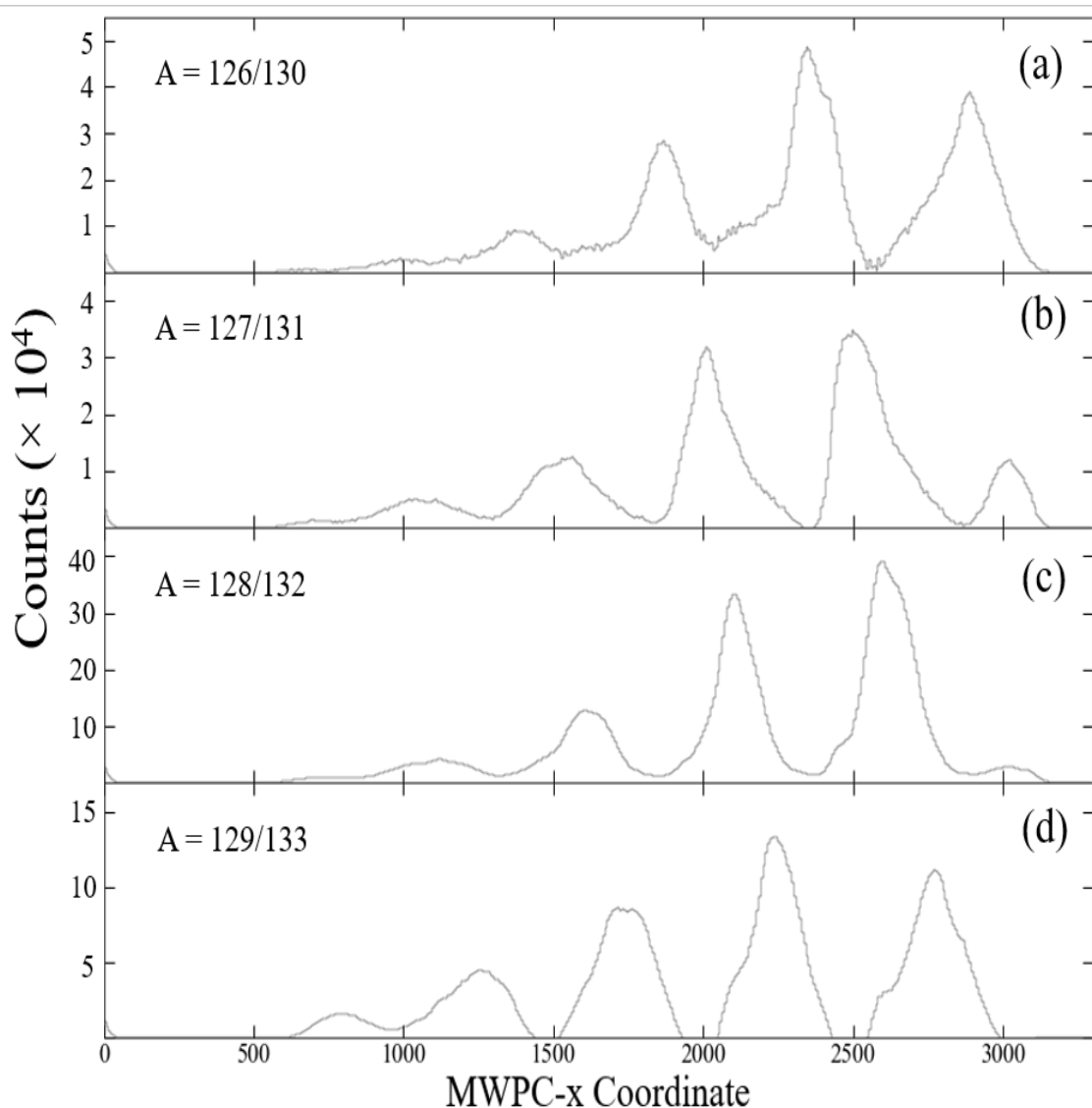
Figure 4.8: Spectra to show counts against MWPC-x coordinate for recoils detected in JUROGAM3 corresponding to various masses, to demonstrate the mass separation capabilities of MARA based on A/q: (a) $A = 126/130$ (in delayed coincidence with the $E_\gamma = 454$ keV in ^{130}Nd), (b) $A = 127/131$ (in delayed coincidence with the $E_\gamma = 273$ keV in ^{131}Pm), (c) $A = 128/132$ (in delayed coincidence with the $E_\gamma = 213$ keV in ^{132}Nd), (d) $A = 129/133$ (in delayed coincidence with the $E_\gamma = 416$ keV in ^{129}Pr).

4.3.2 Double-Sided Silicon Strip Detector (DSSD)

Beyond the MWPC, the recoiling reaction products are implanted into the BB20 DSSD [39]. For this experiment, the thickness of the DSSD used was 300 μm. In total, there are 192 strips in the x-direction and 72 strips in the y-direction with

a strip width of 0.67 mm. It is the DSSD (area of 128×48 mm^2) that identifies where ions are implanted, whilst measuring their energies, as well as the energies of subsequently emitted particles.

4.3.3 Further Focal Plane Detectors

The 'box detector' is a silicon detector that measures the energies of any particles that have escaped, allowing their energies to be measured and counted back again into the events that have been recorded in the implantation detector described above. No implantations occur in the 'punch through detector' and particles with low stopping power will pass straight through. Following this there is an array of Ge detectors comprising four clovers as well as a GREAT clover detector (consisting of four crystals each with fourfold segmentation [40] to measure the energies of higher energy γ rays. There were no planar detectors in use during this experiment.

4.4 Data Acquisition

4.4.1 Correlation Methods

The goal of the data acquisition system is to allow for the reconstruction of time correlations between the signals that are registered in different detectors throughout the experimental setup. Information on the specific nuclear species produced, is obtained from the signature observed from characteristic decay products. Correlation of this information with the recoils associated with a given decay, allows the γ rays of interest to be extracted.

The stages contributing towards the triggering include: the radiation at the target position, recoiling nuclei that emerge from MARA in to the focal plane setup, and then decay measurements from the nuclei that are implanted into the focal plane detectors. Should a signal from a detector lie within the trigger width of the DSSD signal, these two signals are said to be in *coincidence* and collectively defined as an event.

Figure 4.9 shows both the full raw γ-ray spectrum obtained using JUROGAM3,
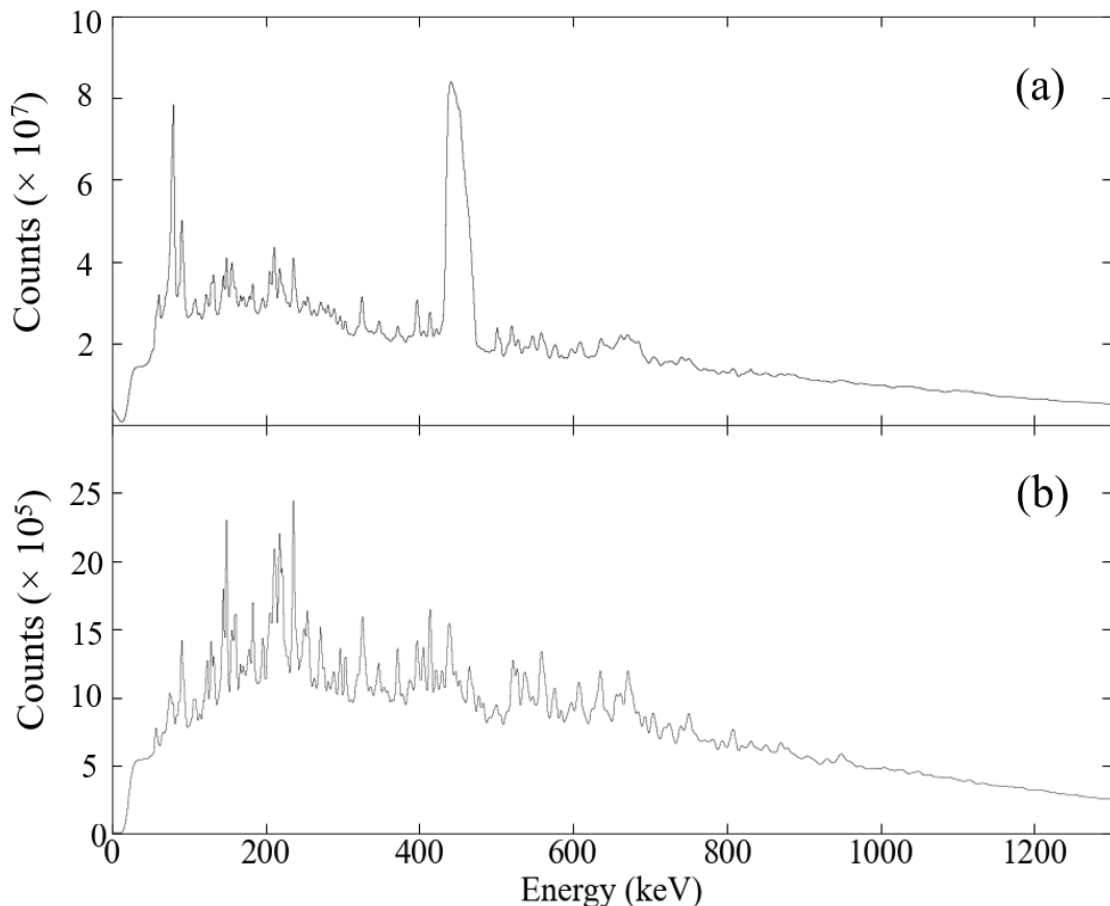
Figure 4.9: Gamma-ray spectra obtained with the JUROGAM3 spectrometer array. (a) shows the JUROGAM3 γ-ray total energy spectrum. (b) shows the γ rays in delayed coincidence with mass 129 or mass 132 recoils seen at the focal plane.

as well as the γ rays in delayed coincidence with mass 129 or mass 131 recoils that are implanted in the DSSD at the focal plane. This allows for the identification of the prompt γ rays observed and to confirm this with known structures for the nuclei in this region. Fig. 4.10 shows both the full raw γ-ray spectrum obtained from the detector setup at the focal plane of MARA, as well as the γ rays detected specifically with a mass of 129 or mass 132. As seen in Fig. 4.10, this significantly changes the spectrum observed and allows for the identification of specific γ-ray energies that can then be selected using the recoil-isomer tagging technique and correlated back to the prompt γ rays seen with JUROGAM3.
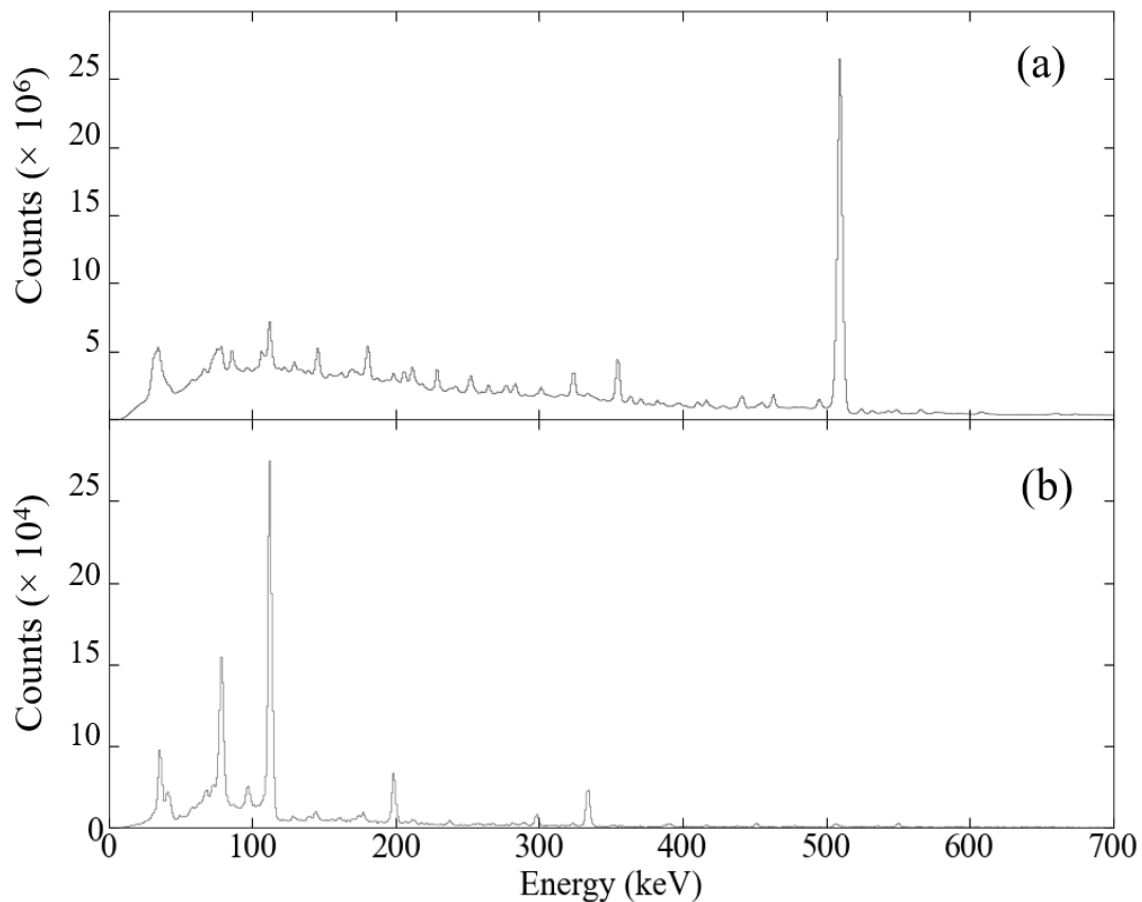
Figure 4.10: Gamma-ray spectra obtained from the focal plane of MARA. (a) shows the total MARA focal plane γ-ray energy spectrum. (b) shows the γ rays of the recoils detected at the focal plane of MARA with mass 129 or mass 132.

4.4.2 Total Data Readout

All acquired detector signals are then passed to the triggerless data acquisition system [41] that utilises a data collection method known as 'Total Data Readout' (TDR). This TDR concept was developed in order to overcome the common dead-time limitations present in past experiments, and allows for data acquisition from the target position and focal plane with measured dead-time data losses. This triggerless data acquisition system allows all events to be timestamped with a precision of 10 ns (with the distribution and synchronisation of a 100 MHz clock).

Event parsing (i.e. the re-construction of events) is then carried out by the GRAIN (Gamma-Ray Angular Intensity Correlations from Nuclear Reactions) software [42] using a Java sort code that is generated by the user.

4.4.3 Detector Calibrations and Data Corrections

JUROGAM3 Energy Calibrations

Prior to data analysis being carried out, it is necessary to perform a calibration of all the detectors. Outputs that are detected as an electrical signal are proportional to the energy deposited. However, without calibration using sources of known radiation, it is unknown to which energies these signals correspond to. In order to assign accurate energies, the germanium detectors of the JUROGAM3 array are calibrated using a stationary source containing ^{152}Eu and ^{133}Ba that is placed at the centre of the array. The focal-plane germanium detectors of MARA are calibrated externally, also using a mixed EuBa source. The source emits γ radiation over a range of energies from 80 keV to 1408 keV, and for the calibration, several peaks are chosen across this range and plotted as a function of the channel number. First, it was necessary to obtain calibration spectra from each of the individual detector outputs, then perform fits to obtain the centroids and intensities of the γ-ray peaks. It is the centroid of the peak that will provide information correlating to the energy of the γ rays, and the area underneath the photopeaks that will give information about the number of γ rays emitted, i.e. the intensities. This information was extracted using Gaussian fits, then a comparison of peak centroids is made with the known peak energies for the EuBa source. Since the relationship between the true energy and channel number is not linear, the relationship may be expressed by the following quadratic equation

$$E = Ax^2 + Bx + C, \tag{4.1}$$

where E is the photopeak energy, x is the channel number, and A, B and C correspond to the measured gain matching coefficients.

Efficiency Calibrations

In order to obtain accurate measurements of the absolute and relative intensities of the γ rays, it is necessary to determine the efficiencies of the JUROGAM3 detectors at various energies. As with the energy calibrations, the γ-ray spectra for each of the

detectors were obtained following the placement of the stationary source containing ^{152}Eu and ^{133}Ba at the centre of the detector array. The efficiency of any detector, ε, can be described by the ratio of the total number of particles detected (i.e. the area of the peak), to the expected number of particles emitted by the source. This relationship is shown by

$$\varepsilon_{abs} = \frac{N}{AIt}, \tag{4.2}$$

where ε_{abs} is the absolute efficiency of the array, A is the activity of the standard source (certified on 1st April 2003 to be 4.01 kBq for the Eu and 4.24 kBq for the Ba), I is the branching ratio of the transition and t is the live collection time. The variation of the ratio of the measured and reference intensities were then fitted (Fig. 4.11) using the polynomial function adapted from Ref. [43] and shown by

$$\varepsilon(E) = \frac{1}{E}[A + Bln(E) + Cln(E)^2 + Dln(E)^3 + Eln(E)^4], \tag{4.3}$$

where $\varepsilon(E)$ is the relative efficiency at the given energy in keV, and the parameters A, B, C, D and E are the fitted parameters of the function. It can be seen from Fig. 4.11 that the JUROGAM3 spectrometer array's peak efficiency is at $\sim$200 keV.

Doppler Shift Corrections

Since the recoiling compound nucleus is travelling extremely fast, the γ radiation emitted by it will be subject to a Doppler shift that is dependent on the velocity of the recoil itself. As a result of this, the γ-ray energy that will be measured in each of the rings of JUROGAM3 will vary from the 'true' γ-ray energy.

This relationship may be shown by

$$E = E_0 \left(1 + \frac{v}{c}cos(\theta)\right), \tag{4.4}$$

where E is the shifted γ-ray energy, E_0 is the true γ-ray energy, $\frac{v}{c}$ is the velocity of the recoils as a fraction of the speed of light, and θ is the angle of the detector relative to the beam direction.
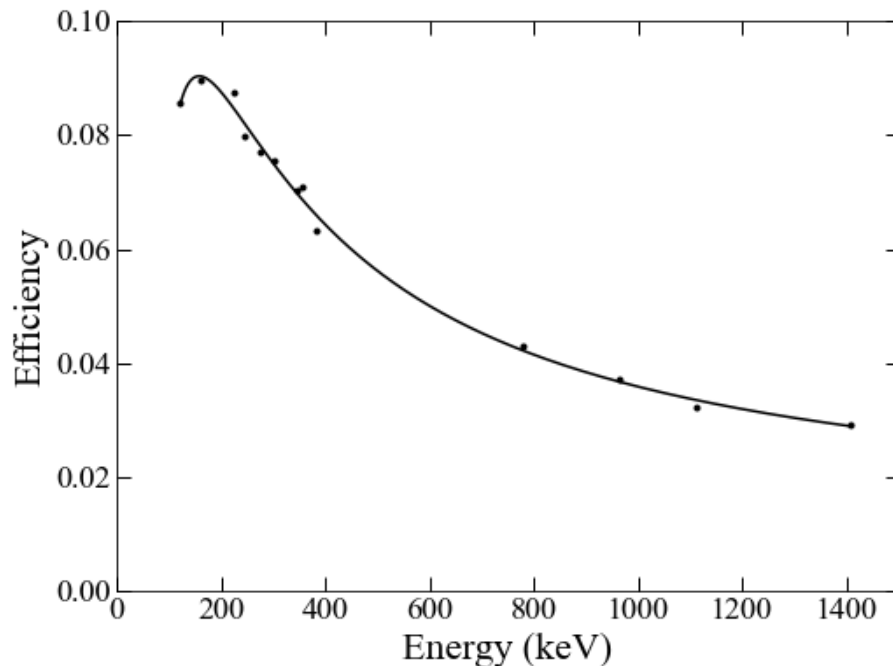
Figure 4.11: Measured efficiency as a function of energy for the JUROGAM3 array during the calibration runs in JM06. Fit parameters as given in Equation 4.3 are, A:97.91, B:$-$ 129.46, C:46.34, D:$-$ 6.33 and E:0.31.

Since the rings of JUROGAM3 have well-defined angles (θ), it is possible to measure the recoil velocity, $\frac{v}{c}$ in order to correct the shifted γ-ray energies. By measuring the centroid of a chosen in-beam photopeak at several chosen ring angles, it is possible to obtain a plot of the measured energy as a function of $\cos\theta$ (Fig. 4.12). The resulting gradient from this plot is then $E_0\frac{v}{c}$ (where $\frac{v}{c}$ was measured to be 0.05) and the intercept is E_0 as taken from Equation 4.4. By the division of the gradient by the intercept and calculation of the associated uncertainty, the Doppler-correction factor β can then be obtained and is found in this instance to be 0.051 $\pm$ 0.001. Fig. 4.13 (a)-(d) shows the Doppler-shifted spectra obtained from the JUROGAM3 detectors at 75.5°, 104.5°, 133.57°and 157.6°, respectively. It can be seen from the two most extreme angles in these spectra that at the forward angle (i.e. 75.5°) the detectors are Doppler shifted to a higher energy, and at the backward angle (i.e. 157.6°) the detectors are shifted to a lower energy. To ensure the measurement of the true γ-ray energies, the Doppler-correction β is applied so that peaks detected at the various polar angles in JUROGAM3 are aligned. The

value of $\dfrac{v}{c}$ calculated here can also be used to determine the time of flight through

MARA – since the flight path of MARA is approximately 6.9 m, and $\dfrac{v}{c} \approx 0.05$, the time of flight can be calculated to be around 490 ns.
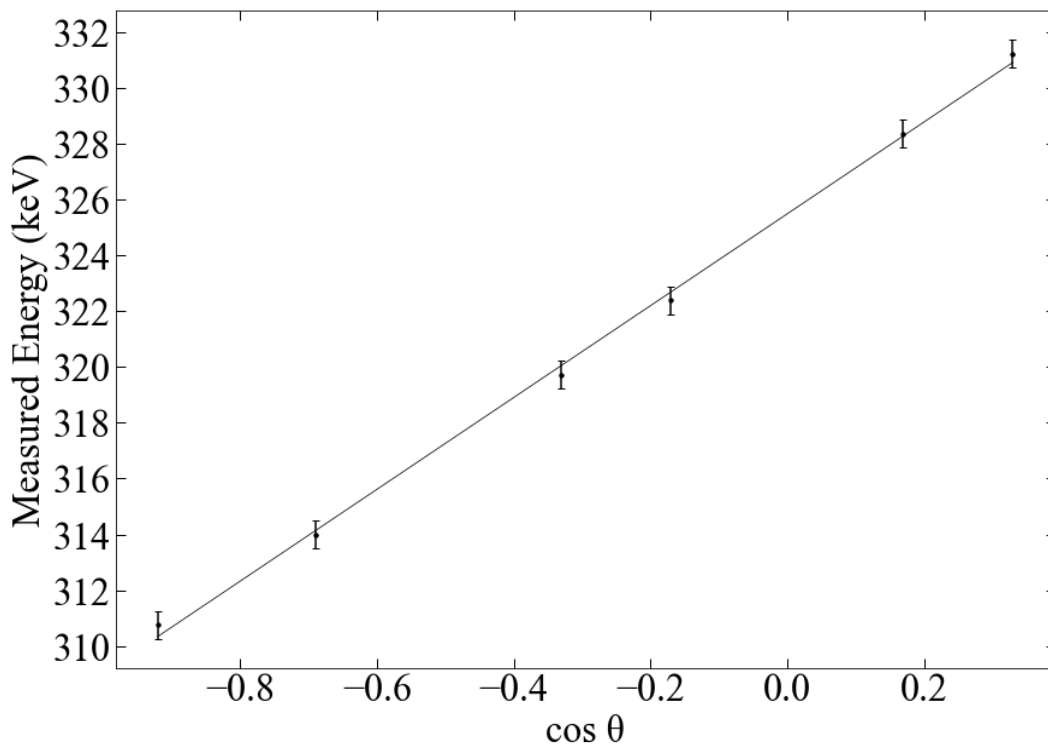
Figure 4.12: Measured energy (keV) from a chosen in-beam photopeak centroid position as a function of θ.

Doppler Broadening

The recoil velocity as described above also affects the width of the emitted γ rays that are observed. It is the finite opening angle of the detectors with respect to the beam axis that results in the Doppler broadening of energy signals, since a range of Doppler shifted energies may be detected in the same detector. This broadening is at its maximum in detectors at $\theta = 90°$ to the beam axis.
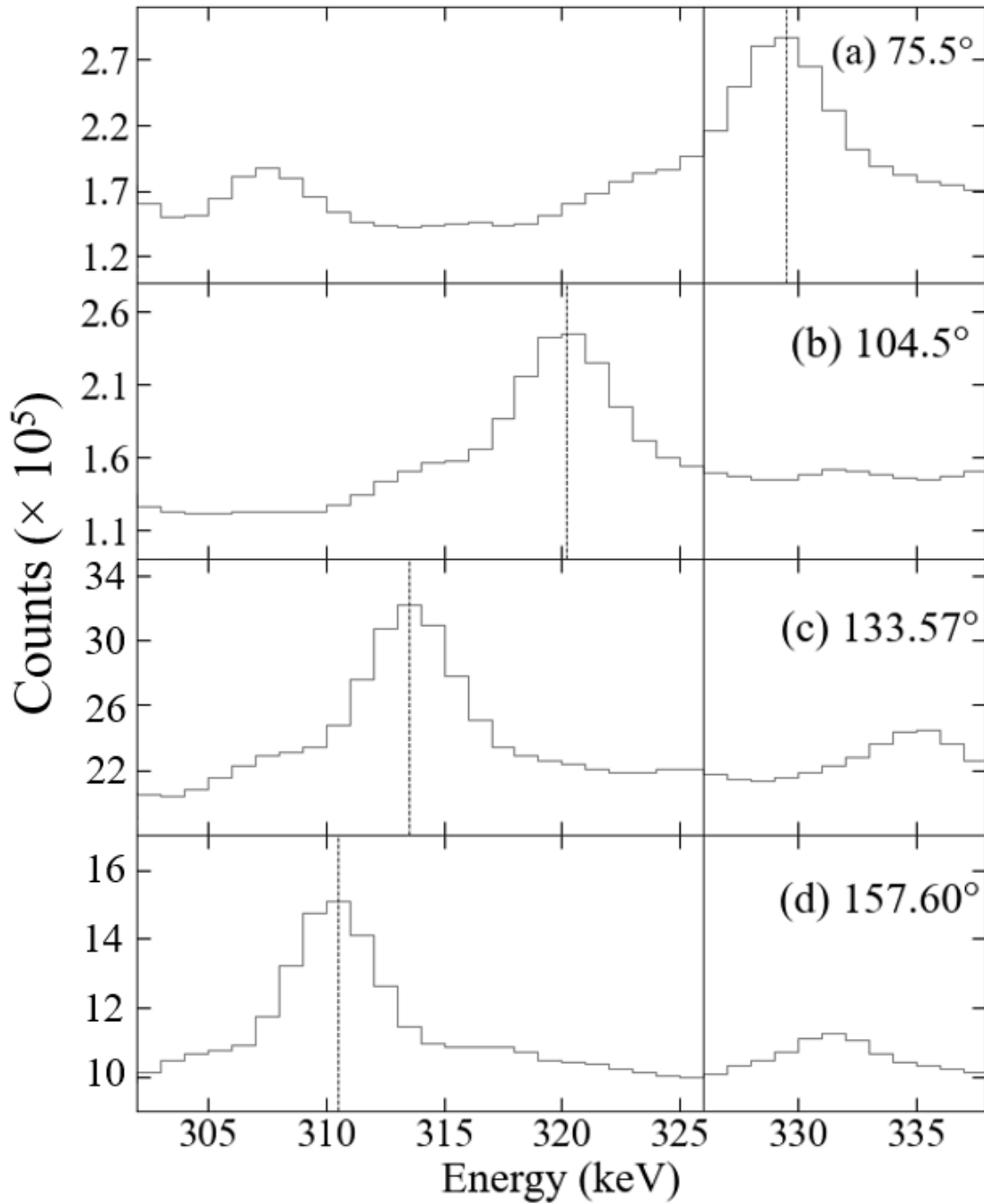
Figure 4.13: Doppler-shifted γ-ray spectra obtained from several angles in the JU-ROGAM3 detectors at (a) 75.5 °, (b) 104.5 °, (c) 133.57 °and (d) 157.6 °, all demonstrated by measuring a chosen in-beam photopeak – with a 'true' energy of 326 keV shown by the solid line.

Add-back

A further 'correction' that was incorporated into the γ-ray reconstruction was the process of add-back. This was applied to the signals from the segmented Clover detectors of JUROGAM3. It is possible for γ rays to Compton scatter from one crystal into adjacent crystals, thus it is necessary to sum the energy signals from adjacent crystals to the give the correct γ-ray energy. This summing was based upon two signals being detected within a timeframe of 10 ns, therefore they may be assumed to correspond to a single event.

4.5   Data Analysis

4.5.1   Gamma Coincidence Measurements

The number of γ rays that are produced in a single event often varies depending on the type of reaction – generally for the rare-earth nuclei produced in fusion-evaporation reactions, the γ-ray multiplicity is around 25 to 30 [44]. The 'fold' of the event may then be defined as the number of γ rays that are actually detected and recorded as a single event, and this is dependent on the efficiency of the detector. For example, a three-fold coincidence event, is a case in which three γ rays are detected in three different detectors and recorded as a single event.

In order to visualise coincidence data, it is preferable to display data produced from such high statistics experiments into spectra of a fixed fold known as a correlation matrix. In the case of this particular data analysis, data were unpacked into a 3-D spectrum known as a γ-γ-γ correlation matrix (also known as a cube). Spectra of 1-D can then be generated from the created cubes – gates may be set on two of the axes, and the projections on the third axis are energies in coincidence with those set gates. The RadWare [45] software package is used for further coincidence analysis, and enables the construction of level schemes from high-fold coincidence spectra.

4.5.2 Angular Intensity Ratios

In order to obtain a greater understanding of nuclear structure, nuclear states are generally characterised by several quantities including (but not limited to) energy, spin and parity. It is desirable to compare experimental observations of such properties of the excited states with theoretical calculations. To assign values of spin and parity to the energy levels observed, and to bring meaning to the level schemes, angular-correlation analysis has become an invaluable tool in doing so. The angular momenta of nuclei produced with high-excitation energies and spins, are aligned perpendicular to the beam axis ($\overrightarrow{L} = \overrightarrow{r} \times \overrightarrow{p}$), thus it is possible to deduce the angular momentum carried by the emitted γ rays. The electromagnetic multipoles of the emitted γ rays in a cascade can be determined from the measured angular distribution, W (θ), given by

$$W(\theta) = A_0 + Q_2 A_2 P_2(\cos\theta) + Q_{d4} A_4 P_4(\cos\theta), \qquad (4.5)$$

where Q_k are geometrical attenuation coefficients accounting for the finite size of the detectors, $P_k(\cos\theta)$ are Legendre polynomials, and A_k are coefficients that are compared to theoretical values for various types of radiation. The angle, θ is defined as the angle between the incident γ ray and the beam axis.

The concept of this analysis is that the direction of emission of the second γ ray in a cascade, is measured with respect to the first. A large spectrometer such as JUROGAM3 is beneficial to obtaining such measurements directly due to its geometry surrounding the target position. One dimensional spectra can be produced for the coincidence transitions at each of the ring angles in JUROGAM3 relative to the beam direction.

In this instance, as shown in Fig. 4.1, there are four rings, therefore there are four possible values of θ. Since there are statistical limitations with the number of counts measured at each angle, it is preferable to measure angular intensity ratios in place of a full angular-correlation analysis. This method is known as directional correlation analysis (DCO) [46].

In this method, a 2-D matrix is created consisting of the events recorded at extreme angles (Phase 1 detectors) against the events recorded at a normal angle

(Clover detectors) with respect to the beam direction. In addition to this, a further gating condition of a single γ-ray energy from any detector is incorporated. This serves to increase selectivity and enhance the transitions of interest, greatly reducing any background from other reaction products. By allowing this gating transition from any detector, there should be minimal effect on the angular correlations of the other two γ rays, given the isotropic distribution of the JUROGAM3 detectors [47]. The principle of DCO involves taking a ratio of the intensity of a γ ray at the extreme angles and the normal angles, shown by

$$R_{DCO} = \frac{I_\gamma(\text{measured Phase 1, gated clover})}{I_\gamma(\text{measured clover, gated Phase 1})} \tag{4.6}$$

or

$$R_{DCO} = \frac{I_\gamma[158°(90°)]}{I_\gamma[90°(158°)]}, \tag{4.7}$$

where the extreme Phase 1 detector angle is taken from Ring 1 (Figure 4.1) at 157.6°, and the normal Clover detector angle is a summation of Rings 4 and 5 at 90°.

Since a ratio of γ coincidences between the Phase 1 and Clover detectors is produced, any relative differences in detector efficiencies are cancelled out and accounted for.

Chapter 5

Rotational Structures in the Highly Deformed ^{129}Pr

5.1 Motivation and Previous Work

The mass region, $A \approx 130$ is of great interest as it a region of particularly high nuclear deformation. The investigation of the rotational structures of nuclei in this region has enabled further investigations into the shape-driving effects of valence and intruder orbitals, as well as being able to observe how the nuclear shape changes from triaxial to prolate shapes at higher spins. With the Fermi surface of both protons and neutrons being in the same subshell, it is well-known that the deformed structures are built on a configuration involving the $h_{11/2}$ shell. The occupation of valence protons in the low-Ω orbitals and valence neutrons in the high-Ω orbitals, is a key factor in determining the shape-driving effects that can occur. The occupation of protons in a low-Ω orbital drives the nucleus to prolate deformations, whilst the occupation of neutrons in a high-Ω orbital drives the nucleus to adopt a more oblate shape. As these nuclei become more neutron deficient towards the proton drip line, the Fermi surface of both protons and neutrons are expected to be at similar levels. Thus, an increase in deformation is to be expected as a result of the increasing possibility of proton-neutron interactions or the occupation of low-Ω orbitals.

The negative-parity $h_{11/2}$ structure was previously identified by Weng et al. [48] up to a spin of $43/2^-$ and extended up to a spin of $51/2^-$ in the work carried out in by Smith et al. [49] with an experiment performed at Lawrence Berkeley National

Laboratory using the Microball CsI(Tl) detector array [50]. A rotational strongly couple band associated with the $\pi g_{9/2}$ "extruder" orbital was also established. Work carried out by Gizon et al. [51] has also confirmed that the β^+ decays from ^{129}Nd established the ground state spin of ^{129}Pr to be at a spin of $3/2^+$. This chapter presents the discovery of two previously unobserved sidebands that have been identified in this work (named as Band 2 and Band 3), as well as the extension of the known strongly coupled band that is associated with the $\pi g_{9/2}$ extruder orbital.

5.1.1   Pr Systematics

To look at how the deformation changes as a function of the neutron number, a systematic comparison of the lower spin states in the $h_{11/2}^-$ bands of several Pr isotopes is shown in Fig. 5.1. It can be seen that the spacing in these bands, of both the Pr and corresponding $A - 1$ even-even Ce isotopes, follow each other closely. This pattern is suggestive of the $h_{11/2}$ odd proton coupling to the associated even-even Ce core, thus being a rotationally aligned particle. It can also be observed that there is a decrease in energy level spacing with decreasing neutron number, which is indicative of an increase in deformation.

5.2   Experimental Details

Levels in the isotopes under investigation were populated using beams from the K130 cyclotron accelerator in the fusion-evaporation reaction $^{58}_{28}\text{Ni}(^{78}_{36}\text{Kr}, \alpha 3p)^{129}_{59}\text{Pr}$. The beam of ^{78}Kr ions bombarded a ^{58}Ni target of nominal thickness 0.75 mg/cm^2 at an energy of 365 MeV and a beam intensity of 3 pnA [32]. Following beam optimisation in order to produce the reference particle mass of $A = 129$, the data produced from this experiment provided data sets for the several nuclei via various evaporation-reaction channels, inclusive of ^{129}Pr discussed in this work. Prompt γ rays were detected by the JUROGAM3 spectrometer array at the target position, where the recoiling fusion-reaction products were then passed through MARA and separated from the unreacted beam based on their A/q ratios. For the first twelve
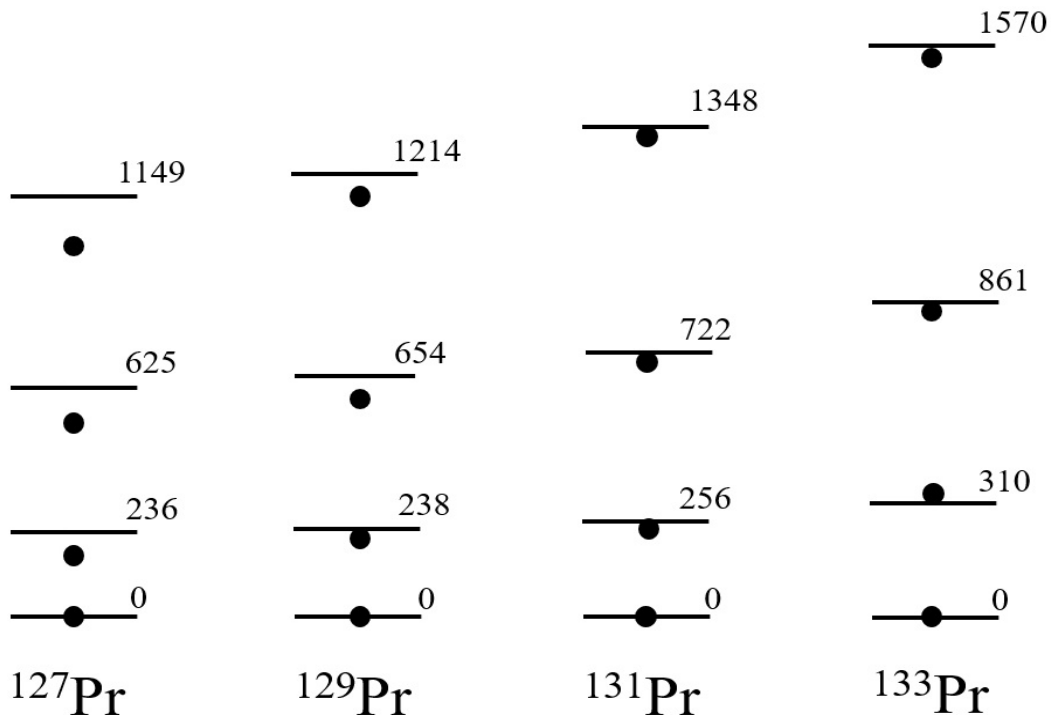
Figure 5.1: The systematics of the low spin parts of the $h_{11/2}$ bands in several Pr isotopes, ranging from ^{127}Pr to ^{131}Pr [52][49][53][54]. The lines represent the level spacing in the Pr isotopes (labelled with the energy level in keV), whilst the dots represent the level spacing in the $A-1$ even-even Ce cores [55][56][57][54]. The lowest energy levels of the $h_{11/2}$ structures have been set to zero to be used as a reference. Levels are labelled by their excitation energy in keV.

days of the run, the beam energy was set to $E_k = 390$ MeV in order to be optimised for maximal production of ^{131}Eu. For the remainder of the run, the beam energy was adjusted to $E_k = 394$ MeV in order to be optimised for the production of ^{129}Nd. After traversing the MWPC, the recoils were then implanted into the DSSD detector situated at the focal plane.

Since the transitions from various reactions are observed in the γ-ray spectra, it is necessary to first utilise the mass selectivity of MARA in order to identify specific nuclei. This removes or minimises the influence of contaminating transitions in the spectra. Previously published data may also be used as a guide in order to assist with this identification. Following the event parsing carried out in GRAIN and the unpacking of data into a cube format, the RadWare software was then used to carry out the triple-γ coincidence analysis. The analysis of the observed spectra by

gating on the specific γ-transition energies, enabled the construction of nuclear level schemes that form the basis of the results presented in this work.

5.3 Results

The experimental results will be discussed for each of the observed bands shown in the level scheme, and further analysis will be examined in the discussion section of this chapter. All spectra shown in this chapter are mass-gated in order to further increase selectivity.

5.3.1 Band 1

The present work has identified the previously known cascade of E2 transitions up to spin $55/2^-$ with an excitation of 1254 keV (Fig. 5.2), with no further transitions being confirmed from the current data. This band has been identified as the yrast band, and from the data in this work it is presently not possible to confirm links with the highly deformed structure of Band 4.
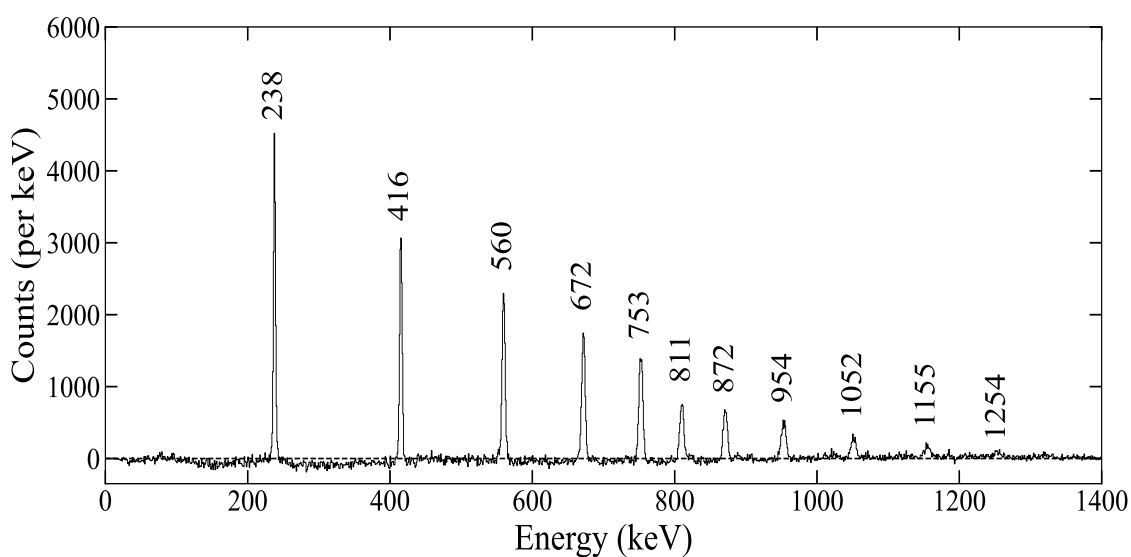
Figure 5.2: Spectrum of sum of double gates of gatelists to show Band 1 (x = 238 keV up to 753 keV, y = 811 keV up to 1254 keV).

5.3.2   Band 2

In this work, based upon the spectra that can be seen in Fig. 5.3, it has been concluded that this cascade of transitions does feed into Band 1 via two assigned transitions of 996 keV and 1118 keV. Plot (a) in Fig. 5.3 shows the resulting spectrum from creating a sum of double gatelist of 432 keV up to 891 keV, showing both the 996 keV and 1118 keV transitions. Plot (b) shows the sum of double gatelist from 492 keV up to 891 keV and the 996 keV linking transition, thus confirming that the 432 keV transition within this band is no longer visible. Plot (c) shows the sum of the doubles gatelist from 432 keV up to 891 keV, thus confirming that the 1118 keV linking transition is correct at linking Band 2 to Band 1 also.

5.3.3   Band 3

As with band 2, it can be seen that band 3 forms a rotational cascade of E2 transitions that links to band 1 via three linking transitions of 1066 keV, 1185 keV and 1297 keV. Figure 5.4 shows three spectra created to justify the positions of these linking transitions, with the sum of doubles gatelists alongside these transitions confirming Band 3 feeding into Band 1 at these points.

5.3.4   Band 4

Band 4 can be seen from the coincidence spectra as shown in Fig. 5.5 whereby a sum of doubles spectra has been created using a gatelist of the M1 transitions from 186 keV up to 374 keV. In this work, four new E2 transitions of 802 keV, 828 keV, 876 keV and 945 keV, and two new M1 transitions of 374 keV and 397 keV, have been identified and added to the level scheme shown in Fig. 5.6. Based upon the systematics of other odd Pr nuclei, this structure of enhanced deformation is presumed to be of positive parity, consisting of two rotational cascades of E2
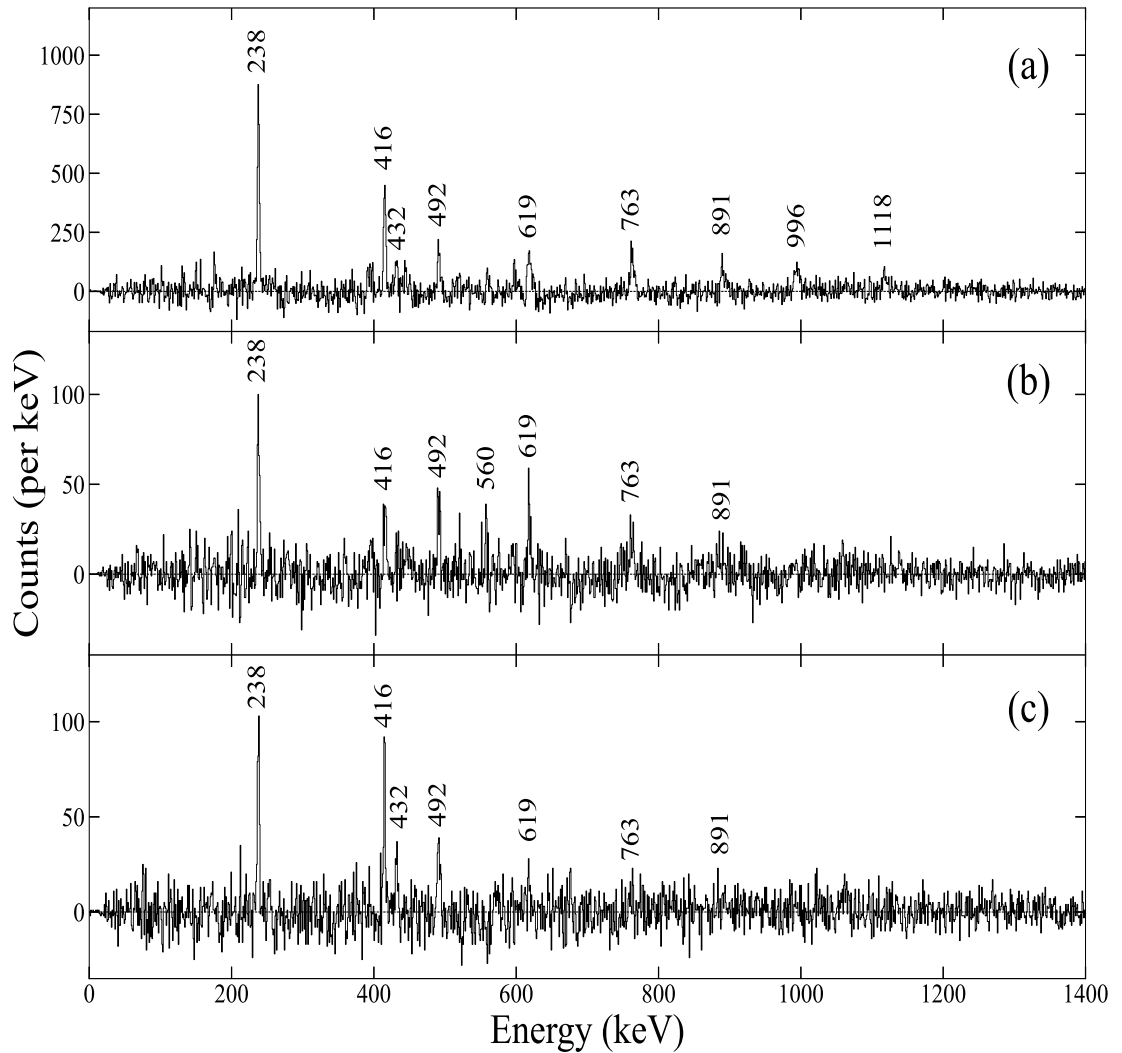
Figure 5.3: Spectra of gatelists and linking transitions to show Band 2. (a) is a sum of doubles gatelist of x = 432 keV up to 891 keV. (b) is a sum of doubles gatelist of x = 492 keV up to 891 keV and 996 keV. (c) is a sum of doubles gatelist of x = 432 keV up to 891 keV and 1118 keV.

transitions connected by a series of M1 transitions. At this point, it is not possible to confirm the position of this band relative to Band 1, due to the lack of data seen regarding any focal plane γ rays. Previous work carried out by Gizon et al. [51] has confirmed that the $9/2^+$ state at the bottom of this band sits at an excitation energy of 497.3 keV, and the lifetime has been measured as 60 ns. This accounts
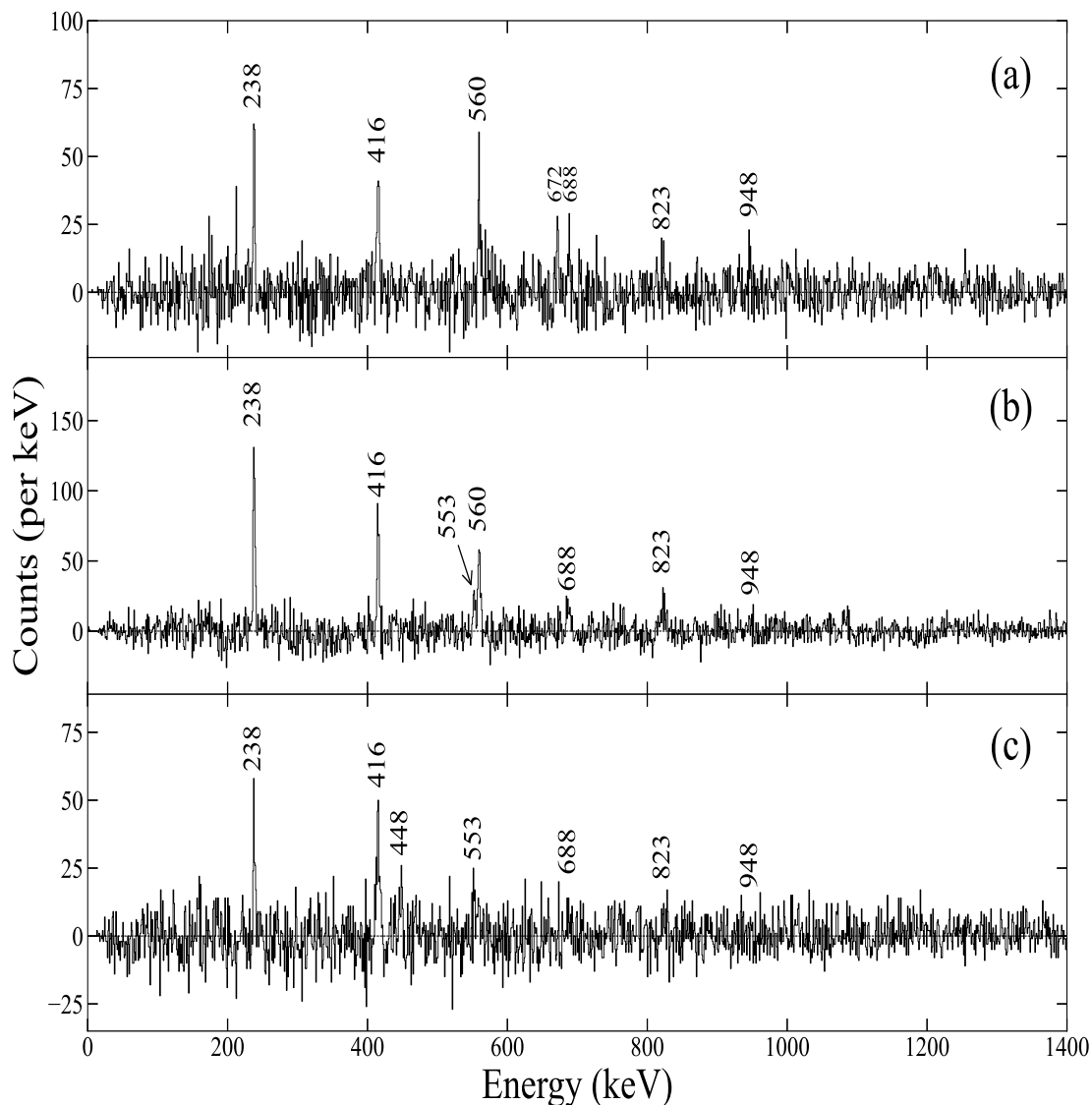
Figure 5.4: Spectra of gatelists and linking transitions to show Band 3. (a) is a sum of doubles gatelist of x = 688 keV up to 948 keV and 1066 keV. (b) is a sum of doubles gatelist of x = 553 keV up to 948 keV and 1185 keV. (c) is a sum of doubles gatelist of x = 448 keV up to 948 keV and 1297 keV.

for why the decay to the proposed ground state is not seen, due to its de-excitation in-flight between JUROGAM3 and the focal plane.

The level scheme for ^{129}Pr deduced in this work is shown in Fig. 5.6, and the
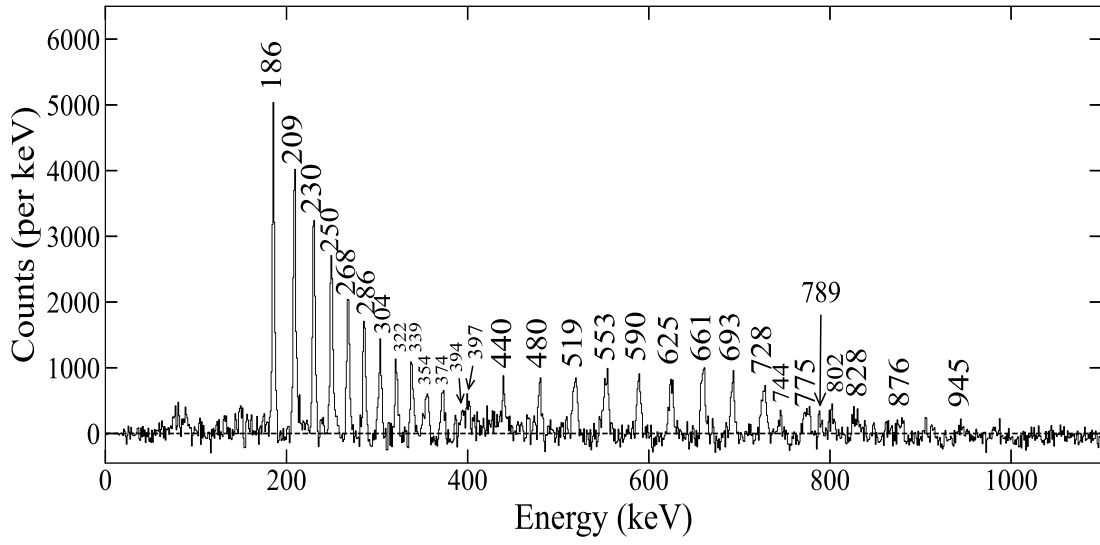
Figure 5.5: Spectra of a gatelist to show Band 4. This plot is a sum of doubles gatelist of the M1 transitions from 186 keV up to 374 keV.

measured properties of γ rays observed, and their associated quantities are recorded in Table 5.1.
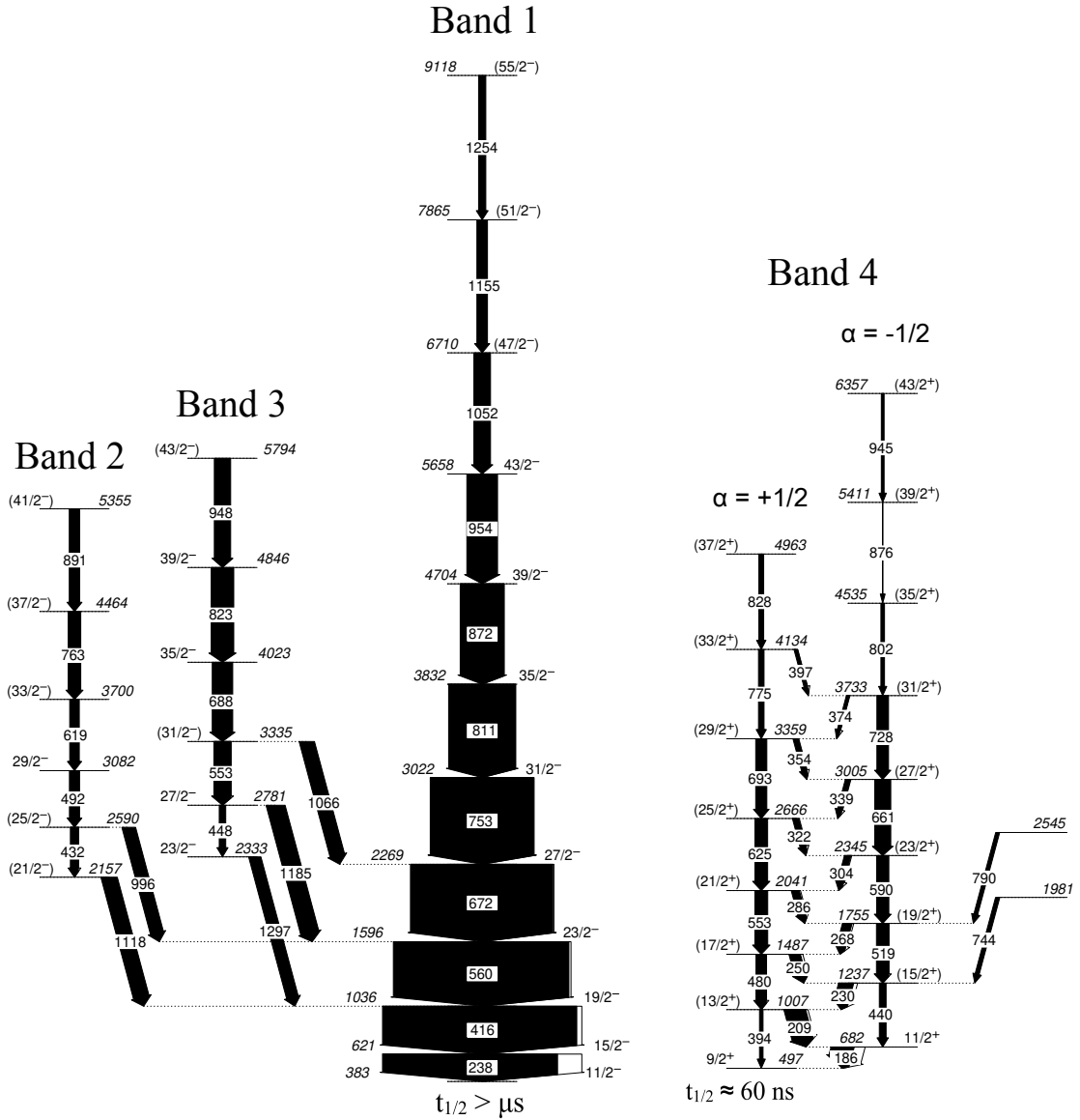
Figure 5.6: The level scheme deduced for ^{129}Pr. The $11/2^-$ state in band 1 sits at an excitation energy of 382.7 keV. The half-life, $t_{1/2}$ for the bandhead is currently unknown. The $9/2^+$ state in band 4 sits at an excitation energy of 497.3 keV based on work carried out in Ref. [51], with a half-life of $t_{1/2} \approx 60$ ns. Brackets on spins and parities indicate tentative assignments where there are a lack of DCO measurements. Widths of arrows correspond to relative intensities.

Table 5.1: List of γ rays and their measured properties for ^{129}Pr. Quantities in brackets denote a tentative assignment to its value.

E_γ (keV)	I$_\gamma$	$J_i^\pi \rightarrow J_f^\pi$	DCO	Multipolarity (λ L)	Band
Band 1					
238	100.0	$15/2^- \rightarrow 11/2^-$	0.88 ± 0.01	E2	1
416	94.7	$19/2^- \rightarrow 15/2^-$	0.96 ± 0.06	E2	1
560	84.4	$23/2^- \rightarrow 19/2^-$	0.68 ± 0.05	E2	1
672	71.2	$27/2^- \rightarrow 23/2^-$	1.04 ± 0.02	E2	1
753	64.6	$31/2^- \rightarrow 27/2^-$	0.99 ± 0.04	E2	1
811	35.2	$35/2^- \rightarrow 31/2^-$	0.82 ± 0.06	E2	1
872	33.5	$39/2^- \rightarrow 35/2^-$	1.11 ± 0.14	E2	1
954	25.5	$43/2^- \rightarrow 39/2^-$	0.91 ± 0.16	E2	1
1052	15.1	$(47/2^-) \rightarrow (43/2^-)$	-	(E2)	1
1155	-	$(51/2^-) \rightarrow (47/2^-)$	-	(E2)	1
1254	-	$(55/2^-) \rightarrow (51/2^-)$	-	(E2)	1
Band 2					
432	-	$(25/2^-) \rightarrow (21/2^-)$	-	(E2)	2
492	-	$29/2^- \rightarrow 25/2^-$	0.83 ± 0.20	E2	2
619	-	$(33/2^-) \rightarrow (29/2^-)$	-	(E2)	2
763	-	$(37/2^-) \rightarrow (33/2^-)$	-	(E2)	2
891	-	$(41/2^-) \rightarrow (37/2^-)$	-	(E2)	2
996	-	$(25/2^-) \rightarrow (23/2^-)$	-	(M1)	$2 \rightarrow 1$
1118	-	$(21/2^-) \rightarrow (19/2^-)$	-	(M1)	$2 \rightarrow 1$
Band 3					
448	-	$27/2^- \rightarrow 23/2^-$	0.99 ± 0.04	E2	3
553	-	$31/2^- \rightarrow 27/2^-$	0.82 ± 0.06	E2	3
688	-	$35/2^- \rightarrow 31/2^-$	1.08 ± 0.24	E2	3
823	-	$39/2^- \rightarrow 35/2^-$	1.20 ± 0.25	E2	3
948	-	$(43/2^-) \rightarrow (39/2^-)$	-	(E2)	3
1066	-	$(31/2^-) \rightarrow (27/2^-)$	-	(E2)	$3 \rightarrow 1$
1185	-	$(27/2^-) \rightarrow (23/2^-)$	0.98 ± 0.96	(E2)	$3 \rightarrow 1$
1297	-	$(23/2^-) \rightarrow (19/2^-)$	0.91 ± 0.35	(E2)	$3 \rightarrow 1$
Band 4					
186	100.0	$11/2^+ \rightarrow 9/2^+$	0.49 ± 0.07	M1	4
209	85.2	$(13/2^+) \rightarrow (11/2^+)$	-	(M1)	4
230	74.3	$(15/2^+) \rightarrow (13/2^+)$	-	(M1)	4
250	62.0	$(17/2^+) \rightarrow (15/2^+)$	-	(M1)	4

E_γ (keV)	I_γ	$J_i^\pi \to J_f^\pi$	DCO	Multipolarity (λ L)	Band
268	50.2	$(19/2^+) \to (17/2^+)$	-	(M1)	4
286	43.5	$(21/2^+) \to (19/2^+)$	-	(M1)	4
304	30.5	$(23/2^+) \to (21/2^+)$	-	(M1)	4
322	26.9	$(25/2^+) \to (23/2^+)$	-	(M1)	4
339	27.8	$(27/2^+) \to (25/2^+)$	-	(M1)	4
354	16.1	$(29/2^+) \to (27/2^+)$	-	(M1)	4
374	18.5	$(31/2^+) \to (29/2^+)$	-	(M1)	4
394	-	$(13/2^+) \to (9/2^+)$	-	(E2)	4
397	-	$(33/2^+) \to (31/2^+)$	-	(M1)	4
440	20.3	$(15/2^+) \to (11/2^+)$	-	(E2)	4
397	-	$(33/2^+) \to (31/2^+)$	-	(M1)	4
480	24.1	$17/2^+ \to 13/2^+$	0.89 ± 0.22	E2	4
519	28.1	$(19/2^+) \to (15/2^+)$	-	(E2)	4
553	28.7	$(21/2^+) \to (17/2^+)$	-	(E2)	4
590	31.1	$(23/2^+) \to (19/2^+)$	-	(E2)	4
625	30.0	$(25/2^+) \to (21/2^+)$	-	(E2)	4
661	39.8	$(27/2^+) \to (23/2^+)$	-	(E2)	4
693	34.3	$(29/2^+) \to (25/2^+)$	-	(E2)	4
728	-	$(31/2^+) \to (27/2^+)$	-	(E2)	4
744	-	-	-	-	4
789	-	-	-	-	4
775	-	$(33/2^+) \to (29/2^+)$	-	(E2)	4
802	-	$(35/2^+) \to (31/2^+)$	-	(E2)	4
828	-	$(37/2^+) \to (33/2^+)$	-	(E2)	4
876	-	$(39/2^+) \to (35/2^+)$	-	(E2)	4
945	-	$(43/2^+) \to (39/2^+)$	-	(E2)	4

5.4   Discussion

As previously discussed in section 2.8, the rare-earth nuclei in the deformed mass region of $A \approx 130$ below $N = 82$ and above $Z = 50$, show a range of nuclear structure phenomena. Since the proton and neutron Fermi surfaces lie between these shell gaps, it is possible to narrow down the orbitals that are involved in forming the various rotational structures that are observed. The states contained within this region are in the negative-parity $h_{11/2}$ shell and the positive-parity $g_{7/2}$,

$d_{5/2}$, $d_{3/2}$ and $s_{1/2}$ shells, shown in Fig. 5.7. As a result of this, it is possible to presume that the Nilsson states within these orbitals are dominant when assigning configuration, and that the odd-N nuclei in this mass region have low-lying excited states and ground-state bands that are predominantly of positive parity. To further understand the nuclear structure in this region, it is necessary to interpret the experimental alignments and Routhians deduced from the level scheme within the theoretical framework of the CSM.

5.4.1 Band 1

Further to the identification of the Nilsson orbitals involved in assigning configurations at $Z = 59$ and $N = 70$ as shown in Fig. 5.7, it is then possible to extend this to the CSM calculations in order to identify the specific quasiparticle configurations. From the systematics of other odd-A nuclei in this region, and with an assumed deformation of $\beta_2 = 0.284$ [49] and triaxiality parameter $\gamma = 0°$, the orbitals that are close to the Fermi surface as seen in the CSM calculations shown in Fig. 5.8, are $\pi h_{11/2}[541]3/2^-(EF)$, $\pi h_{11/2}[550]1/2^-(GH)$, $\pi g_{9/2}[404]9/2^+(AB)$, and $\nu h_{11/2}[523]7/2^-(ef)$. It should be noted that in odd-A nuclei, labels correspond to Nilsson levels at $0 = \hbar\omega$, and these labels refer to the dominant admixture in the wavefunctions. The quasiparticle labelling scheme is presented in Table 5.2.
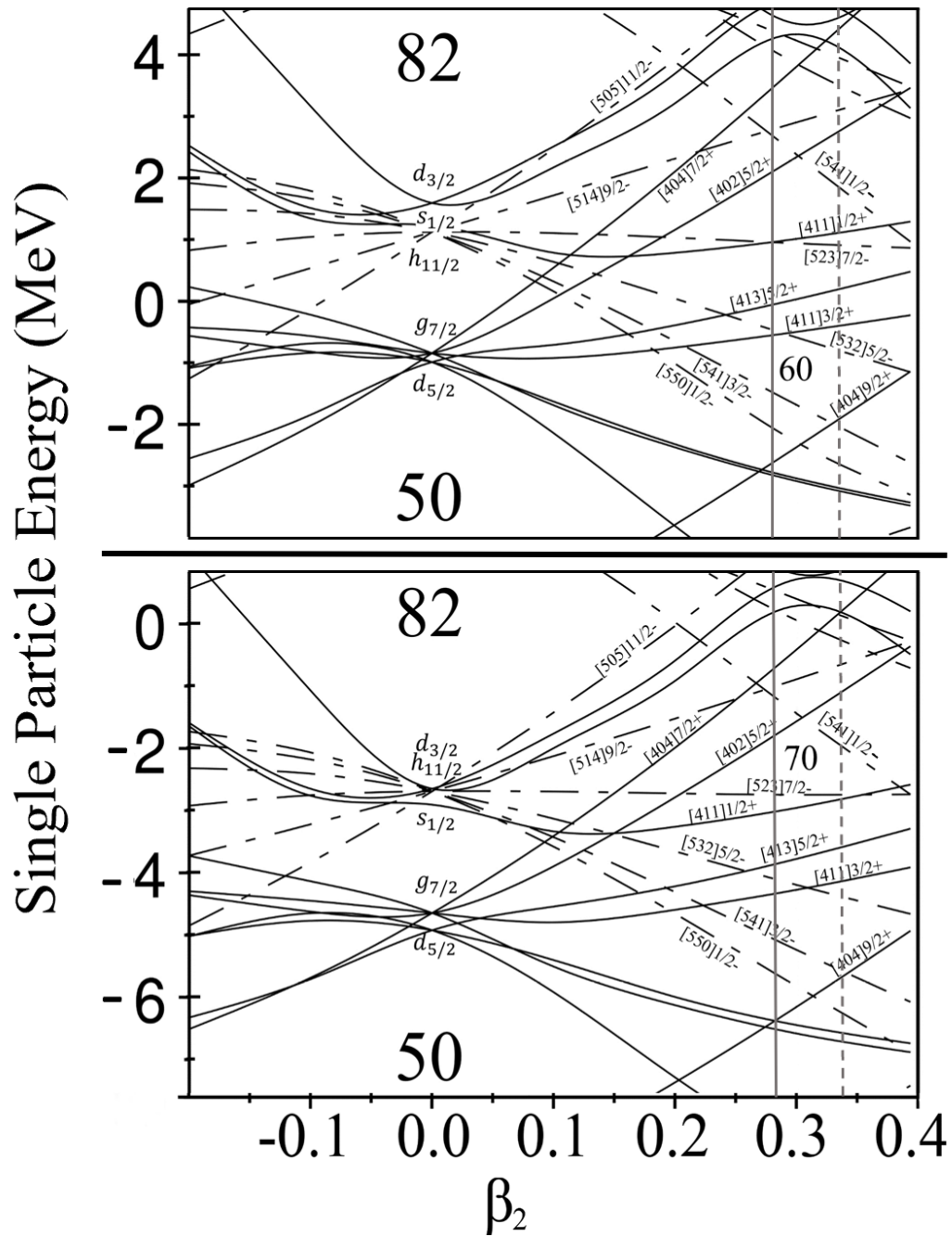
Figure 5.7: Nilsson diagrams showing the single-particle energy as a function of the β_2 deformation parameter for bands in ^{129}Pr. Top: Nilsson diagram for protons. Bottom: Nilsson diagram for neutrons. The states contained within this region are in the negative-parity $h_{11/2}$ shell and the positive-parity $g_{7/2}$, $d_{5/2}$, $d_{3/2}$ and $s_{1/2}$ shells. The deformation parameter used for band 1 is $\beta = 0.284$ shown by the vertical solid line. The deformation parameter for band 4 is $\beta = 0.345$ shown by the vertical dashed line line.
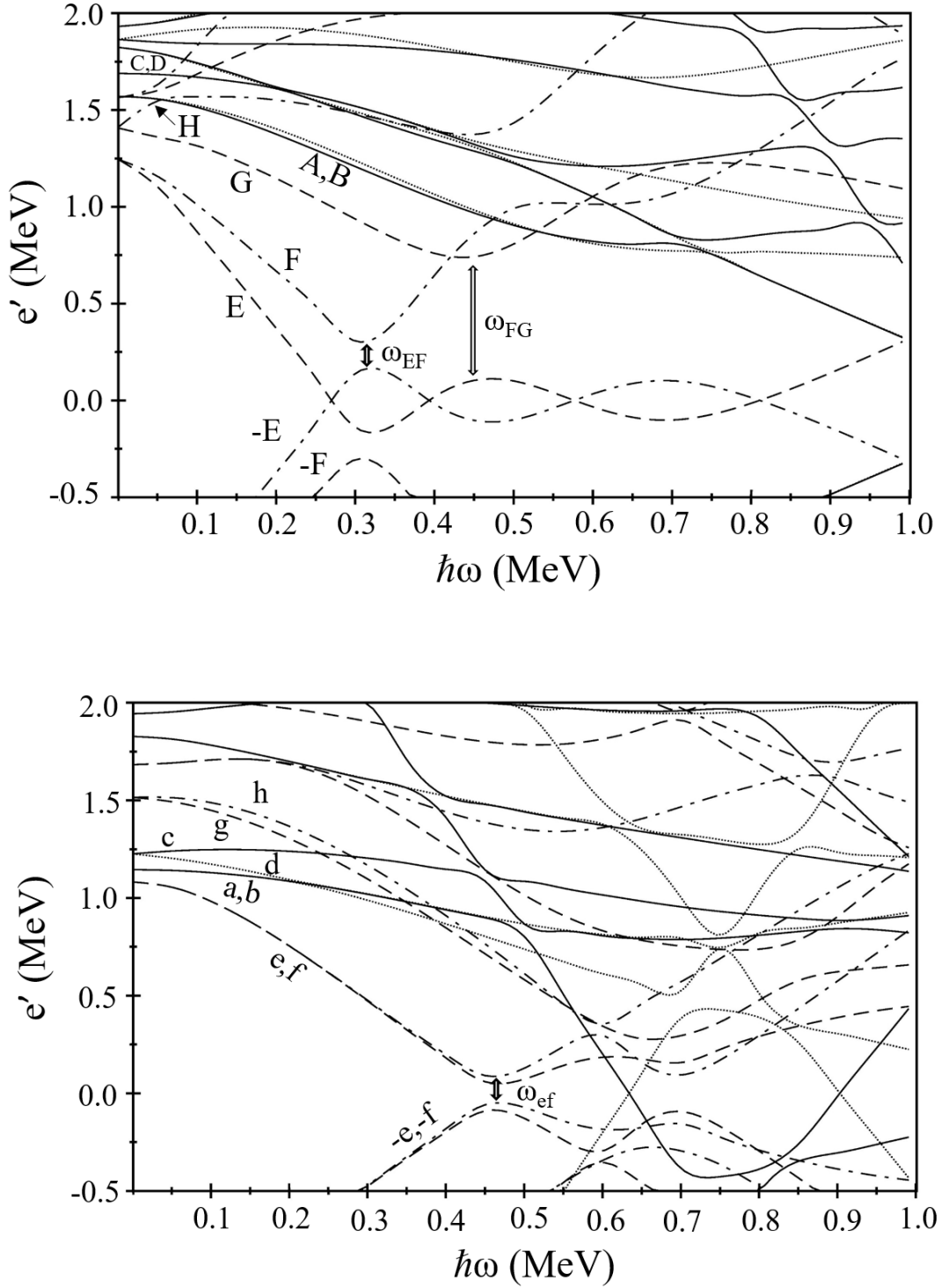
Figure 5.8: Cranked Shell Model quasiparticle Routhians generated using a universal Woods-Saxon potential for band 1 of ^{129}Pr. Top Panel: protons and Bottom Panel: neutrons. $\beta_2 = 0.284$, $\beta_4 = 0.0$, $\gamma = 0.0°$. (π, α) : solid $= (+, +1/2)$, dotted $= (+, -1/2)$, dot-dash $= (-, +1/2)$ and dashed $= (-, -\frac{1}{2})$. Arrows show the crossing frequencies. See text for details.

Table 5.2: Quasiparticle labelling scheme for ^{129}Pr

	Protons			Neutrons	
Label	Nilsson State	$(\pi, \alpha)_n$	Label	Nilsson State	$(\pi, \alpha)_n$
A	$g_{9/2}[404]9/2^+$	$(+,+1/2)_1$	a	$g_{7/2}[402]5/2^+$	$(+,+1/2)_1$
B	$g_{9/2}[404]9/2^+$	$(+,-1/2)_1$	b	$g_{7/2}[402]5/2^+$	$(+,-1/2)_1$
C	$d_{5/2}[411]3/2^+$	$(+,+1/2)_2$	c	$s_{1/2}[411]1/2^+$	$(+,+1/2)_2$
D	$d_{5/2}[411]3/2^+$	$(+,-1/2)_2$	d	$s_{1/2}[411]1/2^+$	$(+,-1/2)_2$
E	$h_{11/2}[541]3/2^-$	$(-,-1/2)_1$	e	$h_{11/2}[523]7/2^-$	$(-,-1/2)_1$
F	$h_{11/2}[541]3/2^-$	$(-,+1/2)_1$	f	$h_{11/2}[523]7/2^-$	$(-,+1/2)_1$
G	$h_{11/2}[550]1/2^-$	$(-,-1/2)_2$	g	$f_{7/2}[541]1/2^-$	$(-,-1/2)_2$
H	$h_{11/2}[550]1/2^-$	$(-,+1/2)_2$	h	$f_{7/2}[541]1/2^-$	$(-,+1/2)_2$

It can be deduced that the negative-parity yrast band is built upon a decoupled $h_{11/2}$ proton, and is the result of the odd proton occupying a low-Ω $h_{11/2}$ orbital. Band 1 has been assigned as the signature $\alpha = -1/2$ component (label E) of the $h_{11/2}[541]\ 3/2^-$ Nilsson configuration. DCO measurements for transitions up to 954 keV are confirmation of a cascade of stretched E2 transitions that are consistent with previous work [49] and is the result of the aforementioned decoupled $h_{11/2}$ proton coupling with an even-even core (in this case ^{128}Ce) [56]. Figure 5.9 shows the backbend seen in the neighbouring ^{128}Ce at around $\hbar\omega = 0.3$ MeV, showing that the change in alignment in ^{129}Pr is due to the first proton alignment being blocked by the odd proton. A result of this is that there is no backbend observed for band 1 in Fig. 5.10.

From the experimental alignment (Fig. 5.10), there is an initial change in alignment, Δi_x of $\sim 5\hbar$ from $0.30 - 0.45$ MeV $\hbar^{-1}$. Further theoretical support for this comes from the CSM calculations shown in Fig. 5.8, where it can be seen that the states E and $-F$ (or $-E$ and F) approach each other at a crossing frequency of $\omega \approx 0.32$ MeV $\hbar^{-1}$ (ω_{EF}). Since there is an odd particle, in this case for $Z = 59$ an odd proton, this proton blocks this orbital, and as such is unable to be a part of the alignment process. The next possible crossing is the FG crossing (ω_{FG}), that occurs at ~ 0.45 MeV $\hbar^{-1}$ and is calculated to have an alignment of $\Delta i_x \approx 5\hbar$, which then allows a change from a one-quasiparticle configuration to a three-quasiparticle

configuration. Hence, the 'up-bend' seen in Fig. 5.10 is indicative of the alignment of the FG quasiparticles, reflecting the magnitude of the interaction between the two bands at the FG crossing. The experimental Routhians in Fig. 5.11 also show a change in the downward trend at the same frequency (~ 0.45 MeV $\hbar^{-1}$) predicted by the CSM calculations for the second proton crossing. The total change in alignment seen in the CSM for ω_{FG} can be calculated as a sum of the slopes and is $\sim 9.5\hbar$, thus making this a good candidate when compared to the experimental alignment of $\sim 10\hbar$ observed. The up-bend signals evidence of a strong interaction where there is a 'smearing' out of the alignment process over several states. Alternatively, ef neutrons (bottom plot of Fig. 5.8) align at approximately the same frequency (~ 0.45 MeV $\hbar^{-1}$). The change in alignment, Δi_x is $\sim 2.5\hbar$ which may contribute to the FG crossing as a gradual alignment. However, this neutron alignment is insufficient to produce the experimental gain by itself.

Therefore, it can be concluded that band 1 is a $\pi h_{11/2}(E)$ one-quasiparticle configuration at low spin, going to a $\pi h_{11/2}^3(EFG)$ three-particle configuration at higher spins.

5.4.2   Bands 2 and 3

Two further rotational sequences of transitions that have also been newly assigned to ^{129}Pr can be seen in bands 2 and 3. Several linking transitions between these bands and band 1 have also been observed. As with band 1, there is an initial experimental alignment observed of $\sim 10\hbar$ (Fig. 5.10). Both the alignment and Routhian plots as shown in Fig. 5.10 and Fig. 5.11 respectively, show that these two bands have almost identical behaviour, as would be expected from two bands based on the same configuration, with opposite signature. It can be seen clearly that these are signature partner bands, with one band lying at the midpoint of the other. At low spin, the nucelar strucutre can be well descried as a single quasiparticel, where only the motion of the valence nucleons are used to desribe lower energy states. At higher spins, it is the collective behaviour of nucelons that leads to the emergence of collective excitations (rotational bands), and it is this increase in spin that is associated with an increase in nuclear deformation. As a result of higher
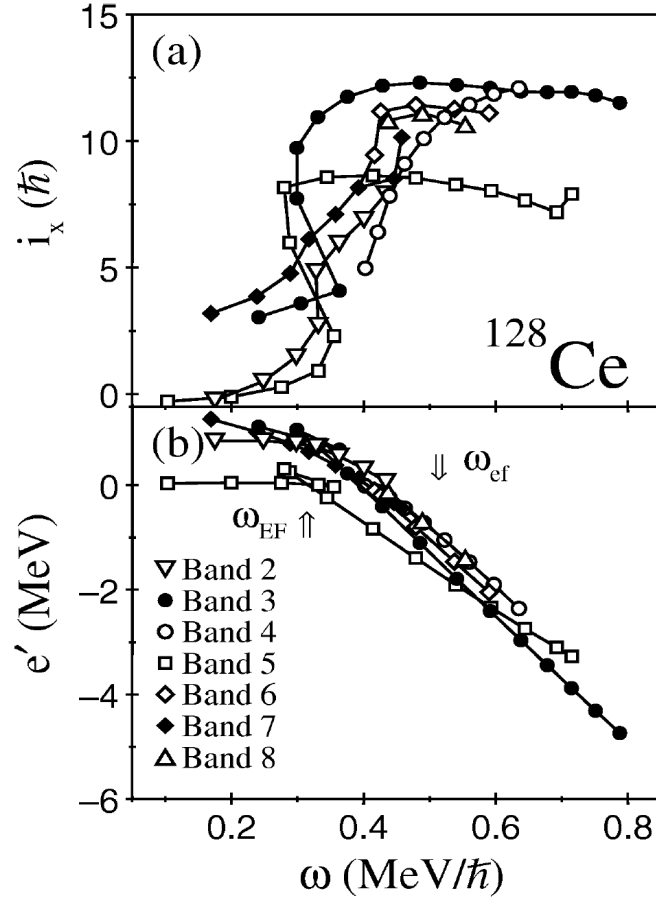
Figure 5.9: Figure taken from Ref. [56] to show (a) the backbend observed in the experimental alignments, and (b) the routhians, both plotted as a function of rotational frequency for all bands of ^{128}Ce. See text for details.

energy levels becoming accessible, additional nucleons can now occupy the higher energy states – leading to the appearance of additional quasiparticles. Thus, it can be deduced that bands 2 and 3 will not be a single quasiparticle configuration, but are likely to be a three-quasiparticle configuration. To explore suitable candidates for configuration assignments, it is important to again look at the states that lie close to the Fermi surface. Based on the CSM calculations (Fig. 5.8) following on from the configuration assignment of band 1, bands 2 and 3 may be assigned a configuration of $\pi h_{11/2} \otimes \nu h_{11/2}^2$ (Eef/Fef).

CSM calculations show that the Eef configuration (band 2) has an alignment of $\sim 9.8\hbar$ and the Fef configuration (band 3) has an alignment of $\sim 8.5\hbar$. At $\hbar\omega \sim 0.3$ MeV, bands 2 and 3 have the same experimental alignment of $I_x \approx 10\hbar$, thus in good agreement with the CSM.
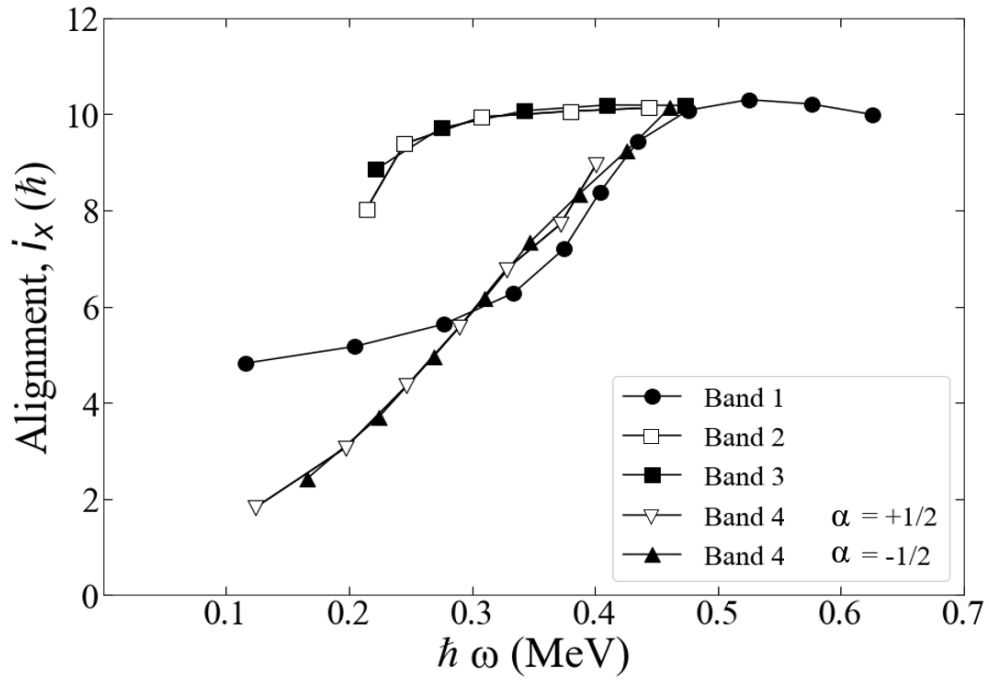
Figure 5.10: The experimental alignment plotted as a function of rotational frequency for all bands of ^{129}Pr. The values of Harris parameters used are $\mathcal{J}_0 = 18.8$ MeV$^{-1}\hbar^2$ and $\mathcal{J}_1 = 23.7$ MeV$^{-3}\hbar^4$ [48].
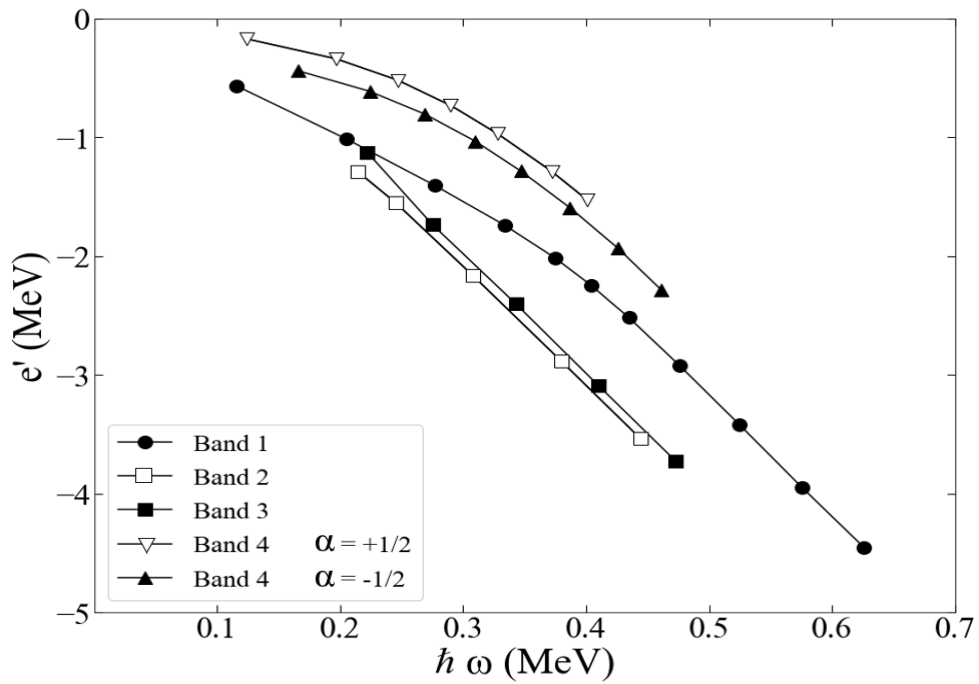
Figure 5.11: The experimental Routhian plotted as a function of rotational frequency for all bands of ^{129}Pr.

5.4.3   Band 4

The superdeformed bands in this mass region are generally associated with the occupation of the $i_{13/2}$ orbital, however as per previous research on the Pr isotopes discussed in Chapter 2 [26], and an assumed deformation of $\beta_2 = 0.345$ [49], the deformed structure observed (Band 4) has been associated with the $\pi g_{9/2}$ extruder orbital ($[404]9/2^+$), where the proton hole is responsible for the deformation-driving properties, and no $i_{13/2}$ orbitals are occupied.

This band structure contains fairly low excitation energies with the occurrence of strong magnetic dipole transitions between the signature partners, as well as having a low degree of signature splitting. This is indicative of an axially symmetric deformed prolate shaped nucleus. From this assessment, it can be deduced that this band structure is likely to be based on high-Ω orbitals, with the only suitable configuration candidate near the Fermi surface being the $\pi g_{9/2}$ (AB) extruder orbital.

A low initial experimental alignment (Fig. 5.10) is consistent with the CSM calculations shown in Fig. 5.12. It can be seen from CSM calculations that the EF quasiproton orbits fall quickly in energy with increasing rotational frequency. Based on this, it can be concluded that the configuration for band 4 is likely to be a one-quasiparticle $\pi g_{9/2}(A)$ at low spin, transitioning to a three-quasiparticle state at higher spins with a likely configuration of $\pi g_{9/2} \otimes \pi h_{11/2}^2$ (AEF/BEF). The EF crossing at ~ 0.35 MeV is unblocked in this case, and this can be confirmed experimentally from the experimental Routhian by the small change is downward trend, observed at ~ 0.35 MeV in Fig. 5.11. The neutron alignment (Fig. 5.12) does not occur until ~ 0.55 MeV, so is an unlikely candidate for the configuration of this band. It has been reported that an isomer decay γ-ray energy of 255.5 keV, decays to a level at 241.8 keV [51], and accounts for the majority of the decay intensity of this coupled band [49]. However, in this present data set this transition is not observed, possibly due to it decaying from an isomeric state. Figure 5.13 shows a level scheme containing the low-lying levels not seen in the data from this work can be seen in work carried out in Ref. [51].
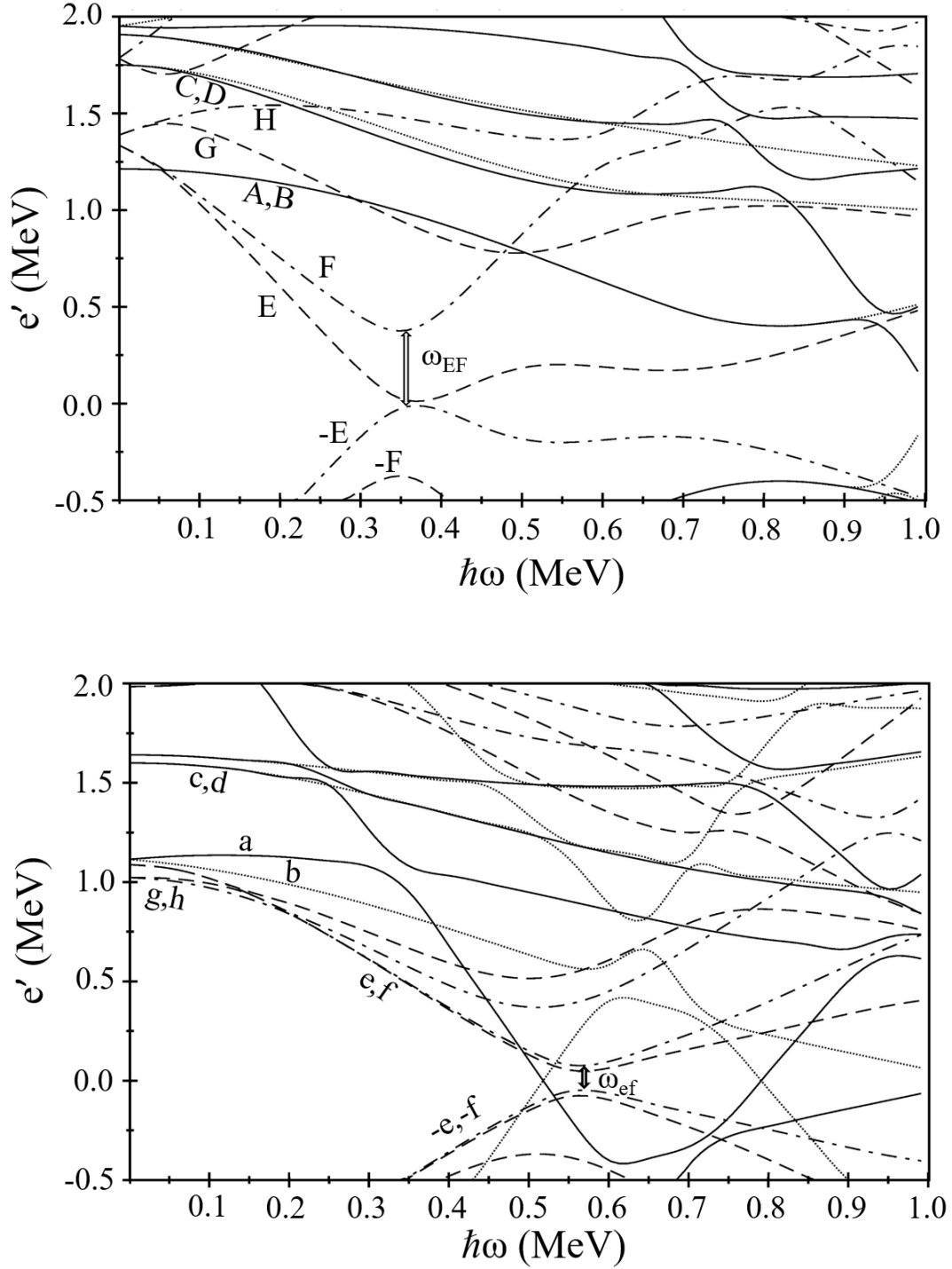
Figure 5.12: Cranked Shell Model quasiparticle Routhians generated using a universal Woods-Saxon potential for band 4 of ^{129}Pr. Top Panel: protons and Bottom Panel: neutrons. $\beta_2 = 0.345$, $\beta_4 = 0.0$, $\gamma = 0.0°$. (π, α) : solid = $(+, +1/2)$, dotted = $(+, -1/2)$, dot-dash = $(-, +1/2)$ and dashed = $(-, -1/2)$. Arrows show the crossing frequencies.
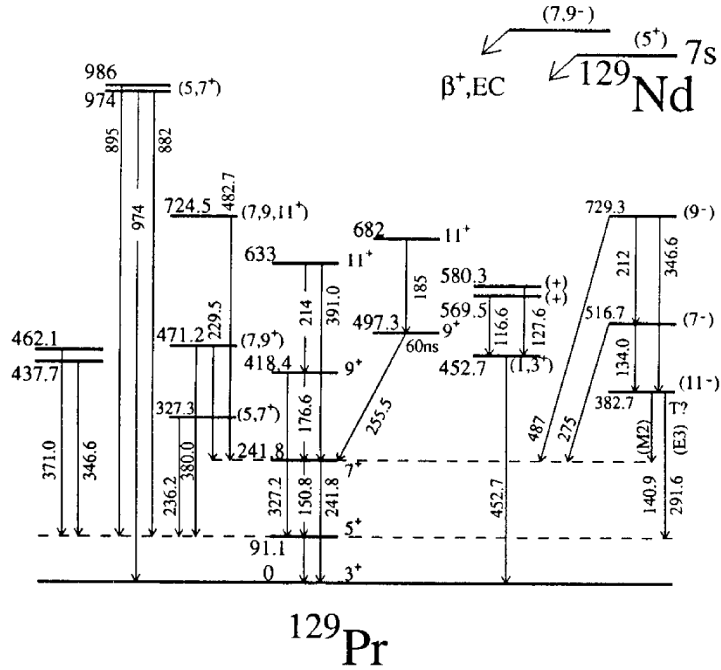
Figure 5.13: Figure taken from Ref. [51] to show the low-lying levels in ^{129}Pr populated in the decay of ^{129}Nd (note that spins are multiplied by two).

DCO measurements proved to be difficult to obtain from this band, aside from a single value of 0.89 ± 0.22 obtained for the transition energy of 480 keV. Within the range of the associated error, this shows that it does lie close to the estimated DCO ratio value of around 0.5 expected for an E2 transition.

5.4.4 Summary of ^{129}Pr

In summary, the level scheme in this work has been deduced for ^{129}Pr and shows two new sidebands (bands 2 and 3) that link to band 1. It has been concluded that band 1 is a $\pi h_{11/2}(E)$ one-quasiparticle configuration at low spin, going to a $\pi h_{11/2}^3 (EFG)$ three-particle configuration at higher spins. The newly presented sidebands found in this work, bands 2 and 3, have be assigned a configuration of $\pi h_{11/2} \otimes \nu h_{11/2}^2$ (Eef/Fef). A deformed structure based on the $g_{9/2}$ extruder orbital (band 4) has also been identified and extended from previous work. It has been concluded that band 4 is likely to be a one-quasiparticle configuration ($\pi g_{9/2}(A)$) at low spins, going to a three-quasiparticle configuration of $\pi g_{9/2} \otimes \pi h_{11/2}^2$ (AEF/BEF), at higher spins. From the present data there is no evidence non-yrast continuation of the one-quasiparticle band after the band-crossing. Experimentally measured alignments

and Routhians are in good agreement with CSM calculations, thus providing new insight into this nucleus and how the observed structures can be interpreted within the known systematics of Pr isotopes.

Chapter 6

Alignments and Band Crossing in ^{132}Sm

6.1 Motivation and Previous Work

As outlined in chapter 5 of this work, the mass region of $A \approx 130$ provides an interesting area of study in that the nuclei near $N, Z = 64$ are predicted to be at the centre of deformation for this region [58]. The structures of the lightest even-even Sm isotopes in this mass region are not well-documented, therefore further studies of their underlying structures are desirable to understand how their properties change far from stability.

The first investigation of the excited states of ^{132}Sm (Z=62, N=70), identified for the first time the yrast band in this nucleus. The work was carried out by Wadsworth et al. [58], using the Daresbury recoil separator [59] in conjunction with ten bismuth germanate suppressed Ge detectors and five NE213 liquid scintillators. Further study of this nucleus is of interest in order to contribute to an understanding of the rotational alignment processes in this region.

This chapter presents the discovery of the S-band in ^{132}Sm, and a reinterpretation of the known higher spin states in terms of shape coexistence.

6.1.1 Sm Systematics

As with the systematic comparison of Pr isotopes in chapter 5, a similar trend can be observed in the lower spin states of the Sm isotopes in this region, shown in Fig. 6.1. The decrease in energy level spacing towards the lighter Sm isotopes shows an increase in deformation with decreasing neutron number. Further to this, the increase in deformation can also be seen with increasing proton number, as shown in Fig. 6.2.
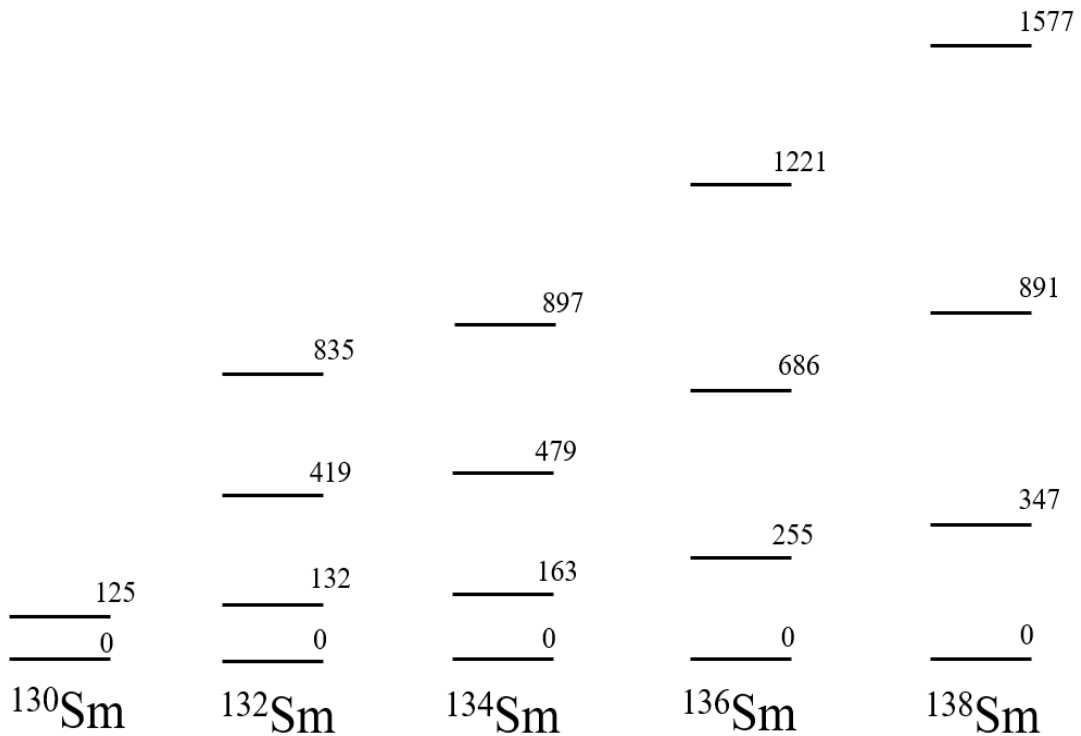
Figure 6.1: The systematics of the low spin parts in several Sm isotopes, ranging from ^{130}Sm to ^{138}Sm [1][58][60][61][62]. The lowest energy levels of the $h_{11/2}$ structures have been set to zero to be used as a reference. Levels are labelled by their excitation energy in keV.
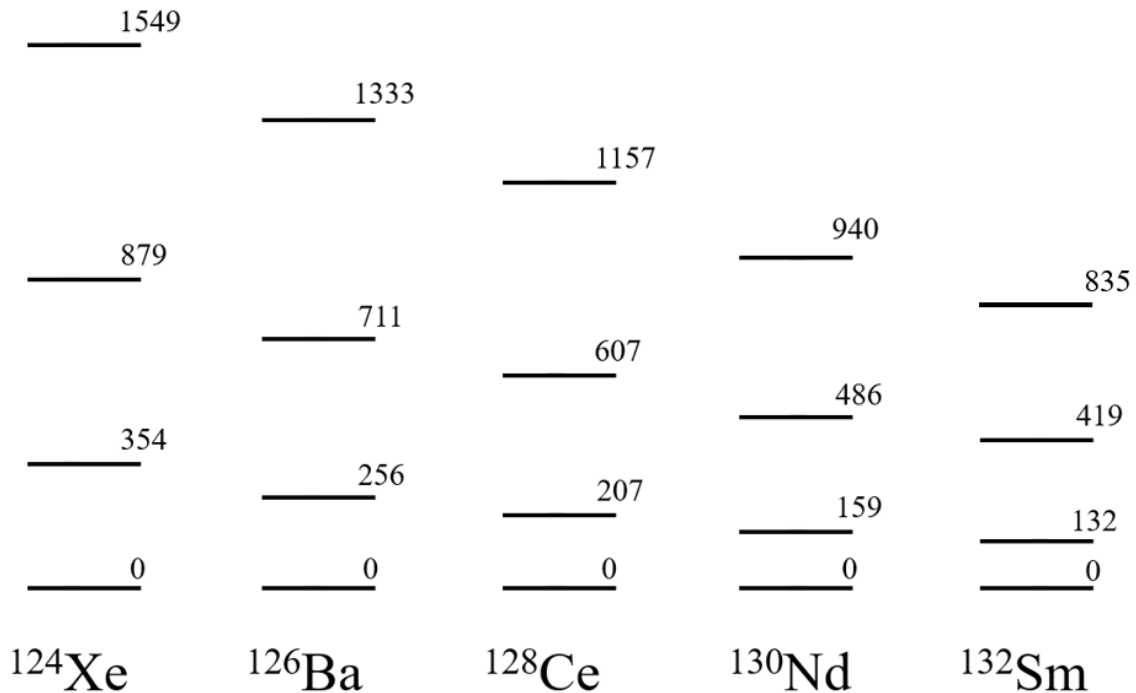
Figure 6.2: The systematics of the low spin parts in several Sm isotones ranging from ^{124}Xe (Z=54) to ^{132}Sm (Z=62) [63][64][56][65][58]. The lowest energy levels of the $h_{11/2}$ structures have been set to zero to be used as a reference. Levels are labelled by their excitation energy in keV.

6.2 Experimental Details

The experimental details are the same as those outlined in section 5.2 of this work, with ^{132}Sm being obtained in the fusion-evaporation reaction ^{58}Ni(^{78}Kr, $2p2n$)^{132}Sm. Spectra displayed in this chapter are not mass-gated as in Chapter 5, due to the limited statistics for the nucleus produced in this reaction channel. In contrast to the γ-ray spectra produced for ^{129}Pr, the contamination was much lower in this case and the spectra are less strongly affected by the strong ^{129}Nd.

6.3 Results

The proposed level scheme obtained for ^{132}Sm from the present set of data is displayed in Fig. 6.3. The study of this nucleus was chosen as its structure is not currently well documented in this region of maximal deformation, and it is desirable

to further explore the possibility of shape coexistence. The most recently published results show γ-ray energy transitions up to 837 keV within the ground-state band. As before, the experimental results will be discussed for each of the bands observed in the level scheme, and further analysis will be examined in the discussion section of this chapter.

6.3.1   Band 1

Band 1 has been tentatively extended from the work carried out by Wadsworth et al. [58], with a new transition of γ-ray energy 905 keV. The energies of this band are justified by a spectrum with a sum of doubles gatelist of the transitions from 132 keV up to 905 keV, shown in Fig. 6.4. It has been assumed following the work carried in Ref. [58] and Ref. [61] that these γ rays form a cascade of stretched E2 transitions linking the 0^+, 2^+, 4^+ etc. states as seen in even-even nuclei.

6.3.2   Band 2

From the current data, it has been observed that there is a cascade of previously unobserved transitions that appear to form a second rotational cascade, connected to the GSB via a transition of 408 keV. This band and its linking in to the GSB can be justified by a sum of doubles gatelist from 518 keV up to 804 keV, and is shown in plot (b) in Fig. 6.4.

The level scheme for ^{132}Sm deduced in this work is shown in Fig. 6.3, and the measured properties of γ rays observed, and their associated quantities are recorded in Table 6.1.
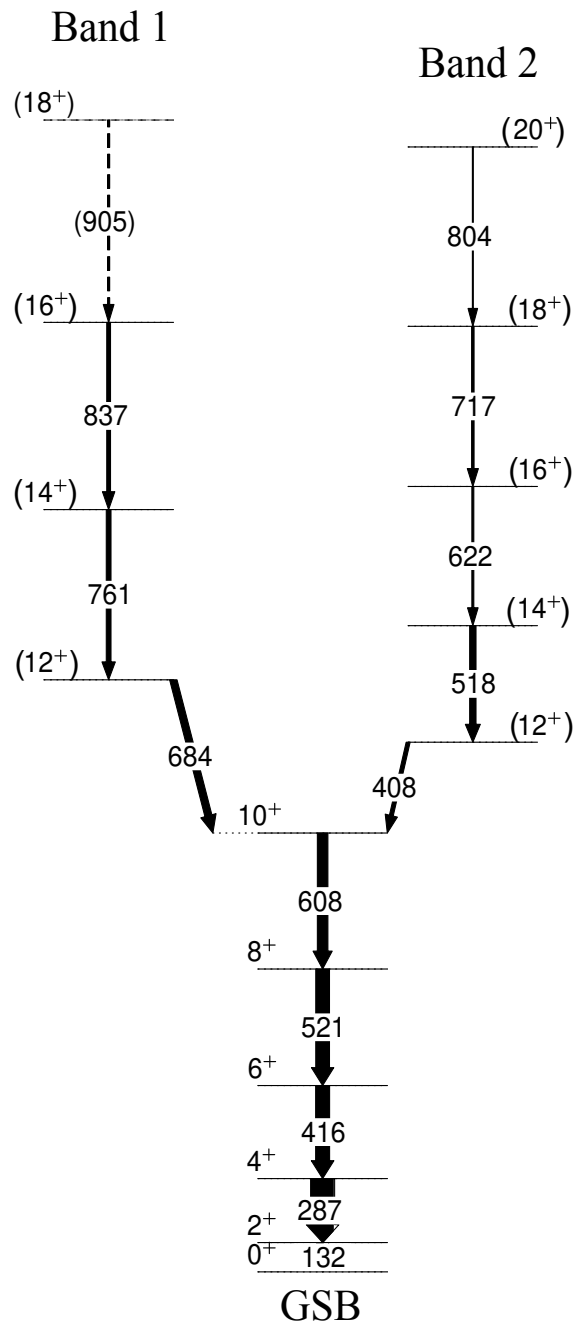
Figure 6.3: Proposed level scheme of ^{132}Sm. Brackets on spins and parities indicate tentative assignments where there are a lack of DCO measurements. Widths of arrows correspond to relative intensities
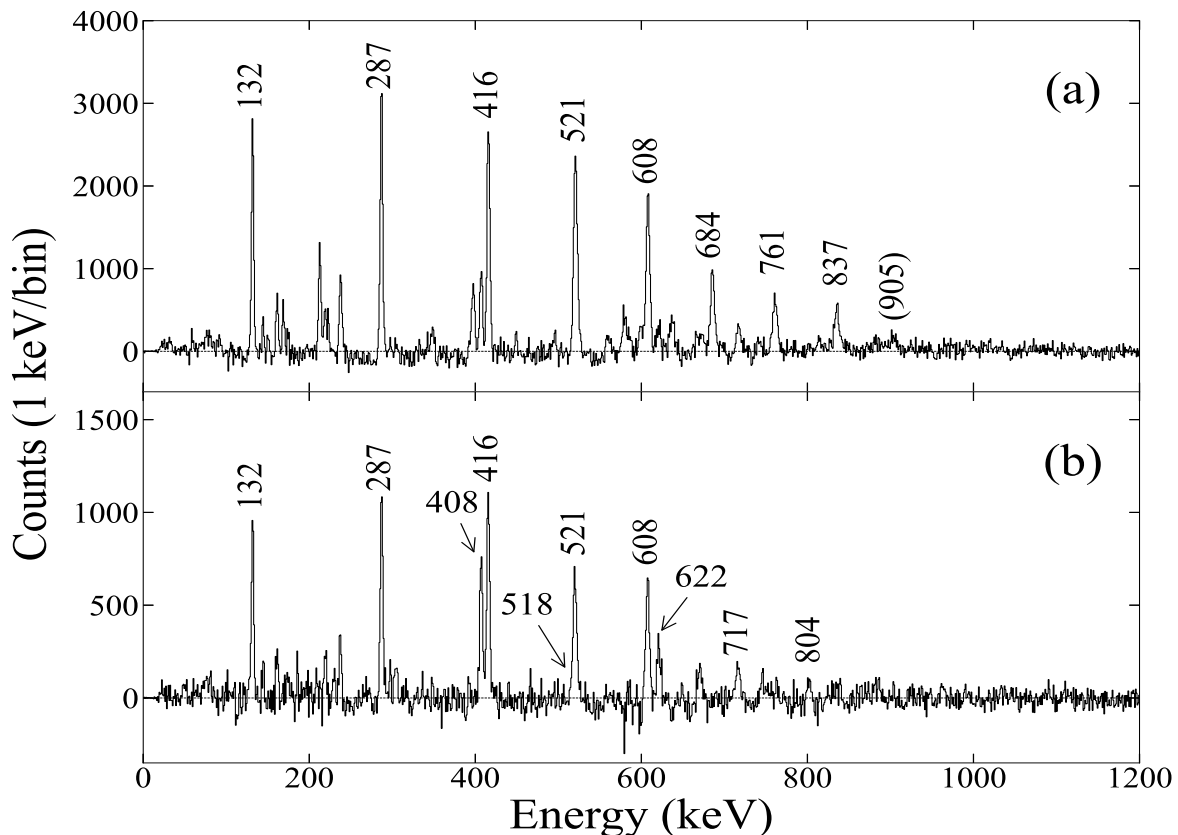
Figure 6.4: Spectra of gatelists for ^{132}Sm. (a) is a sum of doubles gatelist of x = 132 keV up to 905 keV to show the GSB and Band 1. (b) is a sum of doubles gatelist of x = 132 keV up to 608 keV, and y = 518 keV up to 804 keV to show the GSB up to spin 10^+ and Band 2. Visible peaks in these spectra that are not labelled correspond to contaminating γ rays from neighbouring nucleus ^{132}Nd and do not form part of the structure of ^{132}Sm.

Table 6.1: List of γ rays and their measured properties for ^{132}Sm. Quantities in brackets denote a tentative assignment to its value.

E_γ (keV)	I_γ	$J_i^\pi \to J_f^\pi$	DCO	Multipolarity (λ L)	Band
GSB/Band					
1					
132	75.1	2+ $\to$ 0+	1.90 ± 0.16	E2	1
287	100.0	4+ $\to$ 2+	1.44 ± 0.12	E2	1
416	98.4	6+ $\to$ 4+	1.26 ± 0.11	E2	1

E_γ (keV)	I_γ	$J_i^\pi \to J_f^\pi$	DCO	Multipolarity (λ L)	Band
521	100.2	8+ → 6+	1.09 ± 0.09	E2	1
608	84.2	10+ → 8+	1.17 ± 0.11	E2	1
684	46.8	(12+) → (10+)	-	(E2)	1
761	33.2	(14+) → (12+)	-	(E2)	1
837	27.9	(16+) → (14+)	-	(E2)	1
(905)	-	(18+) → (16+)	-	(E2)	1
Band 2					
408	26.9	(12+) → (10+)	-	(E2)	2
518	18.6	(14+) → (12+)	-	(E2)	2
622	13.2	(16+) → (14+)	-	(E2)	2
717	8.5	(18+) → (16+)	-	(E2)	2
804	5.5	(20+) → (18+)	-	(E2)	2

6.4 Discussion

A further observation that is in agreement with previous studies is the ratio of the first 4^+ and 2^+ states given by

$$\frac{E(4^+)}{E(2^+)} = 3.18 \tag{6.1}$$

which is approaching the value of an axially symmetric rotor (3.33 is the 'perfect' value for an axial prolate rotor), indicative of the type of deformation present.

This can be confirmed from these data through the following calculation – from an empirical fit to E2 transition rates, it is found that the decay rate (probability) from the first excited 2^+ state in an even-even nucleus to its 0^+ ground state is given by

$$T_\gamma(E2; 2^+ \to 0^+)[s^{-1}] = (4 \pm 2) \times 10^{10} Z^2 E_\gamma^4 A^{-1} \tag{6.2}$$

from which the "Grodzins" estimate [66] of the nuclear quadrupole deformation can be derived as

$$\beta_2 \approx \left[\frac{1225}{A^{\frac{7}{3}} E(2^+)} \right]^{\frac{1}{2}} \tag{6.3}$$

giving a quadrupole deformation of 0.323, which has been used for the CSM calculations in this chapter.

From the DCO measurements recorded in Table 6.1, it can be seen that they are higher than those measured for ^{129}Pr. The shape of the nucleus plays a crucial role in determining its scattering properties. This may be indicative that ^{132}Sm has a more deformed or elongated shape compared to ^{129}Pr, thus leading to enhanced scattering and, consequently, higher DCO measurements.

At zero spin, i.e. $0\hbar\omega$, an even-even nucleus such as in this case has a ground state band (GSB) that corresponds to a 'vacuum' configuration since all particles are paired.

Since the deformation of 0.323 is only an estimate in this case for the GSB, the CSM calculations can only provide limited information when making comparisons to what is experimentally measured. Thus, single-particle energy Nilsson diagrams (Fig. 6.5) are significant in determining the orbitals involved in assigning structural configurations.

6.4.1   Band 1

From the CSM calculations shown in Fig. 6.6, there is evidence of an $h_{11/2}$ neutron alignment at higher frequencies ($\hbar\omega \sim 0.55$), however this is not observed in the current experimental data. In this case, there is also the absence of the theoretical $h_{11/2}$ neutron alignment experimentally. Discrepancies between the experimental measurements and theoretical calculations may be related to proton-neutron interactions and the deformation driving effects due to the role of intruder states (discussed in section 2.7) that are observed in this mass region.

Evidence of an interaction can be seen by a 'kink' in the alignment in Band 1 at around 10^+ ($\hbar\omega \sim 0.35$) (Fig. 6.7). Since the neutron alignment predicted by the CSM calculations in Fig. 6.6 cannot be seen in these data, Fig. 6.5 showing the single-particle energy levels may be used to deduce the orbitals involved that are
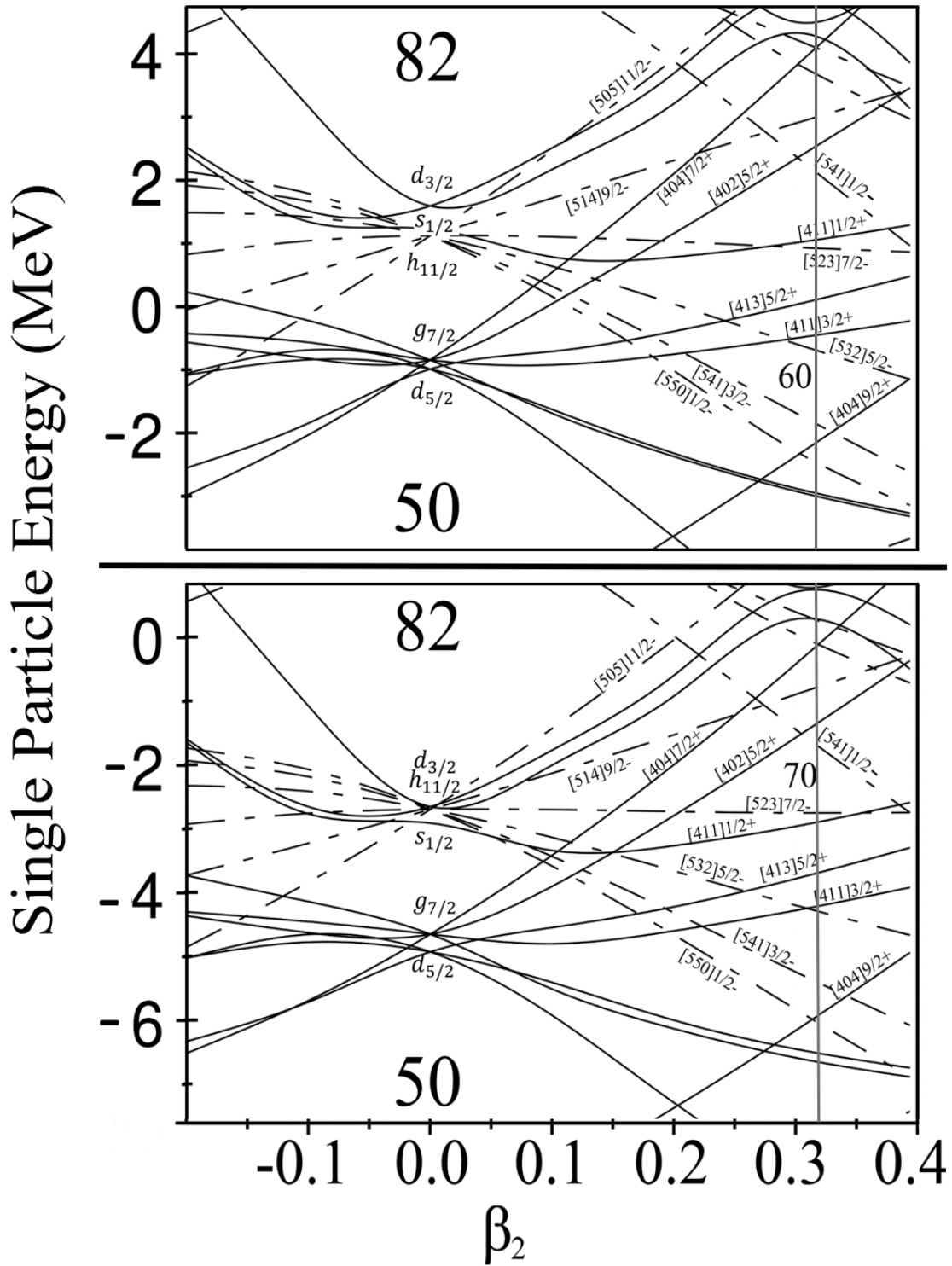
Figure 6.5: Nilsson diagrams showing the single-particle energy as a function of the β_2 deformation parameter for ^{132}Sm. Top: Nilsson diagram for protons. Bottom: Nilsson diagram for neutrons. The states contained within this region are in the negative-parity $h_{11/2}$ shell and the positive-parity $g_{7/2}$, $d_{5/2}$, $d_{3/2}$ and $s_{1/2}$ shells. The deformation parameter used is $\beta = 0.323$
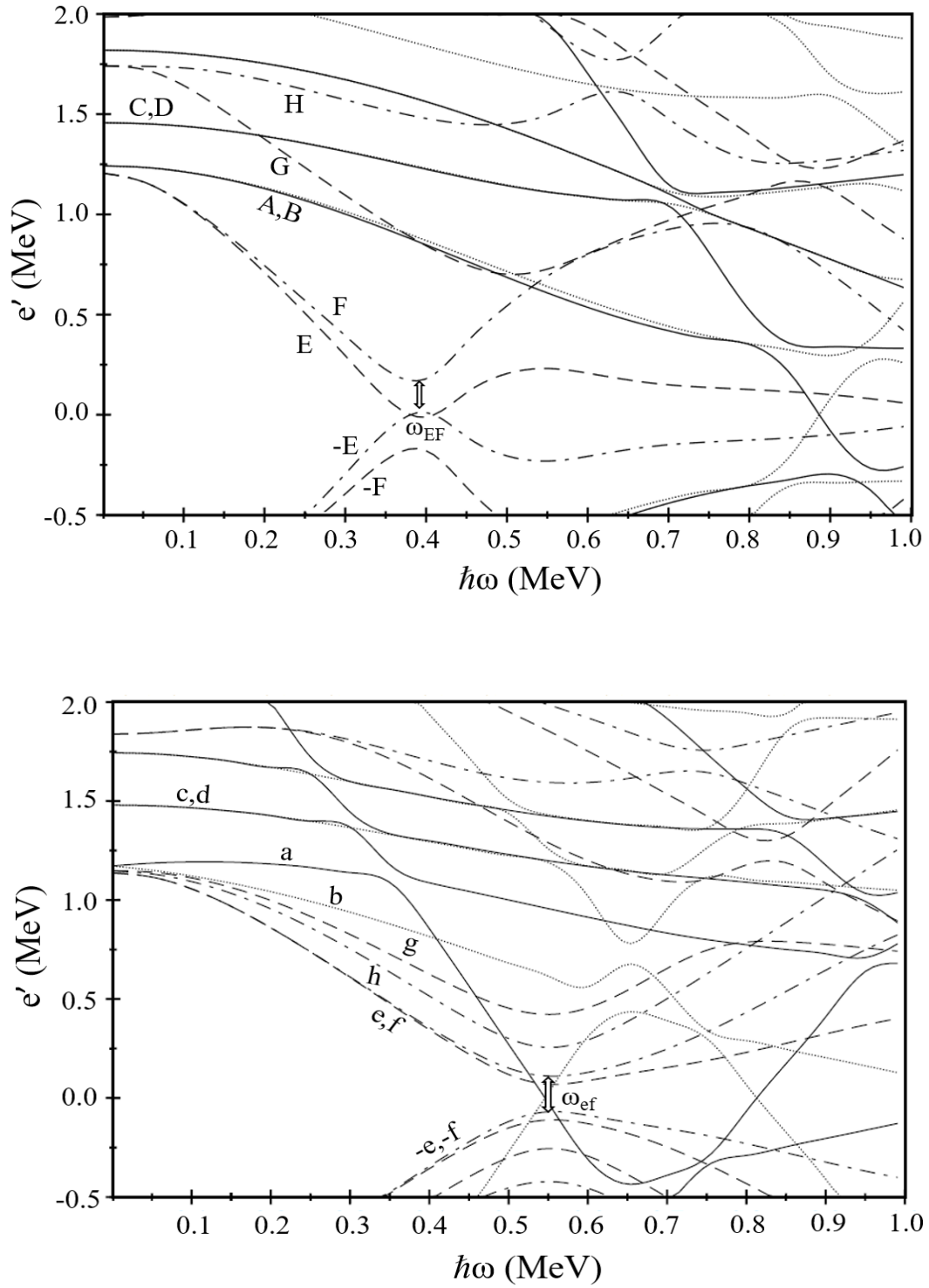
Figure 6.6: Cranked Shell Model quasiparticle Routhians generated using a universal Woods-Saxon potential for band 1 of ^{132}Sm. Top Panel: protons and Bottom Panel: neutrons. $\beta_2 = 0.323$, $\beta_4 = 0.0$, $\gamma = 0.0°$. (π, α) : solid = $(+, +1/2)$, dotted = $(+, -1/2)$, dot-dash = $(-, +1/2)$ and dashed = $(-, -1/2)$. Arrows show the crossing frequencies.

observed experimentally and give further clues as to why this interaction is taking place. The kink observed in Fig. 6.7 shows a continuation of the GSB. As previously discussed, it may be deduced that this is not a neutron alignment since this is not seen experimentally, but is rather indicative of a band crossing.

The interaction may be interpreted as the scattering of a pair of neutrons into the $\nu h_{9/2}$ intruder orbital ([541]1/2$^-$), resulting in a paired band crossing. Thus giving Band 1 a configuration of [541]1/2$^-$ beyond the 12$^+$ state of the GSB. This neutron placement into a downward sloping orbital is also responsible for further driving the nucleus towards a prolate shape, and is in good agreement with the evidence given in [58] that ^{132}Sm is a good prolate rotor. TRS calculations for the neighbouring nucleus ^{133}Sm [67] also concludes that these nuclei have well-deformed prolate shapes.

6.4.2 Band 2

It can be seen in the CSM calculations (Fig. 6.6 that the negative-parity quasiproton levels E and F, derived from the $\pi h_{11/2}$ orbitals, are nearest to the $Z = 62$ Fermi surface. A similar case is seen for the quasineutron levels, where e and f are the lowest energy states. In Fig. 6.6, the bottom diagram for protons shows the states E and -F or (-E and F) approach each other at only a frequency of around $\omega \approx 0.40 MeV\hbar^{-1}$. This can be associated with the alignment of a pair of protons originating from the $h_{11/2}$ subshell. From these CSM calculations, a sum of slopes for the EF protons give an alignment of $\sim 7\hbar$. The experimental alignment seen in Fig. 6.7 is only slightly lower than this at just over 6$\hbar$ thus showing consistency with the theoretical predictions. Based on this, it may be deduced that Band 2 is in fact the S-band (above $I_\pi = 10^+$) and is assigned a two-quasiproton $\pi(h_{11/2})^2(EF)$ configuration. Further support of this band assignment comes from neighbouring nuclei where this S-band has also been observed, such as in ^{128}Ce [56].
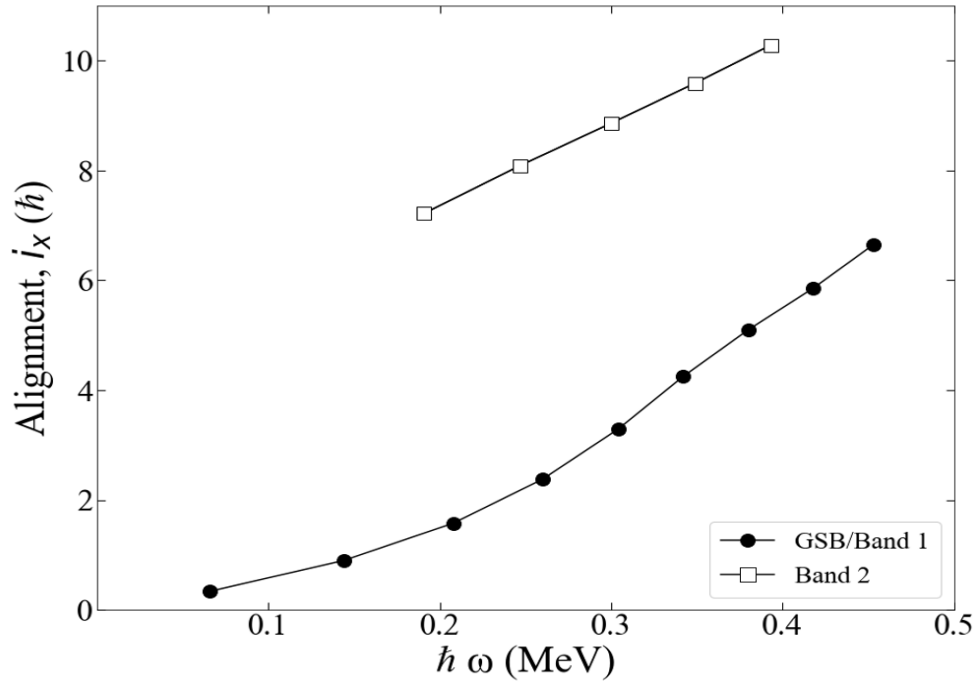
Figure 6.7: The experimental alignment plotted as a function of rotational frequency for all bands of ^{132}Sm. The values of Harris parameters used are $\Im_0 = 17.5$ MeV$^{-1}\hbar^2$ and $\Im_1 = 31.6$ MeV$^{-3}\hbar^4$ [58].
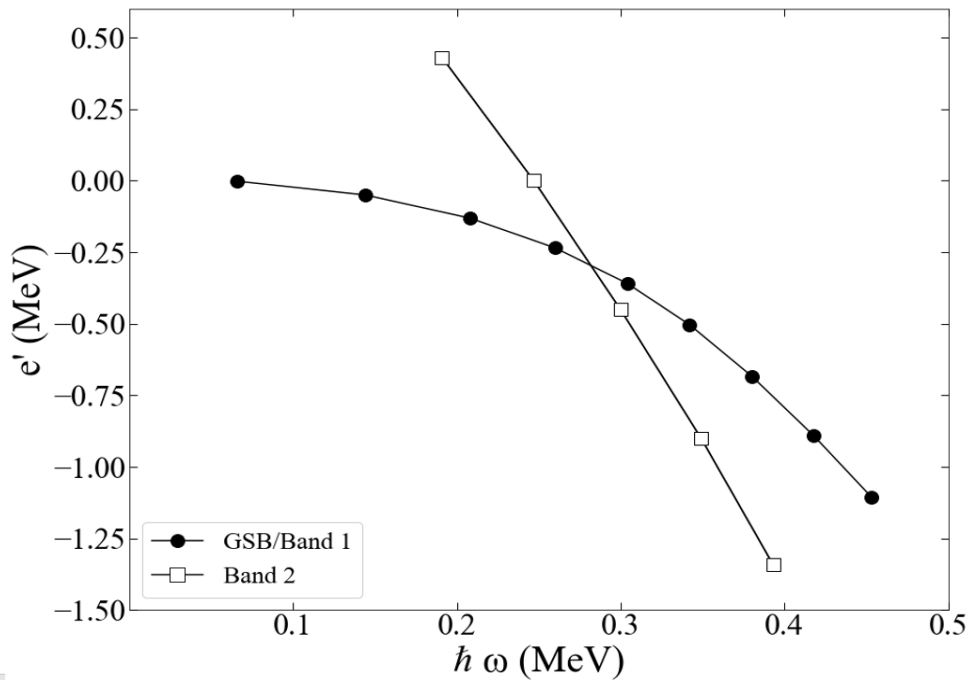
Figure 6.8: The experimental Routhian plotted as a function of rotational frequency for all bands of ^{132}Sm.

6.4.3   Summary of ^{132}Sm

In summary, band 1 has been assigned a configuration of $[541]1/2^-$, based on a pair of neutrons scattering into the downward sloping $\nu h_{9/2}$ intruder orbital. Band 2 has been identified as the S-band above the 10^+ state and has been assigned a configuration of $\pi(h_{11/2})^2$ (EF) corresponding to a two-quasiparticle structure. Since experimental observations were not in agreement with CSM calculations, these configuration assignments have been deduced using single-particle diagrams. Angular correlation ratios could not be obtained for band 2, thus spins and parities are tentative. For future work on this nucleus, it would be desirable to use g-factor measurements and perform mixing ratio calculations in order to provide further confirmation on the nature of Bands 1 and 2. The study of ^{132}Sm has shown new and interesting insights in to the role of neutron configurations in the formation of enhanced deformation bands in this region.

Chapter 7

Conclusion

The excited states in both ^{129}Pr and ^{132}Sm have been studied in this work. The experiment was carried out in JYFL-ACCLAB at the University of Jyväskylä, where the excited states of both ^{129}Pr and ^{132}Sm were populated via the ^{58}Ni(^{78}Kr, $\alpha 3p$) and ^{58}Ni(^{78}Kr, $2p2n$) reactions respectively. Experimental measurements of alignments and Routhians alongside theoretical CSM calculations have been used to deduce the possible configurations of the structures observed in both nuclei. Angular intensity ratio measurements were also calculated in order to obtain further clarity on the multipolarities of the transitions in the two nuclei.

Band 1 in ^{129}Pr has been identified as the yrast band and has been measured up to a spin of $55/2^-$, which is consistent with previous work. It has been concluded that band 1 is a one-quasiparticle configuration at low spin $(\pi h_{11/2}(E))$, going to a three-particle configuration $(\pi h_{11/2}^3(EFG))$ at higher spins. Two new sidebands (bands 2 and 3) have also been identified, and seen to link into band 1. These two further rotational sequences are seen to be signature partner bands, with a likely three-quasiparticle configuration of $\pi h_{11/2} \otimes \nu h_{11/2}^2$ (Eef/Fef). Band 4 is also consistent with previous studies on this nucleus and is confirmed to be a deformed structure based on the $\pi g_{9/2}[404]9/2^+$ orbital. Several new transitions have also been identified up to a spin of $43/2^+$. It may be concluded from CSM calculations that the configuration for band 4 is likely to be a one-quasiparticle configuration $(\pi g_{9/2}(A))$ at low spins, going to a three-quasiparticle configuration of $\pi g_{9/2} \otimes \pi h_{11/2}^2$ (AEF/BEF), at higher spins.

Following the identification of the known ground state band in ^{132}Sm, the discov-

ery of the S-band has provided new and interesting insights into the nuclear structure. Band 1 has been assigned a configuration of $[541]1/2^-$ originating from the $\nu h_{9/2}$ intruder orbital. Based on experimental measurements, it has been concluded that this band results from a pair of neutrons scattering in to the intruder orbital. Band 2 has been identified as the S-band above $I^\pi = 10^+$, and is assigned a configuration of $\pi(h_{11/2})^2(EF)$ corresponding to a two-quasiproton structure. Since CSM calculations have been unable to specifically identify the behaviour that is experimentally observed, configuration assignments to the observed rotational structures have been based on the single-particle energy diagrams shown in Fig. 6.5.

TRS calculations in the neighbouring nucleus ^{133}Sm [67] conclude that these nuclei have well-deformed prolate shapes, and this is further confirmation of the placement of nucleons in downward sloping orbitals. Further work on this nucleus could include calculating g-factor measurements for further confirmation as to the nature of the structures observed.

The experimental setup has been successful in producing a vast array of data, with the entirety of the available focal-place in use for the duration of the JM06 experiment. A small limitation should be noted as potentially causing restrictions in the data obtained – the charged particle veto detector, JYUTube, was not used in the JM06 experiment due to maintenance issues. The use of JYUTube at the target position may have been helpful in limiting background observed in any produced γ-ray spectra.

In conclusion, the analysis of the nuclei ^{129}Pr and ^{132}Sm has yielded new and unseen insights into their nuclear structure and properties. This mass region ($A \approx 130$) has been of particular interest to show how the deformation of nuclei changes towards the proton drip line. Since the neutron Fermi level approaches that of the protons with decreasing neutron number (i.e. both the proton and neutron Fermi surfaces are expected to be at similar levels in the $h_{11/2}$ subshell), this will show an increase in the possibility of proton-neutron interactions [10]. Furthermore, this work has highlighted the role of intruder orbitals that play a role in driving the deformation to elongated nuclear shapes. This study has also confirmed the use of the JUROGAM3 spectrometer array and MARA as efficient tools for investigating nuclear structure using gamma spectroscopy.

Bibliography

[1]   H. Tann. "Excited states in the highly deformed proton emitter ^{131}Eu". PhD thesis. University of Liverpool, 2022.

[2]   R.D. Woods and D.S. Saxon. "Diffuse surface optical model for nucleon-nuclei scattering". In: *Physical Review* 95.2 (1954), p. 577.

[3]   D.L. Hill and J.A. Wheeler. "Nuclear constitution and the interpretation of fission phenomena". In: *Physical Review* 89.5 (1953), p. 1102.

[4]   G. Andersson et al. "Nuclear shell structure at very high angular momentum". In: *Nuclear Physics A* 268.2 (1976), pp. 205–256.

[5]   *E. Paul, Nuclear Models.* 2003.

[6]   S. Ćwiok et al. "Single-particle energies, wave functions, quadrupole moments and g-factors in an axially deformed Woods-Saxon potential with applications to the two-centre-type nuclear problems". In: *Computer Physics Communications* 46.3 (1987), pp. 379–399.

[7]   C. Gustafson et al. *Nuclear deformabilities in the rare-earth and actinide regions with excursions off the stability line and into the super-heavy region.* Tech. rep. Lund Inst. of Tech., Sweden, 1967.

[8]   C.S. Purry et al. "Multi-quasiparticle isomers and rotational bands in ^{178}W". In: *Nuclear Physics A* 632.2 (1998), pp. 229–274.

[9]   CS Wu et al. "Relation between the kinematic and dynamic moments of inertia in superdeformed nuclei". In: *Physical Review C* 45.5 (1992), p. 2507.

[10] A. Bohr and B.R. Mottelson. In: *Proc. Int. Conf. on Nuclear Structure* (1977), Tokyo.

[11]   D.R. Inglis. "Particle derivation of nuclear rotation properties associated with a surface wave". In: *Physical Review* 96.4 (1954), p. 1059.

[12]   M.J.A. De Voigt, J. Dudek, and Z. Szymański. "High-spin phenomena in atomic nuclei". In: *Reviews of Modern Physics* 55.4 (1983), p. 949.

[13]   J.G. Valatin. "Comments on the theory of superconductivity". In: *Il Nuovo Cimento (1955-1965)* 7 (1958), pp. 843–857.

[14]   R. Bengtsson and S. Frauendorf. "Quasiparticle spectra near the yrast line". In: *Nuclear Physics A* 327.1 (1979), pp. 139–171.

[15]   S. M. Harris. "Higher order corrections to the cranking model". In: *Physical Review* 138.3B (1965), B509.

[16]   P.J. Twin. "Superdeformation in ^{152}Dy". In: *The Response of Nuclei under Extreme Conditions.* Springer, 1988, pp. 59–68.

[17]   A.J. Kirwan et al. "Mean-lifetime measurements within the superdeformed second minimum in ^{132}Ce". In: *Physical review letters* 58.5 (1987), p. 467.

[18]   *The Segre Chart.* https://www-nds.iaea.org/relnsd/vcharthtml/VChartHTML.html. Accessed: 2023-06-10.

[19]   R. Wyss and A. Johnson. "Proceedings of the International Conference on High Spin Physics and Gamma Soft Nuclei". In: (1991).

[20]   G.A. Leander, S. Frauendorf, and F.R. May. "Proceedings of the Conference on High Angular Momentum Properties of Nuclei, Vol. 4, Nuclear Science Research Conference Series". In: (1983).

[21]   E.S. Paul et al. "High-spin yrast states in the γ-soft nuclei ^{135}Pr and ^{134}Ce". In: *Physical Review C* 84.4 (2011), p. 047302.

[22]   R. Wyss et al. "Highly deformed intruder bands in the A $\approx$ 130 mass region". In: *Physics Letters B* 215.2 (1988), pp. 211–217.

[23]   J.N. Wilson et al. "Properties of superdeformed band population in the A $\approx$ 130 region". In: *Physical Review C* 57.5 (1998), R2090.

[24]   C.M. Petrache et al. "Lifetime measurements of highly deformed bands in ^{134,135}Nd and ^{131}Ce". In: *Physical Review C* 57.1 (1998), R10.

[25] S.M. Mullins et al. "First observation of the $i_{13/2}$ neutron orbital in the A = 130 region: spectroscopy of ^{135}Sm". In: *Journal of Physics G: Nuclear Physics* 13.9 (1987), p. L201.

[26] A. Galindo-Uribarri et al. "Strongly coupled enhanced-deformation band in ^{131}Pr". In: *Physical Review C* 50.6 (1994), R2655.

[27] J.N. Wilson et al. "Excited Superdeformed Bands in ^{133}Pr: Identification of the $g_{9/2}$ Proton Orbital". In: *Physical review letters* 74.11 (1995), p. 1950.

[28] V.F. Weisskopf. "Radiative transition probabilities in nuclei". In: *Physical Review* 83.5 (1951), p. 1073.

[29] G. F Knoll. *Radiation detection and measurement.* John Wiley & Sons, 2010.

[30] C.W. Beausang and J. Simpson. "Large arrays of escape suppressed spectrometers for nuclear structure experiments". In: *Journal of Physics G: Nuclear and Particle Physics* 22.5 (1996), p. 527.

[31] P.J. Nolan, F.A. Beck, and D.B. Fossan. "Large arrays of escape-suppressed gamma-ray detectors". In: *Annual review of nuclear and particle science* 44.1 (1994), pp. 561–607.

[32] J. Pakarinen et al. "The JUROGAM 3 spectrometer". In: *The European Physical Journal A* 56 (2020), pp. 1–8.

[33] G. Duchêne et al. "The Clover: a new generation of composite Ge detectors". In: *Nuclear Instruments and Methods in Physics Research Section A: Accelerators, Spectrometers, Detectors and Associated Equipment* 432.1 (1999), pp. 90–110.

[34] P.J. Nolan. *EUROGAM: A high efficiency escape suppressed spectrometer array.* Tech. rep. 1992.

[35] J. Sarén et al. "The new vacuum-mode recoil separator MARA at JYFL". In: *Nuclear Instruments and Methods in Physics Research Section B: Beam Interactions with Materials and Atoms* 266.19-20 (2008), pp. 4196–4200.

[36] M. Leino et al. "Gas-filled recoil separator for studies of heavy elements". In: *Nuclear Instruments and Methods in Physics Research Section B: Beam Interactions with Materials and Atoms* 99.1-4 (1995), pp. 653–656.

[37] J. Sarén. "The ion-optical design of the MARA recoil separator and absolute transmission measurements of the RITU gas-filled recoil separator". In: *Research report/Department of Physics, University of Jyväskylä* (2011).

[38] P. Papadakis et al. "Development of a low-energy radioactive ion beam facility for the MARA separator". In: *Hyperfine Interactions* 237 (Oct. 2016). DOI: 10.1007/s10751-016-1364-8.

[39] J. Uusitalo et al. "Mass analyzing recoil apparatus, MARA". In: *Acta Physica Polonica B* 50.3 (2019).

[40] R.D. Page et al. "The GREAT spectrometer". In: *Nuclear Instruments and Methods in Physics Research Section B: Beam Interactions with Materials and Atoms* 204 (2003), pp. 634–637.

[41] I. Lazarus et al. "The GREAT triggerless total data readout method". In: *IEEE Transactions on Nuclear Science* 48.3 (2001), pp. 567–569.

[42] P. Rahkila. "Grain—a java data analysis system for total data readout". In: *Nuclear Instruments and Methods in Physics Research Section A: Accelerators, Spectrometers, Detectors and Associated Equipment* 595.3 (2008), pp. 637–642.

[43] I.A. Alnour et al. "New approach for calibration the efficiency of HpGe detectors". In: *AIP conference proceedings*. Vol. 1584. 1. American Institute of Physics. 2014, pp. 38–44.

[44] D.C. Radford, M. Cromaz, and C.J. Beyer. "Analysis of high-fold gamma data". In: *AIP Conference Proceedings*. Vol. 481. 1. American Institute of Physics. 1999, pp. 570–580.

[45] D.C. Radford. "ESCL8R and LEVIT8R: Software for interactive graphical analysis of HPGe coincidence data sets". In: *Nuclear Instruments and Methods in Physics Research Section A: Accelerators, Spectrometers, Detectors and Associated Equipment* 361.1-2 (1995), pp. 297–305.

[46] K.S. Krane, R.M. Steffen, and R.M. Wheeler. "Directional correlations of gamma radiations emitted from nuclear states oriented by nuclear reactions or cryogenic methods". In: *Atomic Data and Nuclear Data Tables* 11.5 (1973), pp. 351–406.

[47]   E.S. Paul et al. "Detailed spectroscopy of the normally deformed states in 132Ce". In: *Nuclear Physics A* 619.1-2 (1997), pp. 177–201.

[48]   P.K. Weng et al. "High spin structure in odd-proton nuclei ^{129,131}Pr". In: *Physical Review C* 47.4 (1993), p. 1428.

[49]   B.H. Smith et al. "Enhanced deformation in light Pr nuclei". In: *Physics Letters B* 443.1-4 (1998), pp. 89–96.

[50]   D.G. Sarantites et al. ""The microball" Design, instrumentation and response characteristics of a 4π-multidetector exit channel-selection device for spectroscopic and reaction mechanism studies with Gammasphere". In: *Nuclear Instruments and Methods in Physics Research Section A: Accelerators, Spectrometers, Detectors and Associated Equipment* 381.2-3 (1996), pp. 418–432.

[51]   J. Gizon A.and Genevey et al. "Decay of ^{129}Nd to low-lying states in ^{129}Pr". In: *Zeitschrift für Physik A Hadrons and Nuclei* 358 (1997), pp. 369–371.

[52]   C.M. Parry et al. "Yrast structures in the neutron-deficient ^{127}Pr and ^{131}Pm nuclei". In: *Physical Review C* 57.5 (1998), p. 2215.

[53]   M.J. Godfrey et al. "Energy levels in ^{131}Pr". In: *Journal of Physics G: Nuclear Physics* 13.9 (1987), p. 1165.

[54]   E.S. Paul et al. "Measurement of transition quadrupole moments of high-spin states in the N= 74 isotones ^{133}Pr, ^{132}Ce and ^{131}La". In: *Nuclear Physics A* 690.4 (2001), pp. 341–354.

[55]   C.M. Petrache et al. "Spectroscopy of the deformed ^{126}Ce nucleus". In: *The European Physical Journal A-Hadrons and Nuclei* 16 (2003), pp. 337–346.

[56]   E.S. Paul et al. "High-spin study of ^{128}Ce and systematics of quasiparticle pair alignment". In: *Nuclear Physics A* 676.1-4 (2000), pp. 32–48.

[57]   D.M. Todd et al. "Rotational band structures and lifetime measurements in ^{130}Ce". In: *Journal of Physics G: Nuclear Physics* 10.10 (1984), p. 1407.

[58]   R. Wadsworth et al. "Yrast band spectroscopy of ^{132}Sm and ^{130}Nd". In: *Zeitschrift für Physik A Atomic Nuclei* 333.4 (1989), pp. 411–412.

[59] A.N. James et al. "Microsecond mass separation of heavy compound nucleus residues using the Daresbury recoil separator". In: *Nuclear Instruments and Methods in Physics Research Section A: Accelerators, Spectrometers, Detectors and Associated Equipment* 267.1 (1988), pp. 144–152.

[60] A.A. Sonzogni. "Nuclear Data Sheets for A = 134". In: *Nuclear Data Sheets* 103.1 (2004), pp. 1–182.

[61] E.S. Paul et al. "Prolate and oblate rotational bands in ^{136}Sm". In: *Journal of Physics G: Nuclear and Particle Physics* 19.6 (1993), p. 861.

[62] E.S. Paul et al. "Shape coexistence in ^{138}Sm and evidence for the rotational alignment of a pair of N= 6 neutrons". In: *Journal of Physics G: Nuclear and Particle Physics* 20.9 (1994), p. 1405.

[63] I. Schneider et al. "Magnetic dipole band in ^{124}Xe". In: *Physical Review C* 60.1 (1999), p. 014312.

[64] D. Ward et al. "Gamma-ray spectroscopy of ^{126}Ba". In: *Nuclear Physics A* 529.2 (1991), pp. 315–362.

[65] D.J. Hartley et al. "Yrast spectroscopy of ^{130}Nd and evidence of a highly deformed band". In: *Physical Review C* 63.2 (2001), p. 024316.

[66] L. Grodzins. "THE UNIFORM BEHAVIOUR OF ELECTRIC QUADRUPOLE TRANSITION PROBABILITIES FROM FIRST 2sup+ STATES IN EVEN-EVEN NUCLEI". In: *Phys. Letters* 2 (1962).

[67] C.M. Parry et al. "Evidence for highly deformed bands in ^{133}Sm". In: *Physical Review C* 60.5 (1999), p. 054314.